UNIVERSITY OF BIRMINGHAM

BIOGENIC PRECIOUS METAL-BASED MAGNETIC NANOCATALYST FOR ENHANCED OXYGEN REDUCTION

by

ANNA ROSE WILLIAMS

A thesis submitted to
The University of Birmingham
for the degree of

DOCTOR OF PHILOSOPHY

Centre for Hydrogen and Fuel Cell Research
School of Chemical Engineering
College of Engineering and Physical Sciences
University of Birmingham

September 2015

ABSTRACT

This work contributes to the development of electrocatalysts for use in polymer electrolyte fuel cells, specifically for the cathodic oxygen reduction reaction (ORR). To achieve this, electrochemical analysis was conducted using biofabricated platinum (bio-Pt) catalyst. Bio-Pt per se was found to be a poor catalyst for the ORR, attributed to the platinum being inaccessible to the reactants. Various 'cleaning' techniques were tested to partially remove biomass, providing improved catalytic activity.

Bio-Pt was found to possess ferromagnetism under bulk magnetic analysis. Local magnetic analysis of this phenomenon focussed predominantly upon biofabricated palladium (bio-Pd) rather than bio-Pt as the origin of the magnetism appears to be the same in both cases and the effect was stronger in bio-Pd samples. This showed that bio-Pd possessed multiple magnetic types, which were suggested to arise from different types of Pd structure by comparison with electron microscopy studies.

Oxygen is paramagnetic, thus it can be expected to experience a force towards an increasingly strong non-uniform magnetic field. Bio-Pt was exposed to a magnetic field prior to electrochemical testing to magnetise the nanoparticles. Magnetised bio-Pt produced superior diffusion limited current, suggesting that magnetic bio-Pt catalyst enables the enrichment of oxygen from air at the catalyst site.

ACKNOWLEDGEMENTS

I would like to thank the DTC staff for having faith in my ability to complete what I feel to have been a complicated study. In particular my thanks go to my lead supervisor Professor Lynne Macaskie who was a constant, invaluable, source of assistance available to me throughout, to Dr. Neil Rees who arrived in time to ensure the electrochemistry was done properly and for his humour that helped keep me sane when things were not working as they should, to Dr. Waldek Bujalski who, for a brief period, was one of my supervisors and during which time he introduced me to the wonders of EndNote and to Mr. John Hooper who helped me with many of the tasks that are required for an endeavour such as this, and for doing so both expertly and cheerfully.

Throughout my studies I have needed to learn many new things. For their assistance in this I would like to thank the members of the Unit of Functional Bionanomaterials and the members of the Centre for Hydrogen and Fuel Cell Research for helping me to learn many important, and some not so important, things throughout my study. I would also like to thank Drs. Stephen Cottrell, Rustem Khassanov and Pavlo Mikheenko for their invaluable assistance on the magnetic aspects of this study.

I also thank the EPSRC for funding this work.

Finally I would like to thank my family and friends for putting up with me so long. Particularly to Ian and Katie, university was not the same after you finished; and to Dean for ensuring I remained adequately nourished throughout the lengthy writing up period.

TABLE OF CONTENTS

Contents

List of Figures

List of Tables

Abbreviations

Abbreviation	Meaning
Bio-Pd	Biofabricated palladium nanoparticles
Bio-Pt	Biofabricated platinum nanoparticles
CV	Cyclic voltammetry/voltammogram
Dd-Pt	Biofabricated platinum nanoparticles on *Desulfovibrio desulfuricans* biomass
Ec-Pt	Biofabricated platinum nanoparticles on *Escherichia coli* biomass
ECSA	Electrochemical surface area
EDX	Energy-dispersive X-ray
FCC	Face centered cubic
FTIR	Fourier transform infra-red spectroscopy
FWHM	Full width at half maximum
GC	Glassy carbon
GPS	General purpose surface-muon instrument
HAADF	High-angle annular dark-field
HOMO	Highest energy occupied molecular orbital
ICP-MS	Inductively coupled plasma mass spectrometry
MOPS	4-morpholinepropanesulfonic acid
MPMS	Magnetic property measurement system
OFN	Oxygen-free nitrogen
ORR	Oxygen reduction reaction
PEFC	Polymer electrolyte fuel cell

RDE	Rotating disc electrode
SEM	Scanning electron microscopy
SQUID	Superconducting quantum interference device
SRB	Sulphate reducing bacteria
STEM	Scanning transmission electron microscopy
TEM	Transmission electron microscopy
TKK	Tanaka Kikinzoku Kogyo
UV-VIS	Ultraviolet-visible spectroscopy
XPS	X-ray photoelectron spectroscopy
XRD	X-ray diffraction
μSR	Muon spin rotation spectroscopy

1. BIOREDUCTION OF PRECIOUS METALS

Bioreduction is a nanoparticle preparation option that is of particular interest due to the low temperatures and freedom from the environmentally harmful chemicals that are typically used in chemical methods of nanoparticle synthesis. This study focusses upon the use of precious metals, particularly palladium and platinum, due to their catalytic effectiveness. There are a range of different organisms that can be used to achieve this goal, including bacteria, plants and fungi, even extending to various chemicals extracted from these, such as proteins. However, these are not the only variables that play an important role in bioreduction, e.g. pH can affect the conformation of biochemicals and complexation of the metal precursor. Such an alteration can lead to changes in rate of uptake and structural differences in the resulting nanoparticles.

1.1 Nanoparticle Production

Nanoparticles, which are a key catalytic component of polymer electrolyte fuel cells (PEFCs), can be created through a variety of methods. The chemical methods of ultraviolet irradiation, aerosol technologies, lithography, laser ablation, ultrasonic fields and photochemical reduction are typically expensive and involve the use of hazardous chemicals[1]. Bioreduction provides an alternative to these methodologies, with the benefit that it does not require expensive or hazardous chemicals in the preparation of the nanoparticles, with the exception of the metal precursor[2].

1.1.1 Biosorption

When living or dead biomass removes metal ions from solution, the process is known as biosorption. The term biosorption covers a range of physical and chemical mechanisms, such as adsorption or ion exchange; which can be further broken down into complexation, coordination or chelation taking place between the metal ion and ligands (Figure 1.1 is a representation of the various mechanisms which occur)[3]. In the case of living biomass, metabolic processes such as transport, internal compartmentalisation, metal precipitation as sulphides or oxalates and sequestration by metal binding proteins, peptides or siderophores can impact upon the biosorption result[3-5].

1.1.2 Bioreduction

Biosorption does not suffer ill effects when using autoclaved microorganisms, showing that there is no enzymatic contribution; whereas bioreduction is affected by autoclaving, suggesting that an active enzyme process contributes to the reduction[5-7]. It is believed that hydrogenase enzymes[8,9] and nicotinamide adenine dinucleotide phosphate (NADP) dependant nitrate reductase enzyme[10-14] are amongst the most important enzymes for bioreduction. The role of the enzymes are to serve as nucleation sites and to carry out the oxidation of the electron donor, and subsequently provide the resulting electrons to the metal ions[6,15,16]. The biomass itself is thought to do very little other than channelling the electrons, which are produced by the hydrogenase activity, and acting as an immobilization matrix similar in nature to the conventional carbon supports used in chemical synthesis[8].

Sodium dodecyl sulphate polyacrylamide gel electrophoresis (SDS-PAGE) analysis of gold nanoparticles produced by a cell free extract of *Rhodopseudomonas capsulata* revealed that one or more proteins in the size range 14-98 kDa were associated with the nanoparticles[1]. It was not determined if these were hydrogenase subunits or other proteins.

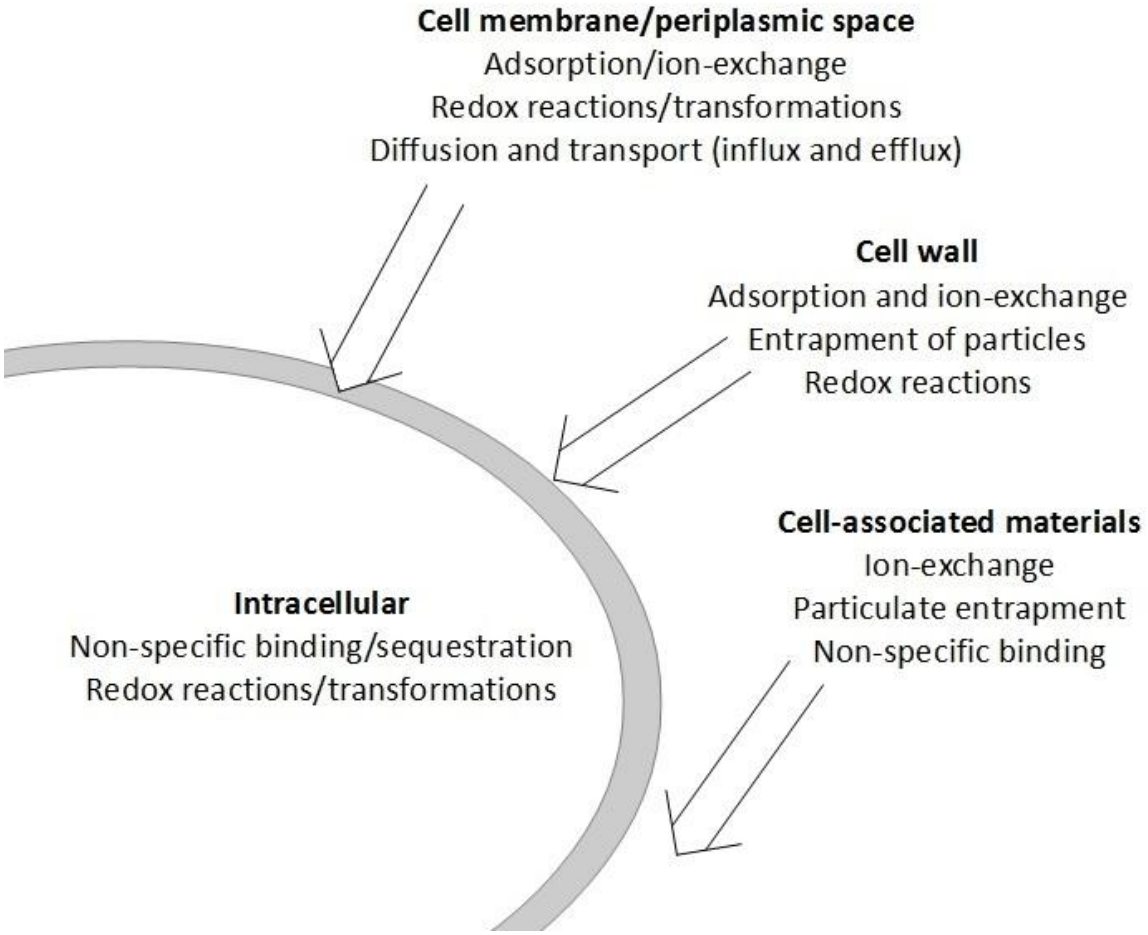

Figure 1.1, processes contributing to the microbial uptake of metals. Not all locations for processes have been confirmed. Image adapted from Gadd and White (1993)[3].

Active enzyme processes are most effective under certain temperature and pH conditions; however it has been found that the optimum temperature and pH which is most effective

for the bioreduction of metal ions is not the same as that for normal activity of the enzymes[14,17-19]. As the reduction of metal ions is not a normal function of hydrogenases the optimum conditions for these need not be the same[20]. The nanoparticles produced during various studies possessed a range of shapes and sizes, thus the local environment housing the enzyme may help steer nanoparticle morphology[21].

1.1.3 Palladium

The mechanism of Pd(II) bioaccumulation is not fully understood, however it is believed to consist of three parts[8,9]. The first part consists of the sorption of aqueous $PdCl_4^{2-}$ onto protonated groups. This is followed by either the oxidation of an externally supplied reducing agent by periplasmic hydrogenases, allowing electrons to be supplied to the Pd(II) ions or the channelling of endogenous electrons to the Pd(II) ions. Either of which lead to the reduction of Pd(II) to Pd(0). Finally the Pd(0) seeds can store and channel hydrogen as $H^{\bullet}$, which allows for the autocatalytic reduction of further Pd onto the seeds. Fourier Transform Infra-Red (FTIR) spectroscopy has been used to ascertain that the locations where Pd(II) sorption takes place are likely to be the hydrogen ions of –OH, -COOH and $–NH_2$ groups on the biomass[22].

A range of *Desulfovibrio fructosivorans*[16] and *Escherichia coli*[23] mutants that were defective in various hydrogenases were tested against wild type cells and autoclaved cells for Pd reduction. This showed that when only one hydrogenase was present Pd biosorption would occur at its location, with no significant alteration to the rate of the subsequent reduction.

The lack of Pd reduction by autoclaved cells shows that some active mechanism is required to trigger the nucleation and/or initiation of Pd crystal growth, although the subsequent crystal growth is due to autocatalytic reduction[24].

1.1.4 Platinum

The bioreduction of platinum is believed to consist of the uptake of aqueous Pt(IV) or Pt(II) complex onto the biomass, followed by a reduction stage[15]. Platinum is most readily found as a Pt(IV) ion in a chloride complex (although Pt(II) species are available), whereas palladium is typically a Pd(II) chloride. This leads to a more complex reduction process that has been shown to involve Pt(II) as an intermediate step[25]. Energy Dispersive X-Ray (EDX) analysis of solids of various samples taken from a bioreduction of Pt(IV) using sulphate-reducing bacteria (SRB) cells showed that Pt(II) was present during the reduction process. Samples taken within the first 2 hours showed that the Pt(IV) concentration in the solution dropped rapidly, with the Pt(II) concentration rising at almost the same rate. After the first 2 hours the Pt(IV) concentration had settled at equilibrium, whereas the Pt(II) concentration took a significantly longer time to do the same. It was also found that under aerobic conditions the rate of Pt(IV) reduction was significantly lower than under anaerobic conditions, whereas the Pt(II) rate of reduction was not found to be noticeably affected by the presence of oxygen, therefore suggesting that the two processes undergo different reduction mechanisms[6].

To investigate the effect of hydrogenase activity on bioreduction of Pt(II) and Pt(IV) ions Cu(II) ions can be used as they are known to inhibit the activity of periplasmic hydrogenases in SRB[26,27]. When SRB biomass was pre-treated with Cu(II) prior to use in the bioreduction of Pt(II) and Pt(IV) ions it was found that only the reduction of Pt(II) ions were inhibited (determined by UV spectroscopy of the concentration of Pt(IV) remaining in solution)[6]. This shows that bioreduction of Pt(II) involves an active periplasmic hydrogenase process whereas the bioreduction of Pt(IV) does not. As heat killed cells have reduced reductive capabilities towards both Pt(II) and Pt(IV), either an active hydrogenase process is involved in both or there have been sufficiently great conformational changes to the enzymes in heat killing that passive processes are affected[6,14]. The presence of an active enzyme process was supported by cooling viable SRB cells to 4 °C for 15 minutes to lower their metabolic rate prior to Pt(IV) exposure, resulting in a considerably slower reduction process[6].

As pretreating with Cu(II) ions specifically inhibits periplasmic hydrogenases whereas heat killing of cells would affect other enzymes also, it is possible that other enzymes are playing an active role in the bioreduction of Pt(IV). Cytoplasmic hydrogenases are known to be unaffected by Cu(II) ions, thus these have been proposed to be playing a role in the bioreduction process[6,26].

Combining all these findings, it seems likely that the Pt(IV) bioreduction process follows a similar route to that proposed for Pd(II)[16], with the initial nucleation and initiation step being an active enzyme process, and with further reduction occurring autocatalytically. The important difference between Pt(IV) and Pd(II) being the inclusion of an intermediate Pt(II) step, potentially involving an additional enzyme (Figure 1.2). It is possible that the Pt(IV) ions

would be able to bypass the permeability barrier of the cells due to their toxicity, which has been found to make the membranes permeable, thus increasing the number of potential enzymes which could take part in the reduction process[7].

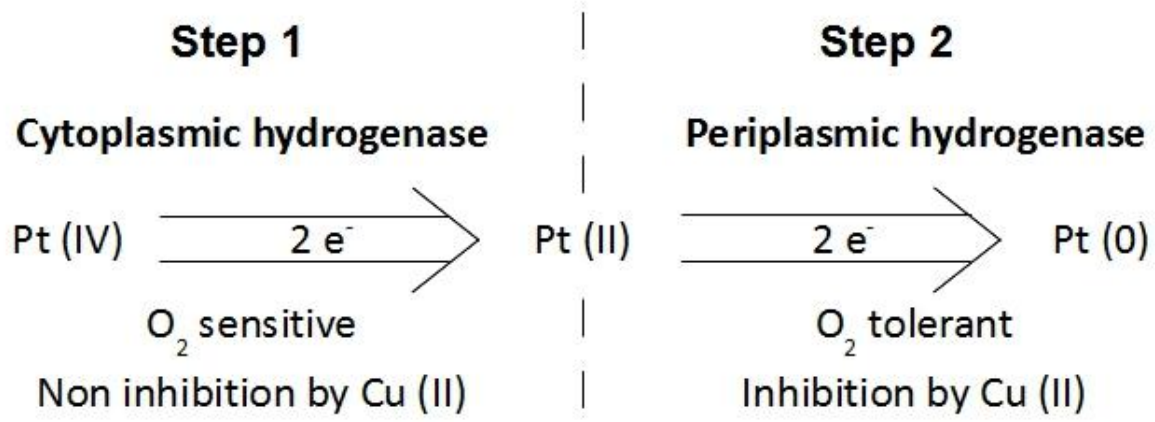

Figure 1.2, a proposed mechanism for the two stage bioreduction of Pt(IV) into Pt(0) nanoparticles. Image adapted from Riddin et al. (2009)[6].

1.2 Biological Variables for Bioreduction

The structure and size of the nanoparticles can be affected by the choice of the type of biomass which is used for the bioreduction as this provides biosorption sites that may impose structural limitations upon the resulting biofabricated nanoparticles.

1.2.1 Bacteria

There is typically a variety of levels of metal loading on the cells within a population of bacteria, ranging from some not supporting any metal to bearing large metal clusters, which probably occurs due to metabolic differences between the cells[8,28]. X-ray absorption near edge spectroscopy was employed to determine that platinum had been reduced from $PtCl_6^{2-}$ to discrete Pt(0) nanoparticles of ~5 nm diameter by *Shewanella algae* using lactate as electron donor, showing that low diameter nanoparticles can be produced with a bacteria-assisted reduction technique[15]. Furthermore, EDX analysis has confirmed that nanoparticles produced in this manner do not contain any of the chlorine complex which was initially associated with the platinum ions (0.4 wt. % detection limit)[15].

When bacteria are used for bioreduction, the metallic nanoparticles which are produced have been found to occupy the periplasmic space between the inner and outer membranes[7,15,16,29], although more recently it has been shown that even smaller nanoparticles can occur throughout the entirety of the cell[30].

The choice of bacteria or even mutants within the same species will affect the resulting nanoparticle uptake, size and catalytic ability[23,31-33]. When comparing three different species of *Desulfovibrio* (*D.desulfuricans*, *D.vulgaris* and *D.fructosivorans*) it was found that *D.desulfuricans* produced the best biosorptive Pd and Pt uptake over a range of conditions, with *D.fructosivorans* consistently performing poorest[5]. This work was corroborated by findings of the Pd uptake of *Cupriavidus necator*, *Pseudomonas putida*, and *Paracoccus denitrificans*, with *C.necator* outperforming the others[29]. Not only has the uptake of precious

metals varied between species, but also the size of produced nanoparticles. Using *Desulfovibrio desulfuricans*, *Cupriavidus metallidurans* and *Escherichia coli* it was found that the nanoparticle size produced was greatest with *E.coli* and smallest with *D.desulfuricans*[32].

It is possible that the size of the produced nanoparticles remains the same between mutants of the same species, although catalytic ability of such nanoparticles have been shown to differ[32]. When bio-Pd produced using wild type *E.coli* and hydrogenase-negative mutants were tested for chemical catalytic ability it appears that the presence of Hyd-1 (one of the two periplasmic facing hydrogenases in wild type *E.coli*) in the bioreduction process was necessary to produce the most effective catalyst[23]. The electrocatalytic activity of nanoparticles produced by an *E.coli* mutant possessing only Hyd-1 was found to be substantially greater than that of the wild type[32,34]. When comparing a range of hydrogenase deficient mutants of *D.fructosivorans*, it was discovered that the nanoparticle cluster growth is more rapid at hydrogenase nucleation sites on the cytoplasmic membrane[16]. This effect could contribute to the differences in catalytic ability between mutants because some results suggest that the rate of cluster growth can affect the nanoparticle morphology[13,35], and the morphology of nanoparticles is known to have an impact upon their catalytic ability[36]. The hydrogenases which are available seemingly affect both the localisation and catalytic ability of the produced nanoparticles. It is believed that there is a direct link between the localisation of nanoparticles and both their chemical and electrochemical catalytic ability, which may be due to the structural conformation enforced by the surrounding biomass[34]. Yet there is no obvious physical difference between the

nanoparticles produced by mutants; however, minute differences may be present as high resolution transmission electron microscopy (TEM) comparison was not employed[32].

1.2.2 Biofilms

Some microorganisms form biofilms, which have been viewed as a potential form of immobilisation of the biomass[4]. It was determined that, in the case of an *E.coli* culture, precious metal deposition did not occur throughout the biofilm, but was limited to several localized areas, although a more even distribution could be obtained if the biosorption were to occur prior to the formation of the biofilm. When prepared in this manner platinum or palladium loaded biofilms could be produced, which incorporated a flow channel structure consistent with that of biofilms of *E.coli* which were formed of non-metallised biomass. The metallised biofilms, when prepared with Nafion® for PEFC testing, were found to be non-conductive and thus unsuitable for that application[37].

1.2.3 Plants and Plant Extracts

When plants are grown in the presence of metal ions it has been found that the metal ions will be taken up into the plant. Bioaccumulation occurs in both the roots and shoots; however the amount in shoots is a small percentage of the amount found in roots[38]. Through the use of TEM, the nanoparticle formation has been determined to occur predominantly on the cell walls and organelles[39].

Crystalline Pt nanoparticles of differing morphologies, albeit mostly spherical, were found to form in epidermal *Medicago Sativa* and *Brassica Juncea* root cells after 24 hours of exposure to a 40 ppm $Pt(NH_3)_4(NO_3)_2$ solution[40]. The diameter of the nanoparticles formed was ~20 nm; thus, as it is known that root cell membranes allow a maximum of 10 nm particles to pass through them[41], the presence of these larger particles in the root epidermal cells would suggest that the reduction of Pt(II) to Pt(0) had taken place in vivo[40].

It is also possible to form nanoparticles with plant extracts rather than using the plant as a whole. The protein content of the plant extract is able to act as stabilizing and/or capping agents which are able to protect the nanoparticles from agglomerating in solution; as determined by analysis of FTIR spectra[17,42-44]. Proteins are not always involved in the bioreduction process; FTIR data has been employed to determine that it is possible for terpenoids and similar metabolites to fulfil this role also[19]. Produced nanoparticles have been found to be stable in solution for several months[17,45].

The use of plant extracts for the bioreduction of Pt(IV) has been found to require incubation at 95 °C for 150 min to achieve 90% Pt reduction[19]. Whilst the high temperature is undesirable, there are potential benefits to the use of plant extract as differently shaped or sized nanoparticles have been found to form under some conditions. Very small (2.4±0.7 nm) and stable (over 6 months) platinum nanoparticles have been observed when an aqueous solution of gum kondagogu (*Cochlospermum gossypium*) was exposed to H_2PtCl_6[17]. *Diopyros kaki* leaf extract has been found to produce Pt nanoparticles in the range 2-12 nm if the reaction temperature or leaf extract concentration are varied, allowing for the size control of small nanoparticles[19].

1.2.4 Fungi

The bioreduction capability of *Fusarium oxysporum* was investigated over a range of temperature, pH and Pt(IV) concentrations. It was found that the optimum conditions for platinum uptake were conditions that would be detrimental to enzyme activity, pH 9, 65 °C and 15.13 mM H_2PtCl_6[14,46]. Over the course of the experiments many different nanoparticle morphologies (circles, pentagons, hexagons, squares and rectangles) were observed through TEM, although the majority were square or rectangular and sized between 10-100 nm. These were found to have formed through both inter- and extra-cellular processes, however intracellular production was much less common[14].

1.2.5 Biochemicals

A range of different biochemicals have been found to be capable of application in the bioreduction of precious metals.

1.2.5.1 Proteins

Apoferritin is a protein consisting of 24 subunits, which assemble to form a hollow cagelike structure[47]. This has been employed for the uptake of several different metal cations from solution, including Pd(II)[48] and Pt(II)[49]. When metal cations are introduced to apoferritin there is a gradual decrease in the metal ion concentration of the solution without the formation of nanoparticles. The metal cations are able to enter the 8 nm internal cavity[47]

through the 0.3-0.4 nm diameter channels[50]. They enter through the channels probably due to the cavity of the protein being negatively charged at pH 9.0[51] and are then trapped within due to electrostatic interactions. If a 5-fold excess of $NaBH_4$ is provided as a reducing agent it is possible to produce spherical nanoparticles[48,49]. Using this method Pt nanoparticles of 4.7±0.9 nm[49] and Pd nanoparticles of 2.0±0.3 nm[48] have been synthesized; however there remains an intact apoferritin shell surrounding the nanoparticle which would probably need to be removed prior to catalysis applications.

1.2.5.2 Oligonucleotides

It is possible to employ long RNA or DNA sequences for the manufacture of precious metal nanoparticles. Portions of sequences are required to be able to form nanoparticles and the rest of the sequence governs the size and shape of the resulting nanoparticle[52]. The oligonucleotide sequence can be attached to a surface such that it is possible to carry out the metallic nanoparticle production *in situ*[53].

1.2.5.3 Honey

Honey has been found as an option as a substrate for bioreduction of Pt(IV) as it contains many sugars which allows for bioreduction without an externally supplied electron donor. It is necessary to heat a mixture of honey dissolved in water and H_2PtCl_6 to 100 °C for a period of 2-4 hours to produce nanoparticles of 1.1-3.4 nm[18].

1.3 Chemical Variables for Bioreduction

Changes to the biosupported nanoparticles can be produced without changing the supporting material as described above. There are a range of conditions which affect the reduction and lead to differences in the nanoparticles.

1.3.1 The Effect of pH

The pH of the combined biomass and precious metal solution has been found to have a profound effect upon the result of the bioreduction process. By considering the effect of the pH on the biosorbent groups it is possible to understand why this is the case. At low pH the basic functional groups which have been found to play important roles in the bioreduction process, such as amines, become protonated. Once these groups are protonated it becomes easier for the negatively charged metal complexes to approach the biomass; however, the removal of the complexing agent from the metal becomes less energetically favourable due to electrostatic interactions, and thus proceeds more slowly. The slower reduction step allows for the production of nanoplates, which are thermodynamically less favourable than spherical nanoparticles[13,40,54]. At less acidic pH the functional groups are not as greatly protonated, and thus less attractive to the metal complexes; however, the reduction is more favourable thus proceeds more rapidly, resulting in the formation of thermodynamically more favourable spherical nanoparticles[13]. In addition to this, there is also an impact upon the metal complex itself. If the pH is sufficiently low, the metal is more likely to be found in a non ionic or cationic form and thus less favourable to electrostatic

interaction with the protonated biomass[22,55]. Thus finding the optimum pH for any particular result involves the balancing of various competing processes.

The proclivity for maximal uptake at low pH has been shown to occur in greatly different types of biomass. The uptake of Pt with the plant *Brassica juncea* at pH 3 has been found to be 26 times greater than that at pH 9 when a 40 ppm metal solution was used[40]. In a similar test which was carried out using the yeast *Saccharomyces cerevisiae* and the algae *Chlorella vulgaris*, it was found that in both cases the uptake was greatest at around pH 2 for Pt and Pd[56]. However, the effect of pH on metal uptake not only varies with biomass, but also with the metal complex used. When the uptake of Pd from $Pd(NH_3)_4Cl_2$ was compared to that of Na_2PdCl_4 using *D.desulfuricans*, it was found that Pd from Na_2PdCl_4 was more readily biosorbed, however the uptake from $Pd(NH_3)_4Cl_2$ was found to be less pH dependent[24].

The pH is also capable of affecting the size and/or shape of produced nanoparticles; with *Cinnamom zeylanicum* bark extract used for the bioreduction of $PdCl_2$ it was found that an increase in pH led to slightly larger nanoparticles[45]. When *Rhodopseudomonas capsulata* was used for the biosorption of gold from $HAuCl_4$ solution over the course of 48 hours the opposite was observed; it was found that at pH 7 spherical nanoparticles, sized 10-20 nm, were formed and at pH 4 the nanoparticles consisted primarily of triangular nanoplates, sized 50-400 nm[13]. Sugar beet pulp and $HAuCl_4$ solution produced similar results with triangular nanoplates forming at low pH and nanowires forming at high pH[42]. The length of these nanowires increased as the pH was increased further[43]. As the beet pulp is a strong complexing agent of gold ions this effect arises due to the hydroxyl ions inhibiting the capping ability[42,57], thus highlighting an instance of pH affecting the biomaterial leading to a

different conformation of metal nanostructure. As it is known that the alteration of pH will changes shape of proteins[58-60], this can provide a range of different micro-environments for the metal nanoparticles to form and grow, and thus produce differently shaped nanoparticles[14].

1.3.2 The Effect of Competing Ions

Many chemicals can be used to control the pH of the metal ion solution; the choice of which one is used can also have an impact upon the metal uptake. With three different species of *Desulfovibrio* it was determined that if HCl were used to modify pH it inhibited the uptake of Pd when compared to the results of solutions where the pH was modified with HNO_3 or H_2SO_4 [5]. The affect upon palladium uptake could be explained by the speciation of palladium at low pH in the presence of high chloride concentration, which can lead to anionic species[55]. The same investigation was also carried out with Pt which found that HCl had, over most pH values, optimum uptake[5]. When a chitosan biosorbent was used for Pt uptake, chloride was also found to be the preferred competitor ion[61].

Sorption isotherms for Pd by *D.desulfuricans, D.fructosivorans* and *D.vulgaris* were fitted to the Langmuir and Freundlich models[5]. It was found that for HCl the Freundlich model was a better fit to the data, whereas for HNO_3 and H_2SO_4 the Langmuir model was a better fit. The findings for Pt sorption showed that the Langmuir model was a better fit for HCl and HNO_3 but the Freundlich model was a better fit for H_2SO_4. This suggests that the presence of certain ions could alter the sorption mechanisms of Pd and Pt[5].

When the chloride ion concentration was enhanced by the addition of NaCl, a competition effect occurring with the metal ions was observed; to which platinum uptake was found to be more sensitive than that of palladium[5]. Typically Pt and Pd sources are chloride complexes, thus this competition effect may need to be alleviated. This can be achieved by the introduction of a Na_2CO_3 buffer to the system which prevents the build up of a high concentration of chloride ions[21].

1.3.3 The Effect of Metal Ions

The metal ion concentration has been found to affect both the uptake of metal and the morphology of produced nanoparticles. When $PdCl_2$ was bioreduced by *Shewanella oneidensis* it was found that by increasing the Pd(II) concentration it resulted in larger primary particles of Pd on the microorganism, with the particle size increasing from 4 to 7 nm diameter as the Pd(II) concentration was increased from 2.5 to 20 mol/m^3. Agglomeration was found to be a greater problem when the Pd(II) concentration was lower and as a result the nanoparticle surface area was found to be greatest at 10 mol/m^3 [35]. The bacterial coverage was far more varied at lower Pd(II) concentrations, indicating that the nucleation had not been complete, whereas the higher Pd(II) concentration allowed for more rapid, and more even nucleation throughout the bacterial population. The more even nucleation resulted in greater distances between particles reducing the likelihood of agglomeration[35]. Similar results have been found using Pd(II) with *Staphylococcus sciuri* and *Cupriavidus necator*[62], and Pt(IV) and cell free extract from sulphate-reducing bacteria[63].

As the reduction capabilities of dead cells are inferior to those of live cells[5], and exposure to heavy metals is known to be toxic to cells[64], the effect of the metal ions upon the viability of cells must be considered. An example of the effect of this toxicity is that *Cupriavidus necator*, *Pseudomonas putida*, and *Paracoccus denitrificans* were found to be unculturable following a 14 hour exposure to 3.4 mM Pd(II)[29], thus even the very low concentrations typically used for bioreduction of precious metals can have an impact upon the viability of cells.

When cells of *Shewanella oneidensis* were exposed to a solution of 5 mg/L Pd(II) without the presence of an electron donor they were found to be mostly capable of surviving, although the culturable fraction was reduced by about 2 log units. When the Pd(II) concentration was increased to 25 mg/L without the presence of an electron donor the cells were unculturable after 10 minutes and, after a 300 minute exposure, about 80 % of the cells were killed. *S.oneidensis* with H_2 in the headspace was found to be capable of resisting the toxicity of 25mg/L Pd(II), with about 10 % of cells killed and less than 1 log unit reduction of the culturable fraction. When 25 mM formate was provided as an electron donor the cells were more capable of resisting the toxic effects of the Pd(II) than without an electron donor, but less capable than when provided with H_2. The culturable fraction had dropped by about 2 log units after 60 minutes, but recovered to the same level as the cells in the presence of H_2 after 300 minutes[65]. The difference is probably the result of the rate at which electrons can be liberated from the electron donor as hydrogen has more rapid kinetics than other electron donors[7]. The reduction of metals appears to be a biological defence mechanism to remove the toxicity from their environment.

This toxicity can also have further implications; Sulphate Reducing Bacteria (SRB) cell plasma membranes were found to become permeable to fluorescein after exposure to solutions of $PtCl_4$ in concentrations as low as 5 mg/L, indicating that there was damage caused by the exposure[7]. This permeability could be the cause of heavy metal compounds being capable of passing into the cytoplasm, as shown by Omajali *et al.* (2015)[30], even though there is no known biological function for this to occur.

1.3.4 The Effect of Electron Donor

The electron donor has been shown to have an impact upon the nanoparticles which are produced. When $PdCl_2$ was bioreduced by *S. oneidensis* using formate as electron donor it was found that increasing the formate concentration resulted in larger particles of Pd on the microorganism and that the increased particle size was the result of a more rapid reduction process[35]. The rate of reduction can also be altered by choice of electron donor as testing of hydrogen, lactate and ethanol with SRB showed that hydrogen produced the most rapid reduction and ethanol the slowest[7]. The first factor is that hydrogen is a small molecule, which means that it can more readily diffuse through the membrane to reach the hydrogenase enzymes which will oxidise it and liberate electrons. The second factor is that the electrons which are liberated from other electron donors such as lactate by lactate dehydrogenases feed through a different and likely more complex electron transport chain before they are capable of reaching the metal ions[7]. There are further implications that arise due to the different enzymes being used in the reduction as it was discovered that when

formate is used as the electron donor the oxygen sensitivity is far greater than when H_2 is used[9]. Reduction via formate has also been found to be far less tolerant to competing ions within the system, with particular sensitivity to Cl^- ions[9]. This has implications that the optimal choice of electron donor may be different depending upon a range of factors relating to the expected reduction conditions and the desired nanoparticle size.

1.4 Summary

There are many biomaterials which can be utilised for the bioreduction of metals, with each leading to differences in the final structure of the resulting nanoparticles. These nanoparticles can be further tailored towards a desired product by adapting the chemical conditions present for the biosorption, reduction or both processes. However, due to the great number of variables, there is the possibility that any change may result in multiple differences as each change can affect multiple aspects of the bioreduction process. An example of such is that pH can alter protein conformation and the chemical complexation of the metal precursor, both of which can affect the end product. As a result of such a great range of variables, and their interlinking, bioreduction is a very powerful technique that allows for tailoring towards a desired goal but achieving that goal can prove to be difficult.

2. INSTRUMENTS

This chapter describes the instruments used throughout this work, their operation modes which were used and the science which underpins the techniques.

2.1 Electron Microscopy

Electron microscopy is a technique that allows for the imaging of materials in sufficiently high resolution for identification of nanostructures, which is not possible with optical microscopy. The limit of resolution of a microscope is determined by the wavelength of the waves used, as described by the Rayleigh criterion (Equation 2.1)[66]. For green light, with a wavelength of about 550 nm, which sits in the middle of the visible spectrum the limit of resolution of an optical microscope is about 300 nm. Due to quantum mechanical wave-particle duality, as described by de Broglie, it is possible to utilise elementary particles to achieve microscopy at greater resolution than is possible with visible light[67]. The de Broglie equation (Equation 2.2) shows that the wavelength of the beam of particles is inversely proportional to its momentum. To achieve a shorter wavelength than visible light, a beam of electrons can be generated from a filament and accelerated by a voltage. The magnitude of this voltage determines the electron momentum as described in Equation 2.3[66]. In this equation the second term in the denominator is required due to due to the relativistic effects that result from particle velocities exceeding half the speed of light; at ≈100 keV accelerating voltage.

$$\delta = \frac{0.61\lambda}{\mu \, sin\beta} \tag{2.1}$$

where δ is the smallest distance that can be resolved, λ is the wavelength of the radiation, μ is the refractive index of the viewing medium and β is the semi angle of collection of the magnifying lens.

$$\lambda = \frac{h}{p} \tag{2.2}$$

where λ is the wavelength of the particle, h is Planck's constant and p is the momentum of the particle.

$$\lambda = \frac{h}{\left[2m_0 eV\left(1 + \frac{eV}{2m_0 c^2}\right)\right]^{1/2}} \tag{2.3}$$

where m_0 is the electron rest mass, e is the charge on an electron, V is the accelerating voltage and c is the speed of light in a vacuum.

In an electron microscope, once the electrons have been produced and accelerated, it is necessary to ensure that they are focussed upon the sample. This is achieved by using a series of apertures and electromagnetic lenses[68]. Once the electrons become incident upon the sample it is possible for them to be transmitted, if the sample is sufficiently thin[69]. Other effects occur such as backscattering of electrons, the generation of secondary electrons, which are electrons emitted from the sample, or X-rays arising due to the excitation caused by the electron beam[70]. For transmission electron microscopy (TEM), samples are thin to

allow for the transmission of electrons. As the electron passes through the material it may be affected by it which, ultimately, is what allows for the image to be generated[69].

When the electrons pass through the sample some are scattered whereas others are not[71]. The primary manner in which electrons interact with the sample is through electrostatic interaction with the atoms within it[72], although it is possible for scattering to occur due to Lorentz interaction with magnetic samples[73]. Any scattering events that cause scatter greater than the objective aperture semi-angle lead do not contribute to the image formed by the transmitted, or direct, beam[71]. Where an electron is scattered by an atom as a result of electrostatic interaction, the degree of scatter is determined by the force between the electron and either the nucleus or electron within the atom with which it is interacting. Coulomb's law (Equation 2.4) shows that this is determined by the charge on the atom and the proximity the electron passes to the scattering body[74]. For a nuclear interaction, clearly the necessary force can be achieved at a greater distance as atomic number increases, thus increasing the probability of the necessary degree of scattering. For an electron-electron interaction increased atomic number also increases the probability of scattering due to the increased quantity of electrons[72]. Also, as the specimen under investigation does not consist of a single atom, but instead possesses many atoms, the probability of a scattering event also increases as a function of the number of atoms per unit area[71].

$$F = \frac{1}{4\pi\varepsilon_0}\frac{q_1 q_2}{r^2} \quad (2.4)$$

where F is the electrostatic force between the two charged bodies, ε_0 is the permittivity constant, q_1 is the charge on the first body, q_2 is the charge on the second body and r is the distance between the two charged bodies.

Once the electrons have passed through the sample it is necessary to use a further series of apertures and lenses to project the electrons onto a screen, forming an image of the sample. The image which is formed is done so using either the unscattered electrons or the scattered electrons, which are known as bright field or dark field images respectively[75]. As the bright field image is composed of non-scattered electrons, lighter elements are shown clearly as many electrons illuminate that area of the image whereas heavier elements appear much darker due to the lack of electrons illuminating that area of the image. For dark field imaging the reverse is true.

Selected Area Diffraction (SAD) can also be used to obtain information about the crystal structure of crystalline areas of the sample. This can be achieved because the crystalline structure behaves as a diffraction grating for the electrons, causing some of them to be diffracted to certain angles which are determined by the size and orientation of the 'diffraction grating' experienced by the electrons. The image used in this technique is taken at the back focal plane rather than the image plane used normally for TEM. For single crystals the diffraction pattern appears as a series of regularly spaced maxima where constructive interference is occurring, with each corresponding to a particular diffraction condition of the crystal structure i.e. 100, -100, 211 etc. As the orientation of the diffraction

pattern is determined by the orientation of the crystal, additional points are present when there are two or more distinct crystals, such as a twinned crystal, as each crystal produces a distinct set of maxima. When dealing with crystalline nanoparticles the number of differently oriented crystals can be sufficiently large to produce a series of concentric rings, with each ring representing a particular Miller index[71].

Scanning electron microscopy (SEM) utilises an electron gun, apertures and electromagnetic lenses in the same way that TEM does, however there is an additional set of electromagnetic coils to scan the beam across the sample surface in a raster pattern[76]. Another difference between SEM and TEM is that SEM utilises either secondary or backscattered electrons rather than transmitted electrons. The type of electrons used to form the image for SEM affects the information which can be acquired from it due to the difference between the two types of electrons. When the electron beam interacts with the sample, an electron within it can become excited and be emitted as a low energy secondary electron[77]. Due to the low energy nature of these secondary electrons, if they are emitted from troughs in the sample surface fewer will be capable of escaping the sample than if they were emitted from peaks. As a result the peaks appear brighter than the troughs, generating the contrast necessary to observe structure[78]. Backscattered electrons occur when an electron undergoes one or more scattering events with nuclei within the sample, thus a greater proportion are produced within areas of the sample with higher atomic number[77]. Environmental scanning electron microscopy (ESEM) operates under the same principals as SEM, but allows the investigation of 'wet' samples. This is achieved by the use of differential pumping to allow an atmosphere in the sample chamber. This also entails the use of a modified detector which is capable of

detecting the electron avalanche which results from the interaction of secondary electrons with the gaseous atmosphere[79].

Scanning transmission electron microscopy (STEM) is a combination of aspects of both TEM and SEM. It utilises the raster scan of the electron beam used in SEM and the transmitted electrons used by TEM. In a standard TEM, dark field images are formed using only a portion of the scattered electrons as an aperture is used. With STEM an annular detector can be utilised, which is capable of detecting a greater portion of the scattered electrons[75]. It is possible to use an annular detector to detect electrons which have been scattered to high angles, a technique called High-Angle Annular Dark Field (HAADF). As the diffracted electrons used for SAD primarily occur at low angles, these are mostly excluded from HAADF measurements. The benefit of doing this is that the occurrence of electrostatic scattering is approximately proportional to atomic number (Z) squared thus it can be used for accurate elemental mapping of samples[80].

2.2 X-Ray Diffraction

X-Ray Diffraction (XRD) is a crystallographic technique that uses an x-ray beam to probe the structure of materials. This technique relies upon the constructive interference that occurs as a result of the interaction of the x-ray beam with the material[81,82]. Constructive interference occurs when two diffracted x-rays are in phase with each other, a condition that is fulfilled when the relationship between the x-ray wavelength and the lattice spacing obeys Bragg's Law (Equation 2.5)[83], causing peaks appear at certain angles. From this the d-spacing

of a material can be determined by sweeping the x-ray beam through a large angle, provided that the x-ray wavelength is both constant and known. For a given crystal multiple peaks will typically appear, each created by a different crystallographic orientation. The angle at which these peaks occur can be used to help identify elements within a material, determine crystalline orientation or measure the d-spacing of a material; the latter can be used to determine the structure of alloyed materials or to measure the degree of strain within a material's structure (provided that it is of a uniform nature)[84]. XRD crystallographs have been determined for many materials and the peak locations and relative intensities can be found in several databases, thus the above methods of analysis can be completed by matching, or possessing systematic differences relative to, one of these references.

$$\lambda = 2d_{hkl}\sin\theta_B \tag{2.5}$$

where λ is the x-ray wavelength, d_{hkl} is the d-spacing of a particular Miller index of the crystal and θ_B is the Bragg angle.

It is also possible to use XRD to obtain information about crystallite size which, particularly in nanoparticulate systems, can equate to particulate size. This can be achieved through the application of the Scherrer equation (Equation 2.6) to the full width at half maximum (fwhm) of the peaks as the degree of peak broadening increases as the crystallite size decreases. However this form of analysis is not without difficulty as the value of the K-factor differs depending upon the crystalline structure and shape[85]. Peak broadening can also originate from other sources such as the instrumentation and non-uniform strain[86].

$$\beta = \frac{K\lambda}{l\cos\theta_B} \quad (2.6)$$

where β is the fwhm of the peak, K is the K-factor, and l is the crystallite diameter.

2.3 X-Ray Photoelectron Spectroscopy

X-Ray Photoelectron Spectroscopy (XPS) is an analysis technique which utilises the photoelectric effect, the emission of electrons from a material when light is incident upon it, to investigate the elemental composition of a substance[87]. This is possible because the electrons which are emitted by each element have specific energy as shown by Einstein's photoelectric equation (Equation 2.7). The work function here is determined by the strength of the binding between the photoelectron and the nucleus prior to emission. For XPS, a more useful description of this relationship is shown in Equation 2.8, although for practical purposes an additional work function is required to account for the energy lost as the electron is absorbed by the instrument's detector[88]. This leads to each element producing a characteristic 'fingerprint' where electrons will be emitted at particular energy depending upon their energy state within an atom, i.e. 1s, 2s, 2p etc, which do not all occur in the same abundance, but possessing of repeatable proportions between such peaks for a particular element[89]. Due to this relationship, a monochromatic x-ray source is important to limit the uncertainty of electron binding energy introduced into the measurement from the x-ray source. As it is the binding energy of a photoelectron that provides information on the sample, XPS experiments typically present data using this rather than the kinetic energy, thus allowing for easier comparison if different x-ray sources are used[90]. However XPS is

limited to the near surface region of a material. Whilst the x-rays are capable of penetrating deeply within the sample, the photoelectrons can only travel a short distance through a material before undergoing an energy loss event. When such an event occurs to a photoelectron it is rendered ineffective for analytical purposes. As the probability of an energy loss event occurring increases as a factor of sample density, the limit of detection distance varies but is typically <10 nm[91].

$$K = h\nu - \phi \tag{2.7}$$

where K is the kinetic energy of the photoelectron, h is Planck's constant, ν is the frequency of the incident light and ϕ is the work function of the material.

$$E_{binding} = E_{photon} - E_{kinetic} \tag{2.8}$$

where $E_{binding}$ is the binding energy of the electron, E_{photon} is the energy of the photon and $E_{kinetic}$ is the kinetic energy of the electron.

The procedure itself requires an analysis chamber which is maintained at ultra-high vacuum, an x-ray source and an electron detector. Ultra-high vacuum is necessary to ensure that the emitted electrons are not involved in collisions with ambient materials which would reduce the signal intensity[92]. The x-ray source provides the photons which cause the photoelectric emission to occur. Any electrons which have greater binding energy than the x-ray energy are not emitted, thus for heavier elements the innermost orbitals are not investigated. Electron beam intensity is determined using an electron multiplier; however this alone is not capable of determining the binding energy of the detected electrons. Typically the kinetic energy of the emitted electrons is determined through the use of a hemispherical analyser[93].

This consists of an inner anodic and an outer cathodic hemispherical plate, with slits at the entry and exit. Electrons passing through the slit into this arrangement experience attraction towards the inner plate and repulsion from the outer plate, thus their path is deflected towards the inner plate. The hemispherical nature of the plates allows for electrons to be capable of passing through this arrangement without impacting either plate. Yet if the electron kinetic energy is too great it will disperse towards the outer plate and if it is too low it will disperse towards the inner plate, in either case these electrons do not pass through the exit slit and thus are not detected. By altering the plate potential it is possible to alter the kinetic energy that allows for successful passage, thus any detected electrons are known to possess the kinetic energy dictated by the plate potential. Throughout the course of an XPS experiment the plate potential is gradually stepped to only allow electrons with particular kinetic energy to be detected, thus an intensity vs. kinetic energy plot can be created[93]. However it is the electron binding energy which provides the elemental 'fingerprint', not the kinetic energy, for photoelectrons[90].

During an XPS experiment it is possible to detect electrons which were emitted from the sample, yet are not photoelectrons. These are known as Auger electrons. Auger emission occurs as a result of the electronic relaxation within an atom after photoemission has occurred[94]. When photoemission occurs with an electron that is not in the least strongly bound energy state, a less strongly bound electron will relax into the hole which has been left by the emission. When this occurs some energy is released. This energy emission can occur as either emission of a photon or an Auger electron, thus for Auger emission two electrons and a hole are involved[95]. The amount of energy to be emitted is determined by

the energy state of the hole and the energy state of an electron prior to its relaxation. For Auger emission a portion of this energy is required to overcome the binding energy and the remainder is the kinetic energy. As a result of this the electron kinetic energy is determined by the energy states of the hole, relaxing electron and the emitted electron and is typically denoted in shell terminology, e.g. KLM Auger emission involves a K shell hole being filled by an L shell electron resulting in the emission of an M shell electron[90]. The kinetic energy of Auger emission is independent of x-ray energy due to being the result of intra-atomic interactions, thus Auger electron data should be presented as kinetic energy[90].

XPS is a technique which is capable of high resolution, which is achieved by control of the electron analyser. The increase of resolution comes at the cost of sensitivity, thus it is impractical to do a high resolution scan over the entire energy spectrum, but focussing upon peaks produced by an element of interest can yield additional information[95]. Differences in electron binding energy can arise as a result of interatomic interaction[90]. If an atom has bonded with a more electronegative element the bonding electrons are more strongly attracted to the electronegative element. The result of this is that the binding energy of the non-bonding electrons increases for the electrons of the less electronegative element and decreases for the electrons of the more electronegative element[95]. The difference in binding energy that this causes is sufficiently large that it can be detected, thus high resolution XPS can provide information about the bonding environment of a particular element within the sample.

A portion of the XPS 'fingerprint' is due to spin-orbit splitting which occurs due to the total angular momentum quantum number, j, (Equation 2.9) being capable of possessing either of

two values when the angular momentum, l, (Table 2.1) has a non-zero value i.e. not an s orbital[95]. Where this occurs the ratio of peak areas is determined by the ratio of the degeneracy of the final states as described by Equation 2.10[96]. Where doublet peaks overlap the deconvolution of the spectra can be greatly assisted by the application of relative parameters for the area and a fixed value for energy difference between doublet peaks[97].

$$j = |l \pm s| \tag{2.9}$$

$$g_j = 2j + 1 \tag{2.10}$$

where j is the total angular momentum quantum number, l is the angular momentum quantum number (which possesses an integer value, Table), s is the spin momentum quantum number (which possesses a value of 1/2) and g_j is the degeneracy of the final state.

Table 2.1, Angular momentum quantum number value and its assignation in subshell notation.

Angular momentum quantum number (l)	Assignation
0	s
1	p
2	d
3	f

2.4 Mass Spectrometry

Mass spectrometry is an analytical technique which can be used to determine the amount and/or type of chemicals present within a sample. For this to be achieved it is necessary to ionise the sample, which then allows for the determination of the mass to charge ratio[98]. For qualitative analysis the mass to charge ratio provides information about the materials present, whereas quantitative analysis typically uses a standard of known quantity to act as an internal reference so that quantitative information can be extracted from the relative peak intensities[99]. For this to be achieved there are three important steps, ionisation, separation and detection[98]. These are important as the separation is achieved based upon the mass to charge ratio, thus the sample requires ionisation for this to be possible. The simplest of these steps is detection, which is typically achieved using an electron multiplier[100], whereas ionisation and analysis can be achieved in a variety of ways, each best suited to certain applications.

Ionisation can be achieved through a variety of methods including, but not limited to, electron ionisation, electrospray ionisation, fast-atom bombardment and inductively coupled plasma. The ionisation method for a sample should be selected based upon the properties of the sample. Hard ionisation methods such as electron ionisation (EI) apply a large amount of energy to the sample and cause a large degree of sample fragmentation, whereas softer methods such as electrospray ionisation (ESI) cause less fragmentation. Both are well suited to qualitative analysis of organic materials as some degree of sample fragmentation can aid in identification of unknown species; softer techniques are better suited to larger biomolecules. Ionisation methods can also lead to near-complete sample decomposition, an

example of this is inductively coupled plasma (ICP). This is best suited to quantitative analysis of inorganic materials as the decomposition leads to a much simpler spectrum, reducing the possibility of overlapping spectral lines which would complicate quantification; however, the decomposition hinders the collection of qualitative information[101].

There are also a large selection of separation techniques that can be used in mass spectrometry such as quadrupole (or hexa- and octo-pole), time of flight, and a range of ion trap systems. Each system has greater suitability for certain applications than others; ion traps can be used for successive fragmentation of large molecules, time of flight has an extremely high mass limit and quadrupole systems allow for continuous sampling. In each case separation is done on the basis of mass-to-charge ratio rather than mass alone, thus doubly (or more) ionised species can increase the complexity of analysis. The mass-to-charge ratio separation is achieved by the application of a magnetic field which may be static or dynamic. Due to the possibility of interfering ions it is sometimes necessary to utilise a collision cell to cause the removal of uninteresting species which originate either from the sample matrix or the ioniser; quadrupole type instruments are particularly well suited to such a technique[102].

As this work utilised mass spectrometry for the purpose of quantification of inorganic materials, an ICP ioniser was used in conjunction with an octopole separator. The octopole separator contained He to function as a collision cell, removing any larger polyatomic ions[103].

2.5 Superconducting Quantum Interference Device (SQUID) Magnetometry

Population averaged magnetic measurements were conducted using a Quantum Design Magnetic Property Measurement System (MPMS). Samples are loaded into the MPMS via the use of a low magnetic signature straw, which is attached to the end of a long sample rod. Initial work was carried out using cling film to wrap up samples, and then affix them within a hole cut roughly halfway along the straw. This method was later refined by using gelatine capsules (Agar Scientific) to contain the sample, and these were held in place using another straw which was cut into pieces and used to hold the capsule halfway along the straw. The benefit of this alteration was that the sample containment had a more consistent signature and the local environment was more consistent as there was no longer any need for a hole in the straw.

Once the sample is properly affixed, the sample rod is lowered vertically into a long, narrow sample chamber via an airlock. This procedure is enacted whilst the instrument is at 200 K or greater, and as rapidly as possible to limit exposure to atmospheric water vapour which can freeze within the chamber. Once the sample is installed it is necessary to ensure that the chamber is properly purged of gas.

The MPMS consists of a superconducting magnet to generate large fields and a SQUID, which is inductively coupled to the sample via a superconducting detection coil[104]. A superconducting magnetic shield is present to ensure that the SQUID is not subjected to effects of the superconducting magnet, or any external magnetic fluctuations. The superconducting detection coil is comprised of a wire with three loops, the upper and lower

loops consist of a single turn made clockwise and the centre loop two turns counterclockwise.

A DC SQUID (as used in this work) consists of a superconducting circuit passing a bias current, I_B, which is split equally along two parallel paths; provided there is no external influence (Figure 2.1). Each path contains a Josephson Junction, which is an insulating or normally conducting junction between two superconductors. This allows the passage of a supercurrent, the non-dissipative current that flows through a superconductor, provided it does not exceed the value I_C, which is the critical current of that junction[105]. When the superconductor experiences the magnetic flux from the sample, a screening current, I_S, arises which flows in a manner to expel the magnetic field that it is experiencing[106]. As a result of this screening current the two Josephson Junctions experience different currents, with one experiencing $I_S+I_B/2$ and the other $I_S-I_B/2$. If I_B is chosen appropriately $I_S+I_B/2$ will exceed I_C, resulting in a voltage being experienced across one Josephson Junction[107,108]. The magnitude of this voltage, combined with the knowledge of I_B, allows for the determination of I_S and thus the magnetic flux originating from the sample.

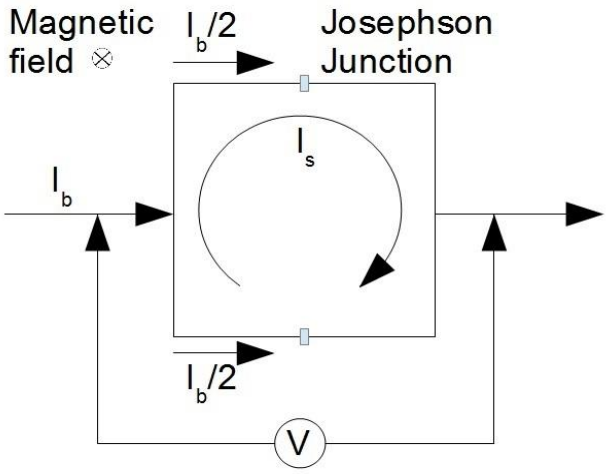

Figure 2.1, a DC SQUID with bias current, I_b, where the magnetic field is travelling into the page leading to a screening current, I_s, that in turn causes a potential difference, V, to occur.

The system is calibrated using a piece of material of known mass and magnetic susceptibility[104]. For the measurement itself, the sample is moved through the detection coil and the raw data generated has an amplitude which is a function of position. The analysis method requires the application of a model to convert the voltage measured into data informing about the magnetic moment, which assumes that the magnetic moment of the sample does not change in sign or value during the measurement[109]. Figure 2.2 shows the layout of the coils and the typical raw voltage measurement against position which the instrument uses to calculate the sample moment.

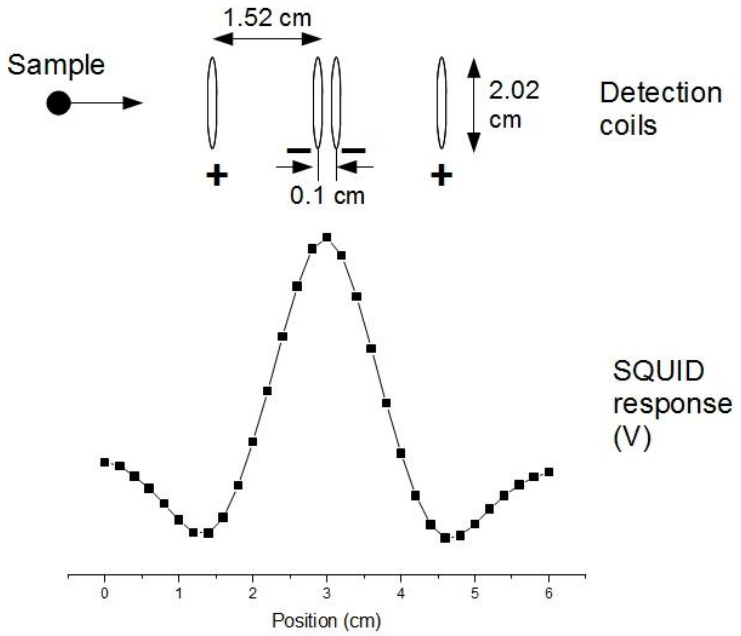

Figure 2.2, the z position of the superconducting detection coil loops and the ideal SQUID response generated by a sample with positive magnetic dipole moment. This signal would be inverted for a sample with negative dipole moment.

During operation, a magnetic field, H, is applied to the sample and the change in its magnetic flux is altered as a result. From this it is possible to determine the magnetisation, M, of the sample as this is related to both the applied field and the magnetic flux observed. If the magnetic susceptibility, χ, where χ=M/H, is plotted over several values of H it is possible to determine the type of magnetism present in the sample and its strength. A diamagnetic (Figure 2.3a) material will produce a negative value for χ and a paramagnetic (Figure 2.3b) material will produce a positive value for χ, both of which are independent of H. With a ferromagnetic (Figure 2.3d) material the plot of M against H will not produce a slope of constant gradient and also possesses non-reversible behaviour i.e. when the applied field is scanned, the sample moment will pass through zero at a field value of $\pm H_c$, where H_c is the

coercivity of the sample. The degree of hysteresis can be used to determine if the material is a hard or soft ferromagnet, where hard ferromagnets have a high coercivity (magnetism remaining when a previously applied field is removed), and soft ferromagnets have a low coercivity. A superparamagnetic (Figure 2.3c) material has the same non-constant M vs. H plot but without any hysteresis, i.e. H_c is zero.

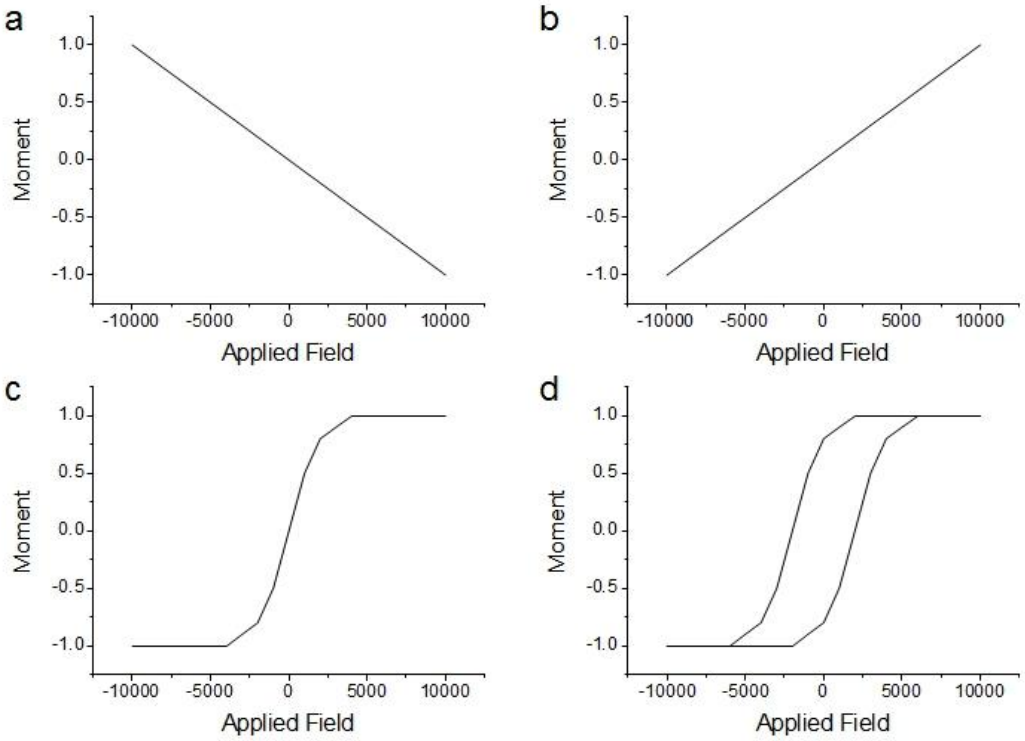

Figure 2.3, typical moment (M) vs. applied field (H) plots for a diamagnetic (a), paramagnetic (b), superparamagnetic (c) or ferromagnetic (d) sample.

2.6 Muon Spin Rotation (μSR) Spectroscopy

Internal magnetic measurements were conducted using muon spin rotation (μSR), primarily at the Paul Scherrer Institut (Switzerland) using the General Purpose Surface-Muon Instrument (GPS). The technique uses the muon as a local magnetic probe. This is achieved by the implantation of a muon into the sample which interacts with the magnetic field at that position. The implantation of muons is achieved when a beam of spin polarised muons is incident upon a sample of sufficient depth to stop the muons. Should such a thickness not be achievable due to small sample quantities, as was the case for this work, additional retardation was achieved through the application of silver degraders between the sample and the beam source. Silver is chosen because it has a very small nuclear moment, thus muons which are entirely stopped within the silver produce negligible signal compared to the sample[110].

The muons utilised by GPS possess a momentum of 28 MeV/c[111] and an energy of 4.1 MeV[112], however upon interaction with the sample they lose energy through ionization of atoms and electron scattering, and then by electron capture and loss. The whole process takes place in under a nanosecond[113]. Once the muon has come to rest it experiences Larmor precession, which is the precession of the muon spin around an external magnetic field (in this case the local magnetic field at the point of the sample where the muon is located); with a frequency dependent upon the magnetic field strength[114].

The μSR experiments require a known starting point and a way to determine the orientation of the spin over time. To obtain a known starting point the muons utilised are of known

polarization, provided by the manner in which the muons are produced. A proton beam provided by a synchrotron is fired at a graphite target which results in the formation of pions, π^+ which have a halflife of 26 ns[115]. Each pion then undergoes decay to a positive muon and a muon neutrino, where the decay particles are emitted at 180° to each other and have spin aligned antiparallel to their momentum[113,116]. The muons possess known energy as the muons utilised for this work originate from pions with no momentum, i.e. pions located at the graphite surface[112].

Muon spin orientation following implantation cannot be determined until the point where it decays; it has a halflife of 2.2 μs. Unlike the pion, the muon undergoes a three body decay process, meaning there are 3 particles emitted by the decay, a positron, muon neutrino and an electron antineutrino[115]. This is inconvenient as the energy is 'parcelled' into 3 directions meaning that the particle energies and angles between particles for one decay event can be very different to those of other decay events. The positron emission occurs preferentially in the direction of the muon spin orientation and the greater the energy it possesses the closer it will typically be in emission orientation to the muon spin orientation had been. The expected anisotropy of the positrons is about 30 %[117], see Figure 2.4 for expected distribution. This leads to an expected asymmetry of 30 %, however in practice a lower value, around 22-27 %, is found due to the nature of each instrument[118,119].

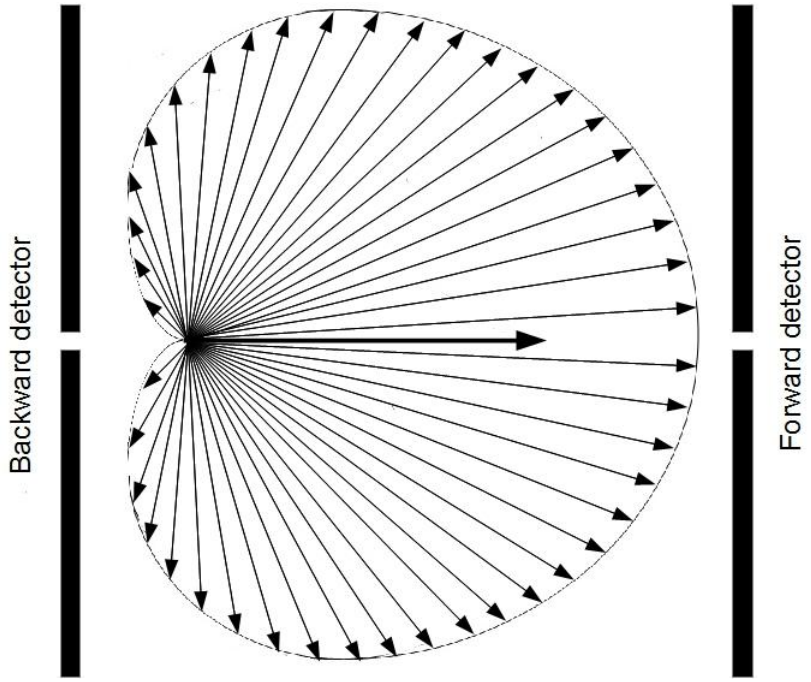

Figure 2.4, the angular distribution of emitted positrons with respect to the initial muon-spin direction (bold central arrow). Length of arrows gives an indication of positron energy for any direction of emission. Adapted from Blundell (1999)[113]. Gaps in the detector plates indicate holes for the muon beam to pass through.

A μSR instrument monitors the time at which a muon or muon pulse enters the sample chamber and is equipped with an array of scintillation detectors to determine the time and position of any positron emissions. Each scintillation detector is a piece of plastic which will emit light when struck by a positron, and is connected to a photomultiplier tube via an acrylic light guide[120]. By carrying out measurements of millions of decays it is possible to form a statistically accurate representation of the muon spin orientation and its evolution with time.

When analysing μSR data it is typical to plot the time dependent decay asymmetry for the

recorded counts of the forward (N_F) and backward (N_B) detectors, as described by the relationship in Equation 2.11.

$$a(t) = \frac{N_F(t) - \alpha N_B(t)}{N_F(t) + \alpha N_B(t)} \tag{2.11}$$

where α describes the relative efficiencies of the detectors, and is measured independently for each sample as it is affected by sample position relative to the detector arrangement.

The determination of the value α is achieved through the application of a small external field being applied transverse to the muon polarisation. As this field is of known strength, and muons oscillate at 136 kHz/mT, it dictates what the relative values of the forward and backward detectors should be for any particular instance[115]. For the analysis of samples it is necessary to fit a function to the data that describes the time dependence of the asymmetry, see Equation 2.12. Values from $G_z(t)$ can then be plotted against a relevant parameter, such as applied field or temperature, to extract information about the sample.

$$a(t) = a_{full} G_Z(t) \tag{2.12}$$

where a_{full} is the full asymmetry for the GPS spectrometer and $G_Z(t)$ is a function describing the interaction between the muon spin polarisation and the local magnetic field with respect to time.

3. REDUCTION OF PLATINUM BY *ESCHERICHIA COLI*

Many types of biomass have been shown to be capable of bioreduction of platinum. With bacteria, hydrogenases are known to play an important role, however the exact mode of operation is not known. This study investigates the use of *Escherichia coli* for bioreduction of Pt(IV) using 5 % or 10 % platinum loadings (w/w %), hydrogen or formate as electron donor and a biosorption duration of 30 or 60 minutes before addition of electron donor. Bio-Pt(0) samples were analysed using transmission electron microscopy, scanning electron microscopy, x-ray diffraction and x-ray photoelectron spectroscopy to gain insight into the interaction between platinum and the supporting biomass.

3.1 Introduction

It has been shown that when bacteria are used to assist in the formation of metal nanoparticles, there are many parameters which can impact upon the manner in which they are formed. This includes metal precursor type and concentration[24,63], reducing agent type and concentration[7,35], presence and type of competing ions[5], pH[13,22] and the species of bacteria[29,31] which is being used. Furthermore, metabolic engineering can be used to 'steer' nanoparticle activity. For example cells of *Escherichia coli* synthesised a 'bio-Pd' catalyst that performed poorly in a polymer electrolyte fuel cell (PEFC) after sintering, whereas Pd made by an engineered strain produced more than three times the power output under load when used as the anodic catalyst[34].

Chloroplatinic acid is the most relevant Pt complex to industrial leaching processes[121], thus formed the focus of this study. Whilst alternative complexes have been shown to have an impact upon the Pt uptake[24], the greater difficulty and cost to produce such materials is a hindrance to potential industrial scale up. Solution pH is an important parameter as this has been shown to produce superior Pt uptake at pH ≈ 2[40,122] and Orozco *et al.* (2010)[34] have shown that cell viability is maintained under such metal sorption conditions; however, cell toxicity of precious metal complexes[64] is a major factor as inferior reduction capabilities of dead cells compared to live cells was observed due to the loss of metabolic components[5].

The objective of this work was to investigate the effect of Pt(IV) challenge duration and reducing agent type and quantity on the reduction of Pt(IV) by *E.coli*; as well as the final Pt loading at a constant challenge concentration of 2 mM Pt(IV). Pt deposition was investigated using transmission electron microscopy (TEM), environmental scanning electron microscopy (ESEM), X-ray diffraction (XRD) and X-ray photoelectron spectroscopy (XPS). Use of the latter surface-specific technique showed previously that Pt(IV) coordinates to specific ligands on the bacterial cell surface and that some Pt(IV) reduction occurs in cell surface layers of *Desulfovibrio desulfuricans* in the absence of applied electron donor[25]. This investigation focussed upon the effect of the conditions of Pt(IV) challenge upon the resulting bio-Pt to obtain information regarding the interaction between the Pt and the cells.

3.2 Methods and Materials

3.2.1 Growth of Bacteria

E.coli MC4100 was maintained at 4 °C on agar plates. Cultures were shaken aerobically in nutrient broth (NB) no. 2 (Oxoid) (37 °C; 24 hours;180 rpm). These were then used to inoculate 5 x 200 mL of minimal medium (composition shown below) and grown anaerobically (37 °C; 44 hours). Each culture was transferred into 1.8 litres of minimal medium, grown anaerobically at 37 °C, harvested by centrifugation during the mid-exponential growth phase (O.D. ≈ 0.2; full growth curve shown in appendix I), washed three times in 4-morpholinepropanesulfonic acid (MOPS)/NaOH buffer (20 mM, pH 7.0) and concentrated into a small volume of the same buffer. The resulting samples were degassed, then stored under oxygen free nitrogen (OFN) at 4 °C until use (within 24 hours). The optical density at 600 nm was measured by UV-vis spectroscopy, allowing for the calculation of the dry mass of cells per unit volume of solution[5].

Minimal media for *E.coli*: 12 g Tris, 0.62 g KCl, 0.96 g $(NH_4)HPO_4$, 0.063 g $MgSO_4.7H_2O$, 0.33 mg $FeSO_4.H_2O$, 4 g sodium fumarate, 5 mL glycerol and 3.6 g glucose with distilled water to bring volume to 1000 mL and pH adjusted to 7.2 using HCl. Glucose was sterilised separately.

3.2.2 Biosorption and Bioreduction of Platinum

Preliminary biosorption tests established that the rate of biosorption of Pt(IV) decreased after 30 minutes (see appendix II), thus cells were challenged with Pt(IV) for a minimum duration of 30 min. The concentration of Pt(IV) was 2mM throughout and different final loadings of Pt (5 % and 10 % by mass) were obtained by adjustment of the Pt:biomass added to Pt(IV) solution in 10 mM HNO_3 (ratio of HNO_3:MOPS/NaOH 3:1; final pH was 2.5).

Platinum solution was degassed and stored under OFN at 37 °C until use. An appropriate volume of biomass in MOPS/NaOH was added to the platinum solution to achieve a platinum quantity relative to the biomass of 5 % or 10 % w/w, as appropriate. An additional amount of MOPS/NaOH buffer (degassed and stored under OFN) was supplemented to achieve the 3:1 ratio of platinum solution to MOPS/NaOH across all samples. During biosorption the samples were maintained at 37 °C, 180 rpm for 30-60 minutes, dependent upon sample.

Hydrogen gas (BOC) or sodium formate (Sigma) were used as reducing agent. Hydrogen gas was sparged for 30 minutes then pressurised at 1 bar (providing ~20 times or 40 times a molar excess required for a complete reduction of platinum present for 10 % and 5 % Pt loadings respectively). Where formate was used it was added as 2.5 times molar excess from a 500 mM sterilised anaerobic stock solution, producing 15 mM final formate concentration. All samples were allowed 3 days at 37 °C, 180 rpm for reduction to occur. The samples were prepared as shown in Table 3.1. The post-reduction Pt content of the supernatant was monitored using the tin chloride assay[23]. All experiments were done three times.

Table 3.1, bioreduction conditions.

Sample	Pt loading (%)	Biosorption duration (min)	Electron donor
1	10	30	H_2
2	5	30	H_2
3	5	60	H_2
4	10	30	Formate
5	5	30	Formate
6	5	60	Formate
7	Pt-free control		

3.2.3 Analytic Techniques

For transmission electron microscopy (TEM), samples were centrifuged and fixed in 2.5 % glutaraldehyde in 0.1 M cacodylate buffer, without the use of any staining agents. Samples were set in resin, sectioned and placed onto copper grids for investigation using a JEOL 1200EX microscope (80 keV).

For scanning electron microscopy (SEM) samples were washed three times (aq.) and resuspended in a small volume of acetone overnight for drying in air. Dried samples were ground using an agate mortar and pestle, dropped onto carbon tape on a metal stub and sputtered with gold for conductivity. Samples were analysed using a Philips XL-30 FEG environmental SEM.

Sample preparation for X-ray diffraction (XRD) was done by washing the sample three times in water. Washed sample was resuspended in a small volume of ultrapure water which was used for a vapour deposition process by applying the sample (20 µl) onto silicon wafer (≈1 cm^3)(using a lamp to assist in water evaporation). This was repeated until a sufficient film was present for analysis. X-ray diffraction measurements were carried out using a Bruker D2 diffractometer with a Lynxeye detector and a rotation stage operating at 15 rpm using a Co Kα x-ray source and EVA software. Scans were conducted between 40-50° 2θ, with each scan taking 13 minutes. XRD analysis used the (111) peak, with curve fitting being done using Origin software.

X-ray photoelectron spectroscopy (XPS) used samples prepared as for XRD. XPS data was collected (National EPSRC users service (NEXUS) facility, University of Newcastle, UK) using a Kratos Axis Nova equipped with a monochromated aluminium anode. Survey scans were done with a pass energy of 160 eV with 3 sweeps over each sample site using 1 eV steps. High resolution scans were done with a pass energy of 20 eV with 10 sweeps over each sample site using 100 meV steps. Charge neutralisation was utilised for all samples. For each sample, measurements were made at three points per sample. Data was collected using a survey scan to measure the entire range of binding energy, and higher resolution scans were conducted over the regions where C 1s, O 1s, N 1s and Pt 4f peaks are located. All high resolution scans were binding energy (BE) corrected such that the C-H 1s peak was located at 284.8 eV.

Analysis of the XPS data was done using CasaXPS. For all analysis a Shirley background was used. The elemental peaks were fitted using components with the GL30 lineshape, a mixture

of Gaussian and Lorentzian lineshapes. The exception to this was the Pt(0) peaks which were fitted with an LA(1.2,85,70) lineshape, an asymmetrical Lorentzian lineshape where the first two values within the brackets determine the degree of asymmetry of the lineshape and the third value within the brackets determines the width of the Gaussian component[123]. This was necessary due to the presence of the conduction band in a metal which provides a range of energy states for electrons to reside, allowing for a range of binding energies as compared to the well defined energy states for core electrons. As the Pt 4f peaks consisted of a doublet, additional constraints were used for this. For each Pt $4f_{7/2}$ peak (IV, II and 0) the corresponding Pt $4f_{5/2}$ peak was constrained to an area equal to 0.75 of the 7/2 peak[124], a binding energy 3.3 eV greater than the 7/2 peak[125] and fwhm equal to that of the 7/2 peak. For all high resolution scans the component peak fwhm was constrained to be no greater than 2.1 eV to ensure meaningful fitting of peaks.

3.3 Results and Discussion

Prior to reduction, the platinum solution/biomass mixture possessed the pale appearance typical of *E.coli.* This was unchanged during the biosorption process. After the addition of a reducing agent there was a distinct change in colouration with the mixtures becoming darker over 2-8 hours and 24-72 hours for the hydrogen and formate reduced samples respectively (Figure 3.1). Notably, while formate-reduced sample at 10 % Pt loading (sample 4, Figure 3.1) developed a black colouration, the samples loaded to 5 % Pt (samples 5 and 6, Figure 3.1e and f) did not. A similar but much weaker trend can be observed with the hydrogen reduced

samples. In each case the tin chloride assay revealed that a negligible quantity of Pt remained within the supernatant after reduction.

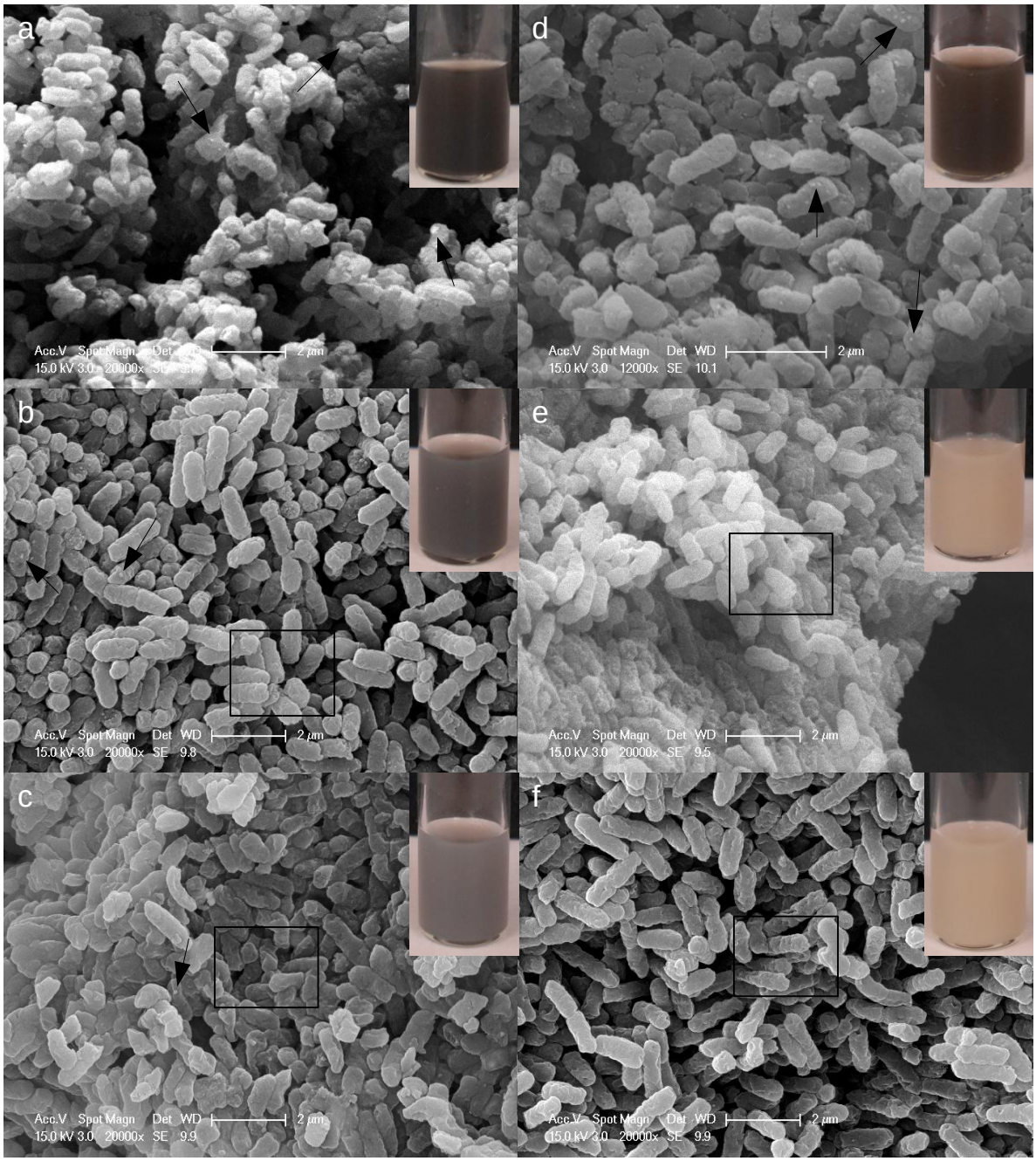

Figure 3.1, ESEM images with optical appearance inset. a is sample 1, b is sample 2, c is sample 3, d is sample 4, e is sample 5 and f is sample 6 as described in Table 3.1. Some protrusions are indicated with arrows and boxes show the location of images in Figure 3.2.

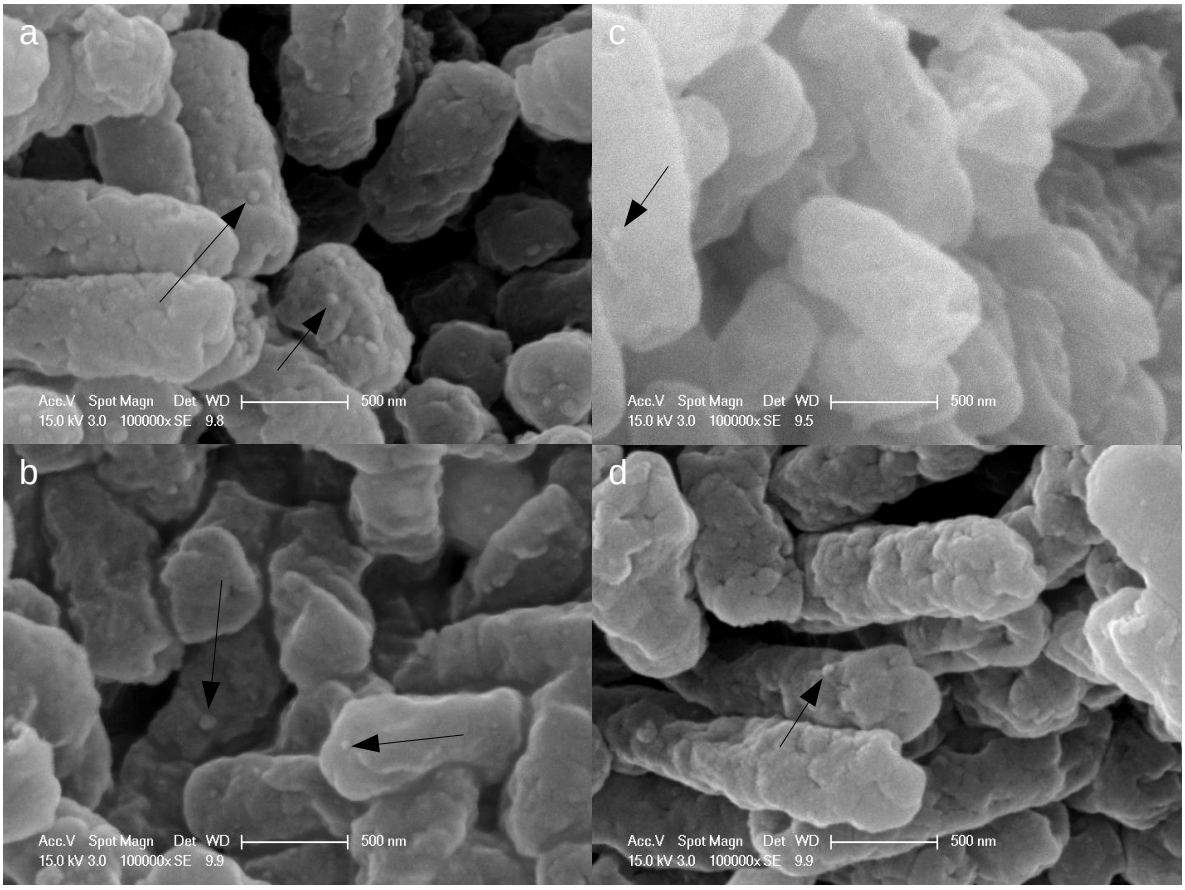

Figure 3.2, ESEM images at high magnification. a is sample 2, b is sample 3, c is sample 5 and d is sample 6 as described in Table 3.1. Some protrusions are indicated with arrows.

Scanning electron microscopy (SEM) investigation (Figures 3.1 and 3.2) revealed the presence of protrusions upon the surface of the biomass which are both more prominent and more plentiful upon the surface of the darker coloured preparations. For the 5 % loaded samples there is a difference between the hydrogen-reduced (samples 2 and 3, Figure 3.1b and c, Figure 3.2a and b) and the formate-reduced (samples 5 and 6, Figure 3.1e and f, Figure 3.2c and d) samples, suggesting that the reduction mechanism differs.

Transmission electron microscopy (TEM) was used to gain insight into the Pt distribution throughout the cells. The TEM images (Figures 3.3 and 3.4) found that samples 1 and 4 (10 %

Pt) show the greatest quantity of cell-surface bound platinum, mirroring the earlier findings. The 5 % loaded hydrogen-reduced samples, Figure 3.3b and c and Figure 3.4b and c, possess areas of platinum present at, or near, the cell surface. Due to the lower platinum proportion compared to sample 1, these platinum sites are either smaller (sample 2) or fewer in number (sample 3), where the platinum is primarily located on a few cells which are extremely heavily loaded, which is likely the result of autocatalytic reduction occurring at dominant Pt seed sites[126]. The 5 % loaded formate-reduced samples (samples 5 and 6; Figure 3.3e and f respectively and Figure 3.4e and f respectively) possess little to no cell-surface bound platinum, instead platinum is distributed throughout the cells. The 10 % loaded formate-reduced sample (sample 4; Figure 3.3d and Figure 3.4d) has the Pt widely distributed throughout the cells, although there are still many cell-surface bound Pt sites. These results show that there is a difference in the way the two reducing agents affect the Pt nanoparticle formation.

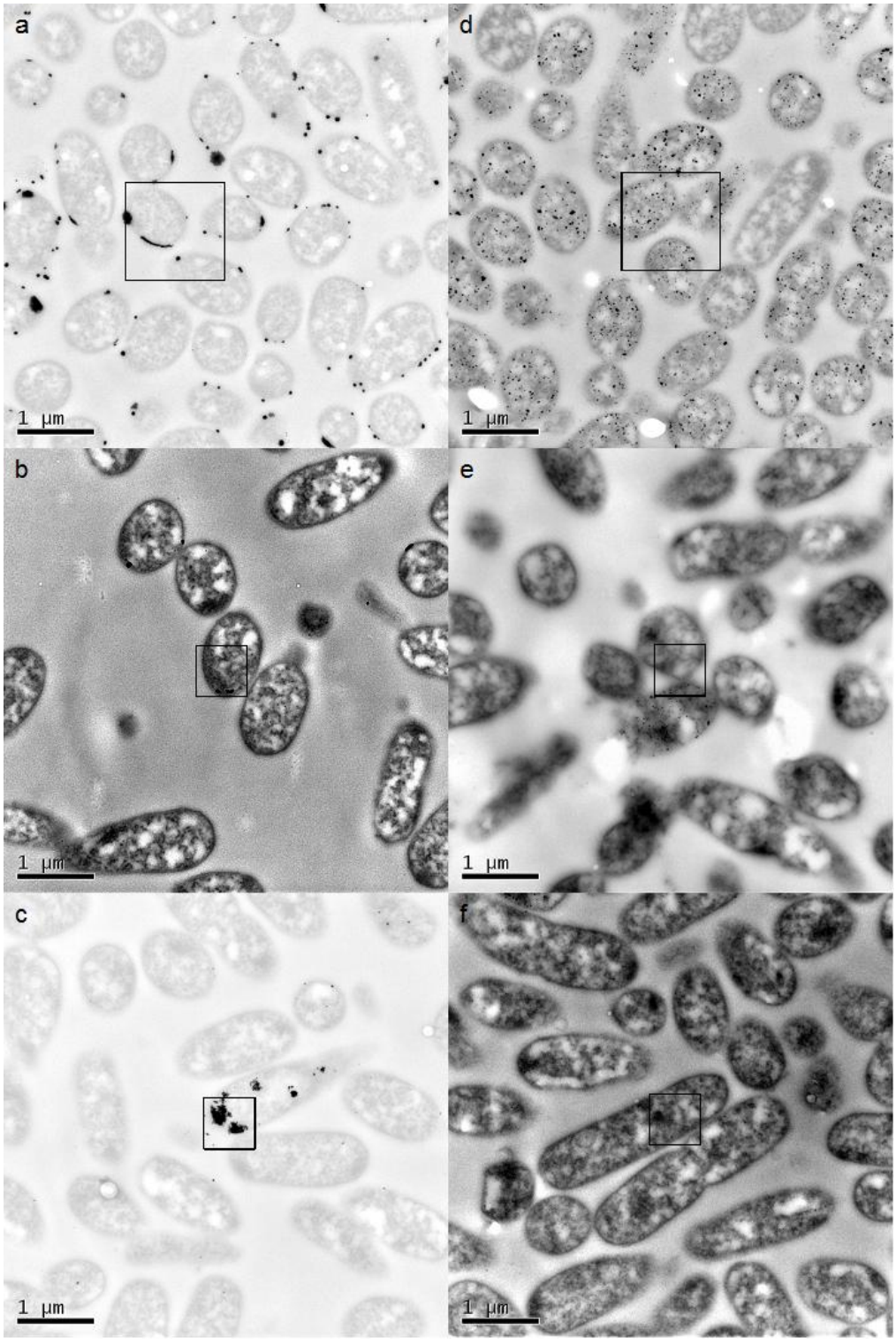

Figure 3.3, TEM images of unstained bio-platinum samples. a is sample 1, b is sample 2, c is sample 3, d is sample 4, e is sample 5 and f is sample 6 as described in Table 3.1. Boxes indicate the location of images in Figure 3.4.

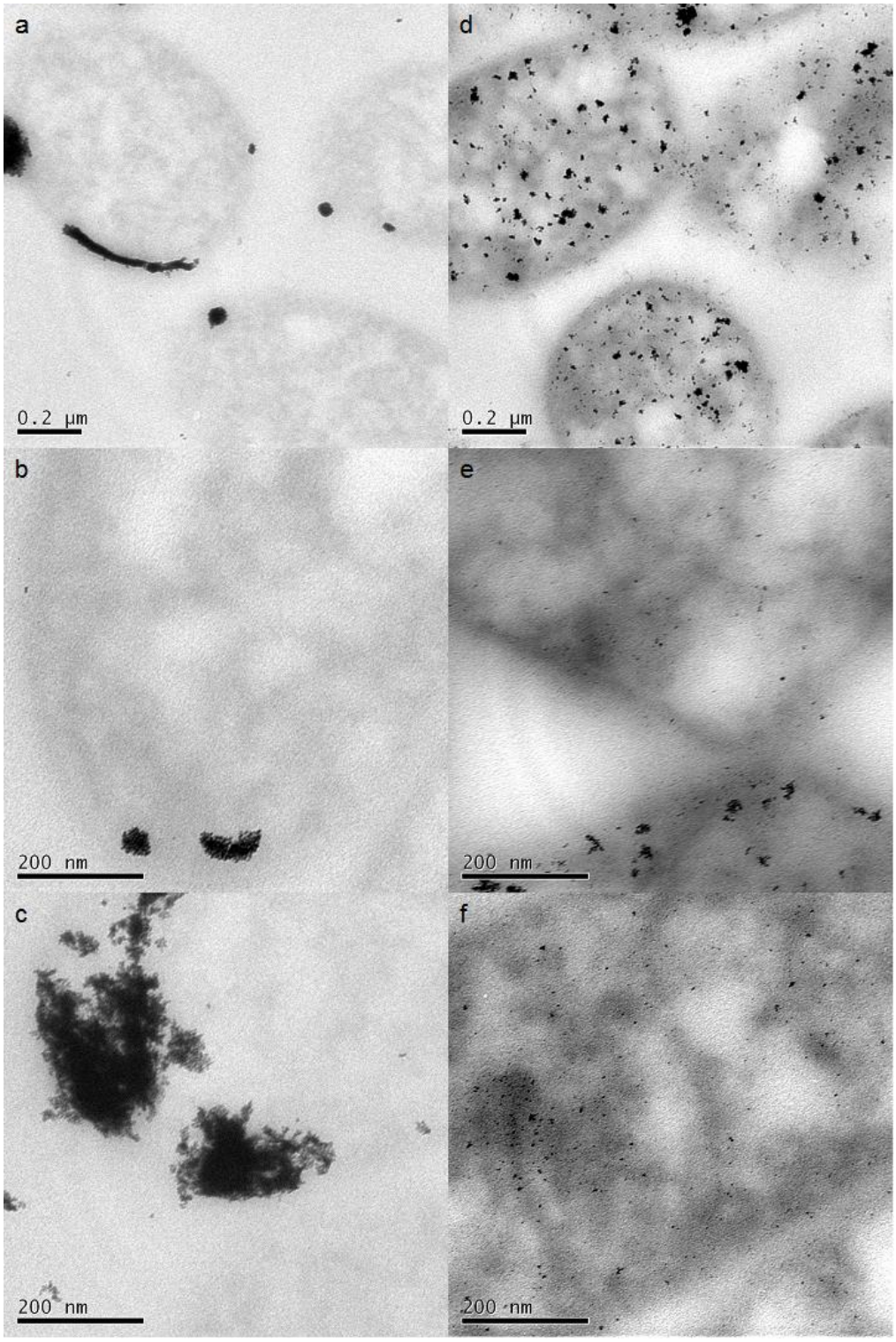

Figure 3.4, high magnification TEM images of unstained bio-platinum samples. a is sample 1, b is sample 2, c is sample 3, d is sample 4, e is sample 5 and f is sample 6 as described in Table 3.1.

The different reduction process is likely the result of the different way in which the cells process the two different electron donors. Cells readily convert the hydrogen into protons to assist with reduction, which primarily occurs in the periplasm due to the presence of hydrogenases[16,23]. Due to the low pH of the Pt salt solution, the formate will be present as formic acid, which is known to be highly toxic to cells[127]. The formic acid is split inside the cells by formate hydrogen lyase which produces molecular hydrogen and carbon dioxide[128]. This hydrogen is located within the cells, therefore allows for the reduction of Pt seed sites throughout the biomass. Furthermore, the reduction process when formate was used as electron donor required longer than it did with with hydrogen (by ~20 times, based upon the time required for colour change). Pt salt is known to cause bacterial cell walls to become permeable[7], thus it allows for Pt access throughout the cell. As formate is a slower acting reducing agent the cell wall permeabilization and subsequent Pt diffusion throughout the cell is allowed more time to proceed before reduction occurs. This would allow for the formation of nucleation sites across a greater area of the cell, which in turn will give more, and smaller, Pt nanoparticles for a given mass of Pt.

Higher magnification images of these samples are shown in Figure 3.4, which allows for the determination that there are two very distinct subpopulations with respect to particle sizes (e.g. Figure 3.4e). The cause of the irregular shape present amongst the larger nanoparticles is due to them being clusters formed of smaller particles, potentially indicating that the biological support cannot prevent agglomeration of extremely small nanoparticles within a certain distance of each other. This agglomeration was observed in all samples, which was identified due to the edges of larger metal sites possessing a grape-like structure.

Examination of the nanoparticle populations by XRD (Figure 3.5) and application of the Scherrer equation to gain information about crystallite size found that, where a clear peak could be identified, the nanoparticles average size was determined to be 5-7 nm. It is clear from the TEM images that the Pt sites are often much larger than this, confirming that the larger areas of platinum present in TEM images are clusters of smaller nanoparticles rather than single large ones.

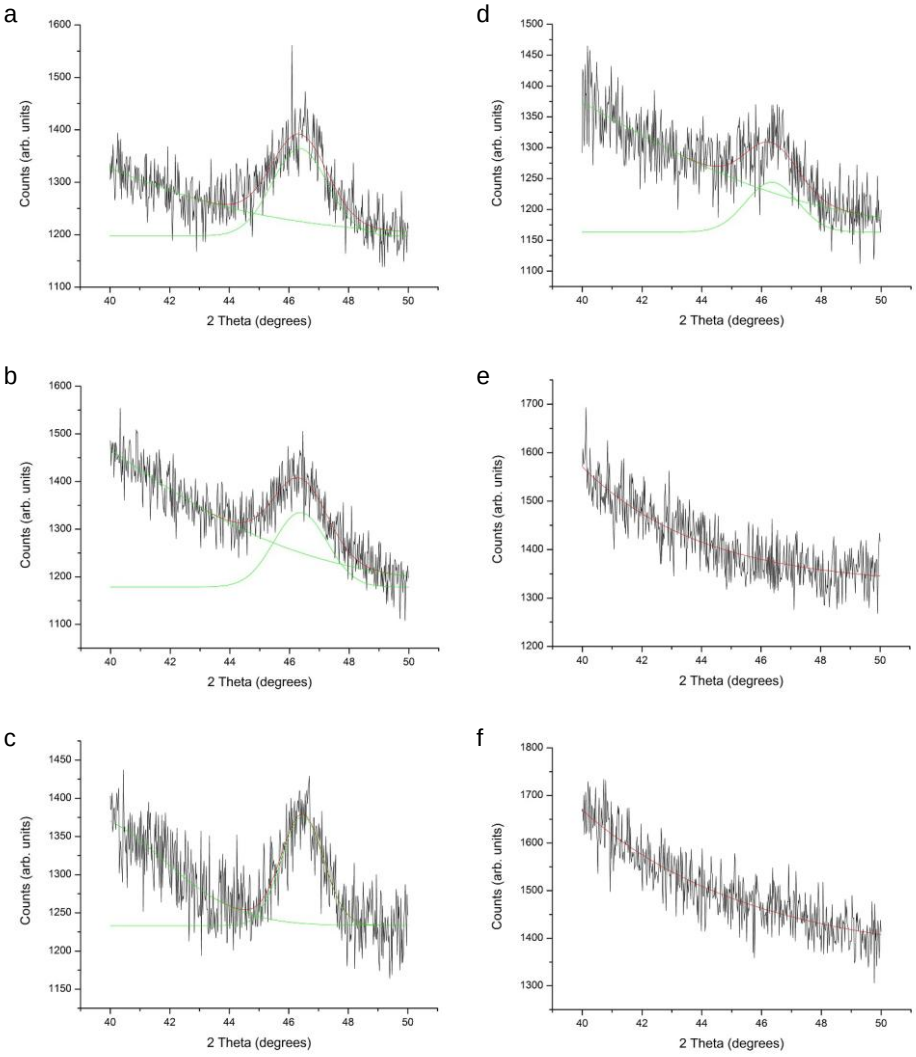

Figure 3.5, XRD data which was fitted using a Gaussian model. a is sample 1, b is sample 2, c is sample 3, d is sample 4, e is sample 5 and f is sample 6 as described in Table 3.1.

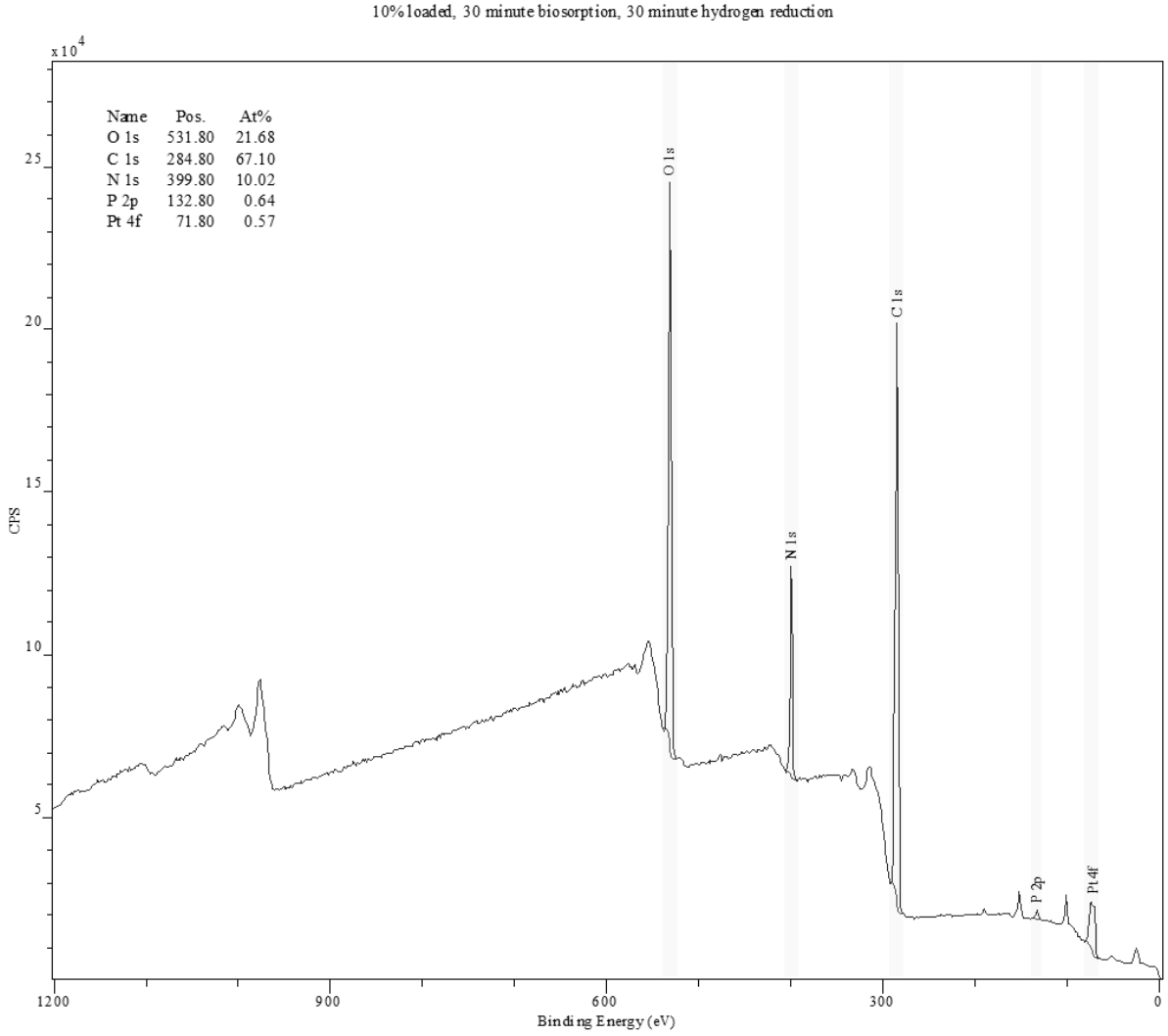

Figure 3.6, XPS survey scan of the 10 % loaded, 30 minute biosorption, 30 minute hydrogen reduction sample. Primary peaks used for quantification are indicated, other peaks are secondary peaks of the same elements, except for peaks at 100 and 149 eV binding energy which are the silicon substrate.

X-ray photoelectron spectroscopy was applied to gain information about the chemical effect upon the biomass and the degree of reduction that occurs, however as it is a surface technique it is limited to a depth of ~10 nm. Figure 3.6 is a survey scan from sample 1, full dataset is available in appendix III. The average data from the XPS survey scans (Table 3.2)

reveals that, proportionally, there are only minor differences in quantities of C and O, however the platinised samples possess a smaller quantity of N when reduced with formate and a smaller quantity of P for all platinised samples, with the hydrogen sample possessing the greater decrease, relative to the native sample. The reduced levels of N and P could be due to two factors. If these elements are being transported further inside the cell beyond the XPS measurement depth they would not be detected. Also, the N and P may be lost into the supernatant as both the bacterial stress response following exposure to acidic pH[129] and exposure to Pt ions[7] leads to increased membrane permeability, thus the cells may be unable to fully retain these elements. Phosphorus is known to play an important role in the reduction of metals by different species of bacteria[30,130], and platinum exposure is known to cause cell membrane permeabilization[7]. If the Pt(IV) were coordinating to the phospholipid bilayer and destabilizing it, this could be what allows for the Pt to then diffuse into the cell, potentially taking the P along with it.

Table 3.2, atomic percentage of elements measured by XPS survey scan. Samples are as described in Table 3.1.

	Sample 1	Sample 2	Sample 3	Sample 4	Sample 5	Sample 6	Sample 7
C	67.31	68.37	68.08	70.09	70.60	70.23	69.27
O	21.61	21.28	20.97	21.40	20.88	21.19	19.67
N	9.85	9.57	10.17	6.93	7.14	7.05	9.53
P	0.65	0.64	0.68	1.20	1.21	1.36	1.51
Pt	0.58	0.13	0.09	0.37	0.15	0.17	0.00

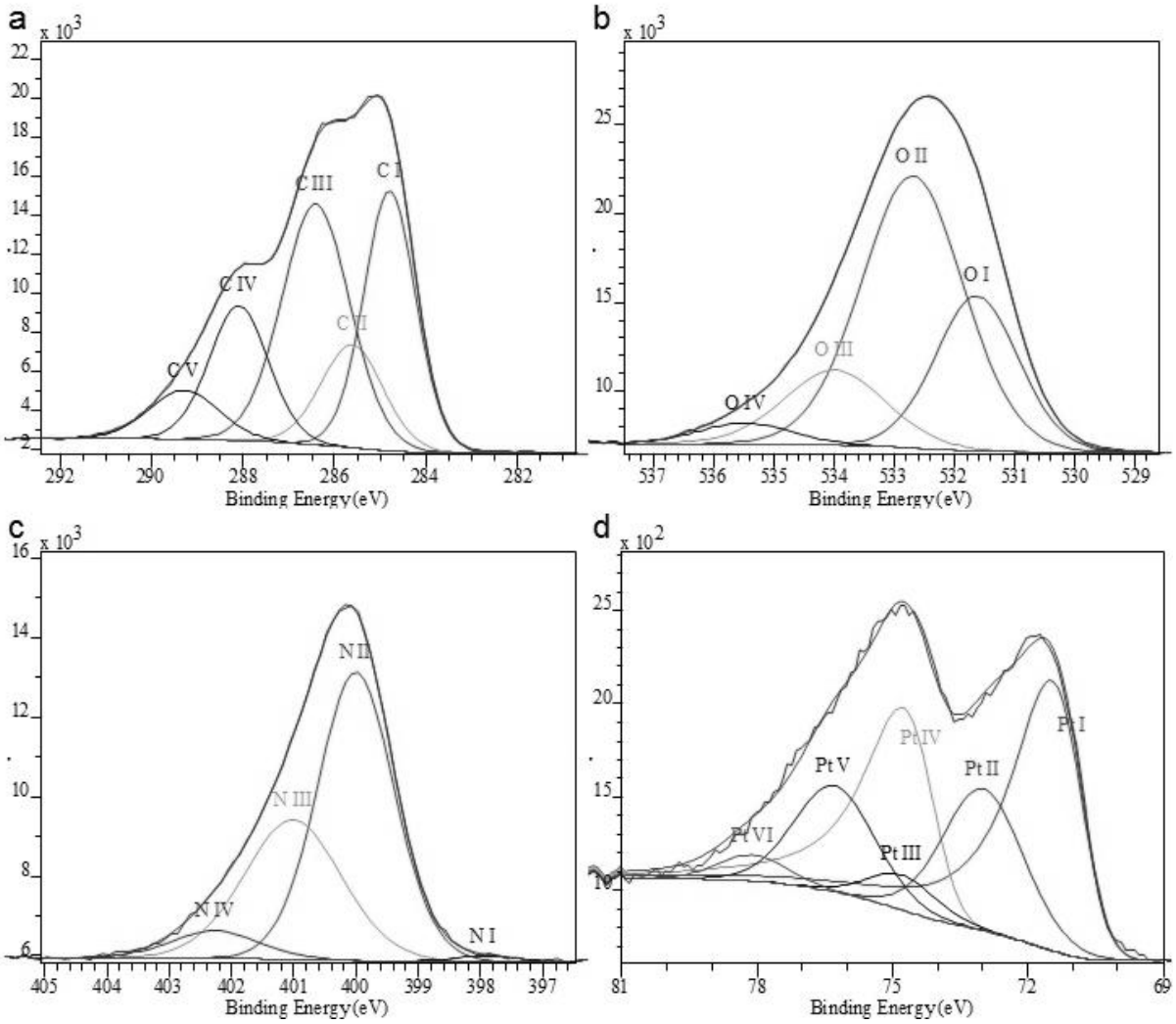

Figure 3.7, XPS high resolution scans of sample 1. a is carbon 1s, b is oxygen 1s, c is nitrogen 1s and d is Pt 4f.

The high resolution scans (Sample 1 is shown in Figure 3.7, full dataset in appendix III) show that each elemental peak consisted of a range of component peaks corresponding to different binding energies and hence different speciations of the element. The fitting of these resulted in a range of component peaks which, once identified, provide information about the interactions present and their relative proportions. The peak assignments are shown in Table 3.3.

Table 3.3, component peak binding energy (BE) and the species that the peak represents.

	C 1s		O 1s		N 1s		Pt $4f_{7/2}$	
Component	BE (eV)	Species	BE (eV)	Species	BE (eV)	Species	BE (eV)	Species
I	284.8	C-H[131]	531.4-531.6	C=O[132] or P=O[133]	397.9-398.1	Adsorbed NH[134]	70.8-71.0	Pt(0)[135]
II	285.4-285.6	C-N[131]	532.6-532.8	C-O[132] or P-O[133]	399.9-400.1	NH_2[136]	72.9-73.1	Pt(II)[137]
III	286.3-286.5	C-O[131]	533.9-534.1	H_2O[138]	400.9-401.1	N-C=O[136]	74.6-75.1	Pt(IV)[139]
IV	288.0-288.1	N-C=O[131]	535.1-535.6	Chemisorbed O[140]	402.1-402.5	NH_2^+ [141]		
V	289.1-289.4	O-C=O[131]						

The high resolution scans in the C region of the spectra are difficult to analyze due to the inevitable presence of adventitious carbon which may be present in different quantities across samples. It is further complicated by the presence of three relatively large peaks (I, II and III) in close proximity, limiting the degree of certainty for the fitting. As such the carbon 1s component peaks have been discounted from analysis. The analysis of the high resolution N, O and Pt regions of the spectra revealed the presence of additional peaks for the platinised samples relative to the native biomass (Table 3.4).

Table 3.4, peak percentage area of components of oxygen, nitrogen and platinum peaks from high resolution scans. Standard error obtained from 3 measurement sites on each sample is shown. Samples 1-3 were reduced with hydrogen, samples 4-6 were reduced with formate, sample 7 is control. The 'A' samples were loaded at 10 % Pt; 'B' and 'C' at 5 % Pt. Samples 'A' and 'B' had 30 minutes biosorption of Pt(IV); samples 'C' had 60 minute (see Table 3.1).

	1 (A)	2 (B)	3 (C)	4 (A)	5 (B)	6 (C)	7
	Area	Area	Area	Area	Area	Area	Area
O I	23.3 ±1.9	27.0 ±1.7	31.7 ±1.0	20.4 ±0.7	20.3 ±0.9	17.3 ±0.3	33.2 ±0.4
O II	57.4 ±1.3	63.1 ±1.8	61.6 ±2.3	61.9 ±0.9	61.3 ±0.9	56.9 ±2.6	59.2 ±0.4
O III	16.0 ±0.5	8.7 ±0.8	5.9 ±1.6	12.4 ±1.2	15.5 ±1.0	19.1 ±0.5	7.6 ±0.8
O IV	3.2 ±0.3	1.2 ±0.1	0.8 ±0.2	5.3 ±0.1	2.9 ±0.6	6.8 ±2.1	0.0 ±0.0
N I	0.7 ±0.1	0.1 ±0.1	0.3 ±0.1	0.4 ±0.2	0.0 ±0.0	0.2 ±0.1	0.0 ±0.0
N II	61.5 ±2.5	62.3 ±3.2	70.6 ±3.3	55.2 ±2.6	61.9 ±3.3	50.0 ±1.5	71.3 ±3.3
N III	31.8 ±2.5	31.4 ±3.0	26.4 ±2.7	31.5 ±2.2	30.0 ±3.4	31.4 ±4.1	28.7 ±3.3
N IV	6.1 ±0.1	6.1 ±0.4	2.7 ±1.0	12.9 ±2.0	8.1 ±0.2	18.5 ±4.5	0.0 ±0.0
Pt I	59.8 ±0.8	30.9 ±1.0	13.2 ±1.1	43.8 ±1.8	24.5 ±0.3	27.1 ±3.4	NA
Pt II	31.8 ±1.0	61.7 ±0.7	79.3 ±3.5	47.4 ±0.7	70.0 ±0.5	60.3 ±1.5	NA
Pt III	8.3 ±0.7	7.4 ±1.6	7.5 ±2.6	8.8 ±1.1	5.5 ±0.7	12.6 ±2.1	NA

In the case of the O region of the spectra, the extra peak (O IV) present in the platinised samples is produced by O adsorbed onto the Pt surface. There is also a decrease in quantity of the O I peak (doubly bonded O), but no change, within experimental error, in the O II peak (singly bonded O). The O III peak (H_2O) shows great variation between samples, but also possessed a large discrepancy between different sites of each sample. This suggests that either some of the double bonded oxygen species are providing electrons for the Pt reduction or are being cleaved during the biosorption process. Such cleaving could account for the destabilisation of the membrane if it is P=O bonds within the phospholipids that are being broken. However, it is unclear whether all such instances are reduced and then the oxygen is chemisorbed onto the resulting Pt(0), or if some are becoming singly bonded due to the variability in H_2O present.

In the N region there are two additional peaks, N I and IV which result from NH adsorbed onto the metal surface and NH_2^+ respectively. The N I peak is only present in very small quantity, and not present in all platinised samples. There is a trend showing the preferential adsorption of NH with hydrogen reduced samples, as more is present in each of these than in the equivalent formate reduced sample. This quantity increases when a larger proportion of platinum is present, which is unsurprising due to the increased quantity of potential adsorption sites. It also increases when the biosorption duration is increased, which suggests that this originates during the biosorption step. This may represent the amine groups present in the enzymes that provide the biosorption sites for the initial formation of Pt seeds. If this is the case, it could be expected that a greater quantity would be found in the formate samples due to the presence of a greater number of Pt sites present in these, as

observed by TEM (Figure 3.3), however many of these sites are located deeply within the biomass and beyond the detection range of XPS, whereas the H_2 reduced samples possess Pt predominantly at the surface of the biomass which could thus be better detected.

The N IV peak indicates the presence of NH_2^+, which would occur due to amine groups providing electrons to assist in the reduction of Pt, such endogenous reduction has been previously observed in *Desulfovibrio desulfuricans*[25]. This peak is greater in the formate samples which also tend to possess a smaller proportion of Pt(0) than the hydrogen samples. As the formate reduced samples possess a more limited supply of reducing agent, it is possible that the biomass is required to provide additional reduction capability in this case, when compared to the hydrogen reduced samples, due to either the slower mechanism or an inability for complete utilisation of the provided electron donor. As the N III peak (amide) is unchanged, within experimental error, between all samples and the N II peak (amine) is much smaller in the platinised samples compared to the native biomass, it is the amine groups rather than the amide groups which assist in reduction. The exception to this trend is sample 3 which does not show a significant decrease in amine presence, however it also possesses very little of the oxidised nitrogen group. This sample also possessed a large variation between analysis sites on the sample, which is likely the result of the preferential Pt reduction at a limited number of sites as shown in Figure 3.3c.

For Pt peaks it is important to note that the use of an asymmetric lineshape results in the occurrence of a greater degree of uncertainty when comparing relative peak areas[142]. The difference between Pt measurements shows that sample 1 possesses the greatest proportion of Pt(0) across all samples. This is unexpected as it possesses a lower quantity of

hydrogen per Pt atom than the 5 % loaded equivalent; however, as the 10 % loaded formate sample also undergoes a more complete reduction than the 5 % loaded equivalent, where both had proportionally equal Pt to reducing agent, it is likely that this is the result of particle size. Figure 3.3 shows that a 10 % loading results in larger particle size than a 5 % loading, which results in a lower proportion of surface Pt thus a lower proportion interacting with O or N groups.

The 60 minute biosorbed samples possess a greater degree of variation between sample sites, indicated by their error being proportionally larger for the Pt or Pt related peaks (O IV (chemisorbed O), N I (adsorbed anime) and N IV (oxidised amine)) when compared to other samples. The increased biosorption duration could be causing this due to an increase in the development of certain Pt seed sites leading to increased autocatalytic reduction in these locations and thus an imbalance in the distribution of Pt throughout the biomass.

The differences observed in the XPS data shows that the use of formate or hydrogen as reducing agent leads to the participation of different chemical groups, which is likely the result of the interaction with different binding sites. As hydrogenases have been shown to play an important role in the bioreduction of precious metals it is likely that other enzymes, possibly including formate hydrogen lyase, fill that role when formate is used as reducing agent, which would lead to these differences arising. It is unclear if there are particular aspects of the biomass which are serving a similar role in the formate based reduction, as is the case with hydrogen based reduction (e.g. formate dehydrogenases), or if the platinum toxicity is leading to the thorough permeation of Pt throughout the biomass which then biosorbs onto non-specialized sites to be eventually reduced.

3.4 Conclusion

In summary, it has been shown that the shift in colour from the appearance of native biomass towards that of the biosorbed metal gives an indication of the distribution of the metal particles formed, provided that all metal precursor has been removed from solution. The differences in reduction conditions used for this study have each shown a different impact upon the resulting bio-Pt. Increased metal loading has been shown to result in both an increase in cluster size and quantity of nanoparticles sites. Biosorption duration appears primarily to influence the degree to which preferential reduction occurs at some sites, yet does not appear to have any impact upon the surrounding biochemistry for the samples in this study. The choice of reducing agent has the greatest impact upon the resulting nanoparticle location and cluster size, although very little impact upon the individual particle size. It also affects the aspects of the biomass which interact with the platinum, with a hydrogen reduction favouring phosphate groups, whereas a formate reduction favours amines.

3.5 Acknowledgements

The authors would like to thank Dr. Anders Barlow at the National EPSRC XPS Users' Service (NEXUS) for the XPS data collected, and Mrs. Theresa Morris at the University of Birmingham Centre for Electron Microscopy for her assistance with the electron microscopes used during this study.

4. DEVELOPING AND TESTING OF ANALYTICAL SYSTEM

Electrochemistry covers reactions where there is a transfer of electrons to or from a reagent. When electrochemical reactions are carried out it is necessary to understand key electrode processes. The Nernst equation describes the interaction between the equilibrium potential and the activity of the reagents for a particular reaction; thus is important when an electrode potential is used to control the relative concentration of the reduced and oxidised species. There is also an activation barrier which must also be overcome, which affects the rate of reaction, as described by the Arrhenius equation. A derivative of the Arrhenius equation leads to the Butler-Volmer and Tafel equations which provide information such as the exchange current density, a property that gives an indication as to the effectiveness of an electrocatalyst. It is also important to consider the effect of transport phenomena as the current produced in an electrochemical reaction is proportional to the quantity of reactants available per second, as described by the Koutecký-Levich equation. In addition to a good understanding of the theory behind an area of science, an experimentalist needs to ensure that the apparatus used for such work is appropriately set up and functioning properly. This chapter describes a test experiment conducted using a ferri-/ferro-cyanide model system.

4.1 Electrochemical Theory

4.1.1 Fundamentals

The charge transfer processes taking place in an electrochemical cell can be represented in a basic form by the oxidised species, *O*, receiving *n* electrons to become the reduced species, *R*, as shown by Equation 4.1.

$$O + ne^- \leftrightarrow R \tag{4.1}$$

The electrons are provided by the electrode; however they are required to be of appropriate energy for the reduction or oxidation to occur. In order for electron donation to occur, the Fermi level of the electrode must be greater than the receptor orbital in the oxidised species. Likewise; for electron reception to occur, the Fermi level of the electrode must be lower than the donor orbital of the reduced species. The Fermi level of the electrode can be adjusted by altering the electrode potential. Over time the concentration of the oxidised and reduced species will arrive at equilibrium, the value of which is dependent upon the electrode potential. This relationship is described by the Nernst equation (Equation 4.2) which relates the equilibrium potential, E_{eq}, to the standard potential of the reaction, E^O, the ideal gas constant, R, the temperature, T, the number of moles of e^- being transferred, n, the Faraday constant, F, and the activity of the oxidised and reduced species, a_O and a_R.

$$E_{eq} = E^o + \frac{RT}{nF} ln \frac{a_O}{a_R} \tag{4.2}$$

It is typically more convenient to use a modified form where the formal potential, $E^{o'}$, is used instead (Equations 4.3 and 4.4) as this allows the use of concentration of oxidised, C_O, and reduced, C_R, species at the electrode, rather than their activities. The formal potential is related to the standard potential, but modified by the activity coefficients of the oxidised, γ_O, and reduced species, γ_R.

$$E_{eq} = E^{o'} + \frac{RT}{nF} ln \frac{C_O(x = 0)}{C_R(x = 0)} \quad (4.3)$$

$$E^{o'} = E^{o} + \frac{RT}{nF} ln \frac{\gamma_O}{\gamma_R} \quad (4.4)$$

The activity coefficient provides a proportional relationship between the activity and the concentration of the reactant, thus at low concentration where the activity coefficient ≈ 1 the formal potential and the standard potential are approximately equal.

As the standard potential and the number of moles of electrons transferred are dependent upon the species involved and the temperature may be controlled, it is possible to obtain a situation where the relative concentration of the reduced species is controlled by the applied potential.

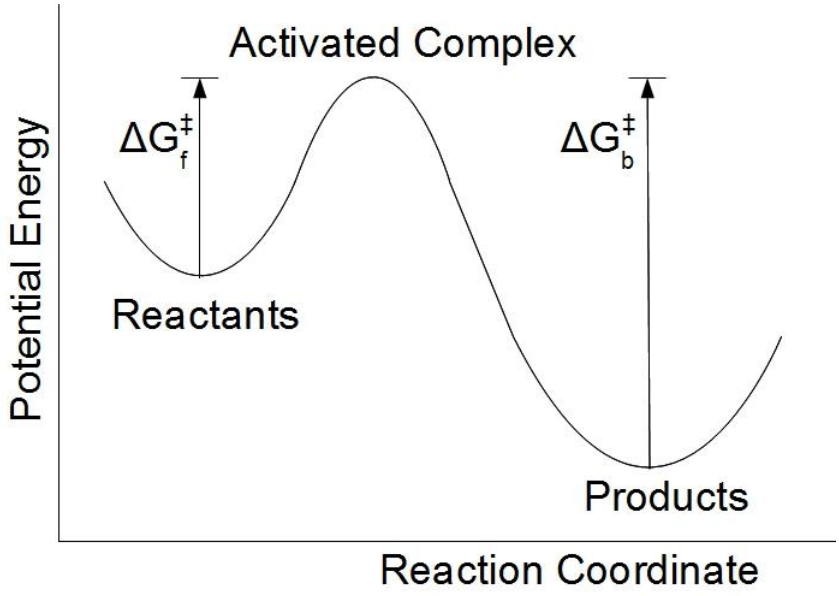

Figure 4.1, shows the potential energy of the reaction components, where $\Delta G_f^{\ddagger}$ and $\Delta G_b^{\ddagger}$ are the free energy requirement for the forward or backward reaction to achieve the activated complex state. Adapted from Bard and Faulkner (2001)[143].

Chemical reactions possess an activation barrier, an amount of energy that must be overcome for the reaction to proceed. The energy requirement for this is shown diagrammatically in Figure 4.1. The activated complex is an intermediate state which is energetically unstable, but is a necessary intermediate step in the reaction; either forwards or backwards. An input of free energy is required to obtain that state, which is short lived as it will rapidly decay in one of the two directions. For the reaction shown in Figure 4.1 the rate at which reactants are converted into products will be much more rapid than the reverse as the free energy requirement to obtain the activated complex is much easier to provide. This provides a kinetic limitation to the rate of reaction.

The rate constant, k, has an exponential relationship to the free energy, as described by the Arrhenius equation (Equation 4.5) where A is the pre-exponential factor, E_A is the activation energy, R is the gas constant and T is temperature. Typically we can provide additional energy to the system by providing heat, which will assist the reactants or the products to obtain the necessary energy to achieve the activated complex.

$$k = Ae^{-(E_A/RT)} \tag{4.5}$$

For an electrochemical system there is an additional method of affecting the energy requirement; altering the electrode potential alters the system and changes the values of $\Delta G_f^{\ddagger}$ and $\Delta G_b^{\ddagger}$. For a reduction reaction, the relationship between these factors has the form shown in Equations 4.6 and 4.7 (the Butler-Volmer equations), where k_f is the forward reaction rate constant, k_b is the backwards reaction rate constant, k^0 is the rate coefficient at $E = E_{eq}$ and α is the transfer coefficient.

$$k_f = k_f^o e^{-\alpha nF(E-E^o)/RT} \tag{4.6}$$

$$k_b = k_b^o e^{-(1-\alpha)nF(E-E^o)/RT} \tag{4.7}$$

To identify the rate at which the reaction rate is occurring in an experiment we can monitor the current. As the electrode reaction occurs it either provides or accepts electrons. This results in a flow of charge. The amount of charge which flows per unit time is detectable as

current. Provided that the number of electrons being transferred in the reaction of interest is known then current may be used to directly monitor the rate of reaction.

$$v = i/nFA \tag{4.8}$$

where v is the electron flux or net rate of electrode reaction, i is the current passed, F is Faraday's constant and A is the electrode area.

As is shown in Equation 4.1, a reaction does not simply progress in one direction. As a result, Equation 4.8 is the sum of Equations 4.9 and 4.10.

$$v_f = k_f C_O = i_c/nFA \tag{4.9}$$

$$v_b = k_b C_R = i_a/nFA \tag{4.10}$$

where i_c is the cathodic current and i_a is the anodic current.

In a situation where a reaction is being studied electrochemically it is possible to obtain information from the electrode potential. The electrode potential controls the energy of the electrons present at its surface. If the electron energy, or Fermi energy, of the electrons at the electrode and the Fermi energy of the available electrons in the reactants are equal, no change will occur. If the Fermi energies of these electrons are not equal, equality is attained via the transferral of electrons from the higher Fermi energy to the lower one. When equilibrium has been achieved, v_f is equal to v_b. The net current in this case is zero as the detected current density is the sum of the forward and backward current densities. We can denote a quantity, i_0, known as the exchange current. This is what the current at equilibrium in one direction would be if we were able to measure it. The magnitude of i_0 gives a very

good guide to the rate of reaction; the difficult part is obtaining this value. Through the combination of Equations 4.6, 4.7, 4.9 and 4.10 it is possible to obtain Equation 4.11, which is typically simplified to Equation 4.12, and is known as the Butler-Volmer equation and provides information about the exchange current.

$$i = nFAk^o \left(C_O \exp\left[\frac{\alpha nF}{RT}(E - E^o\right] - C_R \exp\left[\frac{(1-\alpha)nF}{RT}(E - E^o\right]\right) \quad (4.11)$$

$$j = j_0(e^{\alpha nf\eta} - e^{-(1-\alpha)nf\eta}) \quad (4.12)$$

where j is the current density, j_0 is the exchange current density, f is equal to F/RT, η is equal to $E-E^o$.

Equation 4.12 consists of a forward (reduction) portion and a backward (oxidation) portion. Both of these are dependent upon η, although the dependence of one is the inverse of the dependence of the other. This means that if the overpotential is very positive the backwards term dominates, and if it is very negative the forwards term dominates. In these conditions it is possible to make the approximation that the smaller term vanishes. If we then take logarithms of these two new approximate equations we arrive at the Tafel equation (Equation 4.13).

$$\eta = a + b \log(i) \quad (4.13)$$

$$a = \frac{2.3}{\alpha nf} \log(i_0) \quad (4.14)$$

$$b = \frac{-2.3}{\alpha nf} \quad (4.15)$$

With a Tafel plot, η vs. log(i), it is possible to extract information from both the intercept (Equation 4.14) and the slope (Equation 4.15) of that plot. At standard temperature and pressure and applying the assumption that $\alpha \approx 0.5$, the slope is equal to n/120 mV/decade where n is the number of electrons transferred in the rate determining step. The intercept provides information about i_0, however it is necessary to extrapolate the plot to obtain this as the Tafel equation does not apply at low overpotential where the anodic and cathodic currents are both non-negligible.

The rate of a reaction is not solely dictated by the kinetics of that reaction. In the situation where the rate of a reaction is high, and the reverse rate is not, it will reach a situation where there is not sufficient reactant to maintain that rate. For an electrochemical reaction this becomes present at high overpotential as this leads to a rapid, one-sided, reaction. In this case the reactant present at the electrode will be rapidly converted into product, and then the reaction will be limited by the rate at which the reactant reaches the electrode.

4.1.2 Transport Phenomena

There are three types of transport phenomena which are relevant to electrochemistry; diffusion, convection and migration. Diffusion is the transport of a species along a concentration gradient. The direction of diffusion is from a region of high concentration to a region of low concentration, as described by Fick's first law. Convection comes in two forms, natural and forced. Natural convection occurs as a result of thermal or density differences between areas of the solution. Forced convection occurs as a result of the provision of heat

or mechanical interference, although heat is rarely used for this purpose as thermal convection is much more random than the use of stirring. Migration is the movement of charged particles in an electrostatic field, the act of charged particles redistributing themselves in a field to obtain overall neutrality.

It is possible to manipulate conditions such that the impacts of certain transport effects are limited. The affect that migration has on the reaction components can be made to be negligible by the use of a sufficiently concentrated electrolyte solution. As the electrostatic charge can be carried by any ions a sufficient excess of electrolyte will allow for migration effects to be ignored. To ensure that this is the case a concentration of 0.1 M or greater is typically used. A large excess of inert electrolyte also has additional advantages. The solution is more conductive, thus there is less resistance to hinder the current and it is, effectively, of constant ionic strength, thus the activity of reactants and products does not change throughout. Also it compresses the double layer to increase the efficiency of electron transfer.

Natural convection effects are negligible over short time scales, but there are ways in which they can be further limited. The usage of a heat bath means that the solution is maintained at constant temperature and thus there will be negligible convection resulting from temperature gradients. Density differences between reactants and products are more difficult to control. One method which can be used to control natural convection effects is to apply forced convection. If this is done correctly, all natural convection becomes negligible. Although natural convection is typically of lesser magnitude than forced convection, it is of

an unknown degree. In certain circumstances it is preferable to have a known and controllable large effect rather than a random minor effect.

4.1.2.1 Diffusion

In an isolated system, Fick's first and second laws describe the diffusion process. The first law (Equation 4.16) shows how a species behaves within a one dimensional concentration gradient such that the gradient will ultimately be annulled. This is represented by an equation where J_O (x, t) is the flux of species O at position x and time t, $\partial C_O/\partial x$ is the concentration gradient of O in direction x and D_O is the diffusion coefficient of O. The negative sign shows that the species move from a high concentration to a low one.

$$J_O(x,t) = -D_O \frac{\partial C_O(x,t)}{\partial x} \tag{4.16}$$

In the case of an electrochemical cell at high overpotential there is the conversion of reactant to product. This leads to an increase in the product concentration at the electrode surface compared to the rest of the solution. There is also a deficiency of reactant at the electrode surface compared to the rest of the solution. As a result of this the product will diffuse away, trying to attain an equal concentration throughout the whole solution. The reactant will diffuse in towards the electrode for the same reason. This process is not completed instantaneously thus we have an expanding region of reactant depletion and product excess as time progresses.

Fick's second law (Equation 4.17) describes the rate at which C_O, the concentration of species O, alters over time.

$$\frac{\partial C_O(x,t)}{\partial t} = D_O \frac{\partial^2 C_O(x,t)}{\partial x^2} \tag{4.17}$$

4.1.2.2 Forced Convection

If the working electrode is rotated, convection of material towards it will occur, and the rate of this convection increases as the rate of rotation increases (Figure 4.2). Under the circumstance where the overpotential is high, the reaction rate will be limited by the rate at which the reactants are transported to the electrode. For an electrochemical reaction the current is proportional to the reaction rate (Equation 4.8), thus for the above situation, the current will increase as the rotation rate is increased. This situation is thoroughly described by the Levich equation (Equation 4.18).

$$i_l = 0.62nFAD_O^{2/3}\omega^{1/2}\nu^{-1/6}C_O^* \tag{4.18}$$

where i_l is the Levich, or diffusion limited, current, n is the number of electrons transferred, ω is the rotation rate in $rads^{-1}$, v is the kinematic viscosity of the solution and C_O^* is the bulk concentration of species O.

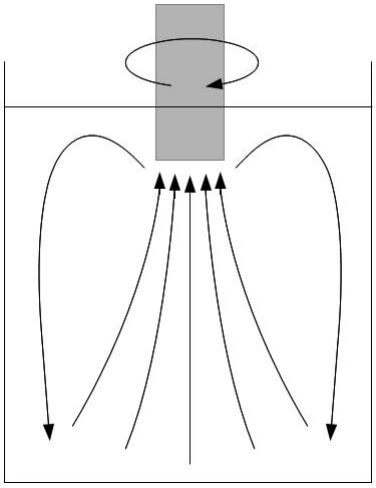

Figure 4.2, example diagram of fluid flow during forced convection.

A Levich plot, i vs. $\omega^{1/2}$ (Figure 4.3a), will be linear provided that the overpotential is great enough to ensure that the mass transport is the current limiting factor. If this is extended, the kinetics will inevitably become the limiting factor and the plot will be curved such that i = i_k as $\omega^{1/2} \rightarrow \infty$. However, this is not an effective way to obtain information about i_k, as the necessary rotation rate required would be difficult to obtain. Yet the total current is related to both the kinetic current and diffusion limited current, as shown in Equation 4.19.

$$\frac{1}{i} = \frac{1}{i_k} + \frac{1}{i_l} \tag{4.19}$$

The combination of Equations 4.18 and 4.19 leads to the Koutecký-Levich equation (Equation 4.20), from this it can be observed that a plot of i^{-1} vs. $\omega^{-1/2}$ (Figure 4.3b) would yield a graph where the slope was related to n, A, D_O, v and C_O^*, and the intercept would equal i_k^{-1}. This is known as a Koutecký-Levich plot, which provides information about the kinetic

current from the intercept. It also allows for determination of one of the terms in the Levich equation from the slope, provided all the other terms are known.

$$\frac{1}{i} = \frac{1}{i_k} + \frac{1}{0.62nFAD_O^{2/3}\omega^{1/2}\nu^{-1/6}C_O^*} \tag{4.20}$$

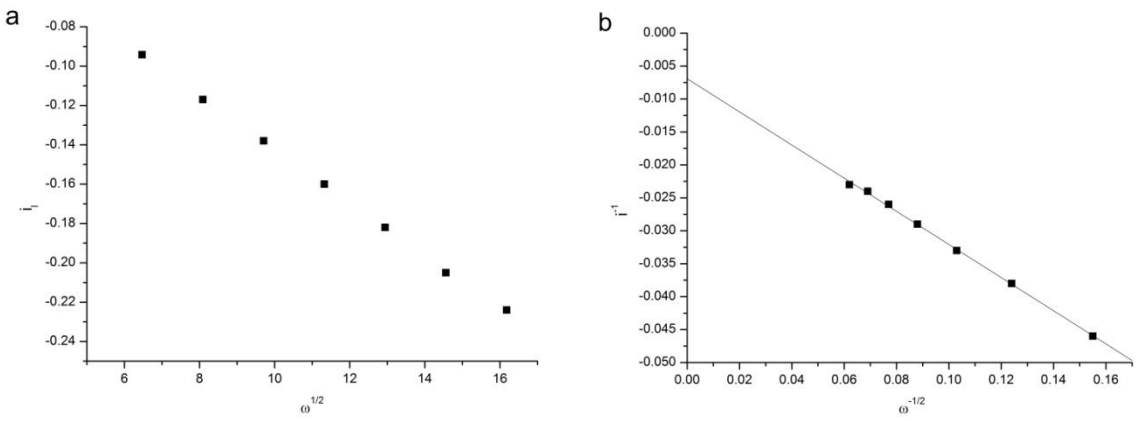

Figure 4.3, example Levich (a) and Koutecký-Levich (b) plots.

4.1.3 Electrochemical Surface Area (ECSA)

When a reaction is being catalysed by an expensive material, it is important to obtain the maximum possible effect for as little material as possible. As a catalyst affects a reaction through surface interaction, one possible method of enhancing the efficiency is to use a material with a high surface area, thus small particles. However, the physical surface area is not the truly effective quality, the electrochemically active surface area needs to be maximised. These two properties are related as increasing the physical surface area typically increases the electrochemical surface area.

The measurement of the electrochemical surface can be achieved through different methods, which ultimately involve the adsorption and subsequent removal of a substance from the catalyst surface. The removal of the substance from the catalyst is achieved by altering the potential of the electrode. This is a gradual process which becomes increasingly likely to occur the further the potential is altered, until the point where the reaction balance has been shifted sufficiently that the rate of the adsorption of substance to the catalyst is negligible. Throughout this procedure electrons will flow between the electrode and the substance adsorbed onto the catalyst, thus a current can be measured. Given that current is charge per unit time (Equation 4.21) it is possible to calculate the total charge that passes between the electrode and the adsorbed substance, if the voltage is changed by a set amount per unit time it is possible to determine the time from the change in potential.

$$q = \int i \, dt \tag{4.21}$$

4.2 Electrochemical Setup

Electrochemical measurements were carried out at 298 K, controlled using a heated water bath and a peristaltic pump feeding water into a jacket on the electrochemical cell. The bath temperature was controlled using a submerged heater and monitored by thermometer. The electrochemical vessel was routinely cleaned using a mixture of concentrated nitric and sulphuric acids. Measurements were made using a 3 electrode arrangement, with the working electrode being a 2 mm diameter Pt or 3 mm diameter glassy carbon (GC) disc electrode, the counter electrode being Pt mesh and the reference a leakless Ag/AgCl

reference electrode (eDaq), arranged as shown in Figure 4.4. Prior to first use all working electrodes were polished on wet sandpaper, then with alumina slurry of gradually decreasing particle size; subsequently only alumina slurry was utilised for cleaning prior to each use. The counter electrode was flame-annealed prior to each use. Experimental control was via an Autolab PGSTAT302N potentiostat operated using Nova 1.10 (Metrohm). The electrochemical cell and all electrodes were housed inside a faraday cage, which was earthed to prevent electrical interference. The water heater was also earthed.

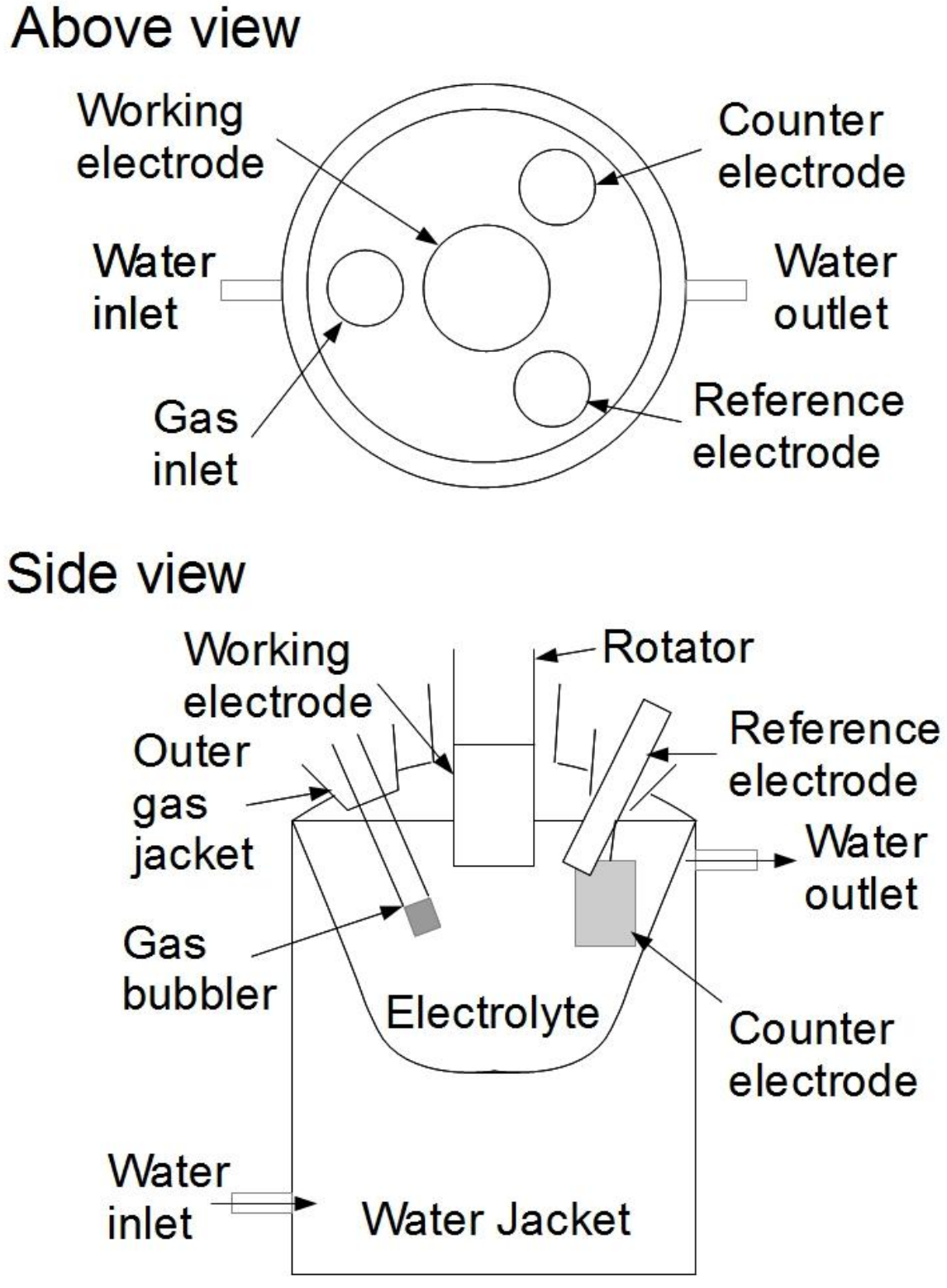

Figure 4.4, electrochemical apparatus arrangement.

4.3 Equipment testing

Prior to full investigation of bio-Pd samples, electrochemical measurements were conducted using the ferri-/ferro-cyanide system in a dioxygen free electrolyte[144]. The sample solution consisted of 1 M KNO_3 and 5 mM $K_3Fe(CN)_6$. Experiments were done at scan rates of 25, 50 and 100 mV/s. The purpose of these tests was to ensure that the electrochemical equipment was performing accurately. This could be determined with this system as it is a well defined reversible system. The peak current is determined by the Randles-Sèvčík equation (Equation 4.22).

$$i_p = 0.4463nFAC\left(\frac{nF\nu D}{RT}\right)^{\frac{1}{2}} \quad (4.22)$$

where i_p is the peak current, n is the number of electrons transferred, F is the Faraday constant, A is the area of the electrode, C is the concentration, v is the potential scan rate, D is the diffusion coefficient, R is the gas constant and T is the temperature.

The effect of the scan rate can be seen in Figure 4.5. As expected from the Randles-Sèvčík equation the increase of scan rate results increased peak current. The anodic and cathodic peak currents are predicted to be equal, which is the case when baselines are applied. These are in close agreement with the value expected[145]. The peak potential can be observed to remain constant, indicating that the reaction occurring is reversible with rapid kinetics. When GC electrodes were used a small increase in peak separation could be observed, indicating that the kinetics were slower.

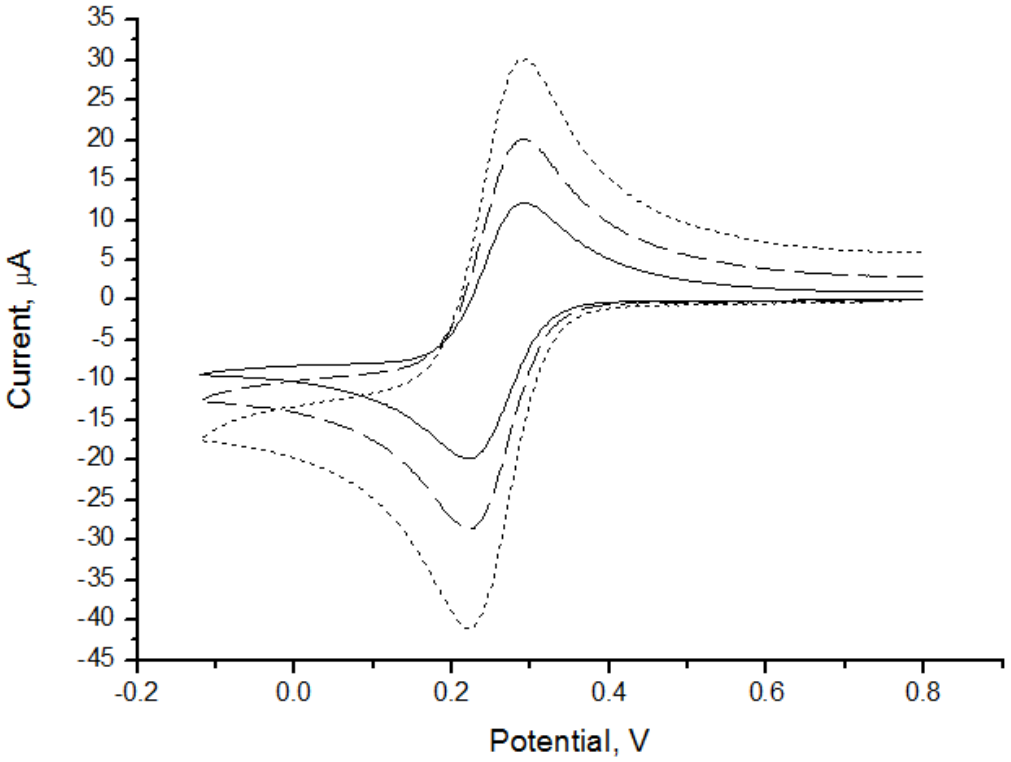

Figure 4.5, typical cyclic voltammogram of the 5 mM ferri-/ferro-cyanide system with a 2 mm diameter Pt electrode at scan rates of 25 (solid line), 50 (dashed line) and 100 mV/s (dotted line).

The ferri-/ferro-cyanide experiment was repeated with each electrode until all were performing appropriately, i.e. the peak to peak separation is roughly 60 mV (Figure 4.6). During this process each electrode not performing as expected was subjected to thorough polishing to obtain a good, contamination-free, surface. Initially the reference electrode potential was found to drift, which subsequently settled, yet its potential was routinely tested to ensure that no further change in potential occurred. Three 3 mm diameter GC disc working electrodes were used (Figure 4.6), all of which were found to be in close agreement

with the Randles-Sèvčík equation (Equation 4.22) as the peak current was within close approximation of that predicted by theory.

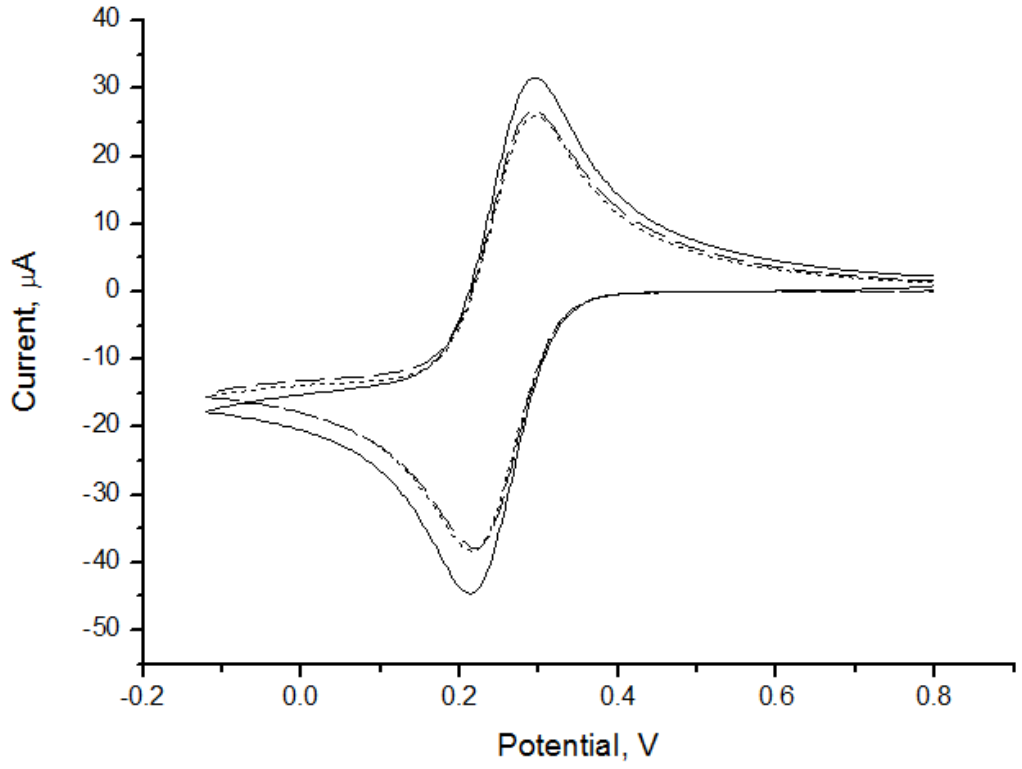

Figure 4.6, cyclic voltammograms of the 5 mM ferri-/ferro-cyanide system with 3 different 3 mm diameter glassy carbon electrodes at a scan rate of 25 mV/s. Electrode 1 (solid line), electrode 2 (dashed line) and electrode 3 (dotted line).

4.4 Acknowledgements

The contents of chapter 4 are based heavily upon Bard and Faulkner (2001)[143] and lecture notes prepared and kindly provided by Dr. Sarah Horswell.

5. DEVELOPMENT AND EVALUATION OF METHODS TO PRODUCE ELECTROCATALYSTS FROM BIO-PT USING *ESCHERICHIA COLI* AND *DESULFOVIBRIO DESULFURICANS*

Bioreduction of platinum is a promising alternative preparation procedure of Pt-nanoparticles for catalytic use. For use in a fuel cell the presence of a large quantity of non-conductive biomass is a severe hindrance which needs to be addressed before fuel cell application. This study investigates 'bio-Pt' prepared using two different species of bacteria and a selection of potential methods to remove the undesirable biomass subsequent to the completion of the bioreduction process. The resulting 'cleaned' nanoparticles were then tested in an electrochemical cell using cyclic voltammetry and linear sweep voltammetry to provide information about the electrochemically active surface area and diffusion limited current. Transmission electron microscopy was used to provide supporting information about the degree of cleaning achieved, showing that the most electrochemically active catalysts were those with minimal remaining biomass. X-ray diffraction was used to show the degree of particle size growth occurring as a result of the partial removal of the supporting biomass. Samples where the diffusion limited current was within 10% of theoretically predicted values were further investigated in comparison with commercially prepared catalyst (Tanaka Kikinzoku Kogyo). Information about mass and specific activities, and half-wave potential showed that one of the 'bio-Pt' preparations compared favourably to the commercial catalyst.

5.1 Introduction

Polymer Electrolyte Fuel Cells (PEFCs) are efficient energy production devices that have potential uses in many applications, including automotive[146-148] and domestic power generation[149,150], due to their low temperature operation and rapid start up[151,152]. However, several major drawbacks preclude widespread commercial application, such as their high cost and poor durability. One of the main areas of development for PEFCs is the catalyst, which typically consists of platinum or platinum alloy nanoparticles supported on carbon and this accounts for over 20 % of the total cost of the fuel cell system[148]. Pt and Pd catalysts are susceptible to poisoning, e.g. by trace amounts of impurities present in commercial hydrogen feedstock gas, as well as contributing to the premature failure of the FC electrode, the need to extensively purify hydrogen adds to the overall cost.

In an attempt to address these issues, microbiology has been applied in two ways. As an alternative to petrochemically-derived hydrogen, H_2 can be produced as a fermentation product of sufficient purity to feed a PEFC directly[153,154]. In addition, biohydrogen-producing bacteria can be used subsequently to manufacture platinum group nanoparticles which are active as fuel cell electrocatalysts[34]. Precious metal ions (Pt(IV) and Pd(II)) can be reduced using hydrogenases to make nanoparticles of Pt(0) and Pd(0)[16,23,155]. Hence, the bioreduction of metals from solution is capable of producing effective catalysts through a bottom up scheme of preparation[8,33]. There is also evidence supporting the usage of Pt and Pd from waste sources, such as road dust to make nanoparticle catalyst[156]; bio-catalyst made from waste supported energy production in a PEFC[32]. Another potential benefit of such a production method is that bacteria are grown at large scale in many industrial processes;

residual biomass must be disposed of, at cost. If these wastes from primary production could be reused to produce platinum nanoparticles for PEFCs, costs could be reduced significantly[34]. This production method also has the benefit that there is no need for the use of environmentally harmful solvents as well as harnessing a waste from one application (motor vehicle catalytic converters) into a device for clean energy production. Ultimately this approach brings dual benefits in terms of low carbon technology; 'closed loop' metal recycling would reduce the impact of sourcing and refining from primary sources. The environmental 'cost' is 2-75 tonnes of CO_2 per kg of Pt mined from primary reserves[157]. Bio-recycling is 'clean' in that, once soluble forms of metals are obtained, metal recovery and catalyst fabrication are performed in a single step at ambient temperature with recovery of the catalyst under gravity.

However, for application in fuel cells it is necessary for a good electrical contact to the catalyst. An initial study showed that native metallized biomass of *E.coli* had little activity in a PEFC, attributed to the high water content conferring low conductivity[155]. Sintered biomass of platinised cells of *Desulfovibrio desulfuricans* gave power output comparable to commercial FC electrode catalyst[155]. *Shewanella oneidensis* native metallized biomass has been shown to be capable of use without sintering, implying intrinsic electron transport mechanisms between cells, but a heavy loading of Pd was required[35]. In this work two different approaches are utilised to overcome the problem of poor conductivity, first by the carbonisation of the biomass and secondly by stripping away a portion of the poorly conducting material. A range of techniques have been developed for the removal of surface contamination from nanoparticles, such as exposure to different atmospheres with[158,159] or

without[160] heating, refluxing in water[161], washing with acetone[162], electrochemical oxidation[163] and electrochemical deposition/dissolution of PbO_2 film[164]. These types of procedures can have a negative impact, with aggregation being a major issue[160,161] and introducing the potential for structural change[165], particularly at high temperature[166]. Calcination has been shown to be an effective method for this application, having been successfully applied to preparation of PEFC materials[155]. Whilst the stripping of biomass components could lead to agglomeration of nanoparticles, it was found possible to obtain conductivity without totally removing all the stabilising agents to leave catalytically active yet stable material[167]. In this case a partial removal of the biomass will leave a selection of organic ligands in contact with the nanoparticles.

5.2 Methods and Materials

5.2.1 Growth of Bacteria

Desulfovibrio desulfuricans NCIMB 8307 used for this study was grown as described previously[24]. The *Escherichia coli* MC4100 used for this study was pregrown aerobically in nutrient broth (NB) no. 2 (Oxoid) at 37 °C for 24 hours under constant agitation (180 rpm). Portions of culture were then used to inoculate sealed 200 mL serum bottles containing degassed minimal medium, described below, under oxygen free nitrogen (BOC), where they were grown anaerobically (37 °C, 48 h). Cultures were then transferred into sealed 2 L duran bottles containing 1.8 L of the same oxygen free minimal medium. Biomass was harvested during the mid-exponential growth phase (O. $D._{600}$ ≈ 0.2-0.25) via centrifugation, followed by

washing three times in 20 mM MOPS-NaOH buffer pH 7.0 (Sigma), and concentrating into a small volume of the same buffer such that the cell concentration was 40 mg/mL, dry weight. The suspension was then degassed, and stored under oxygen free nitrogen (OFN) at 4 °C until use, typically within 24 hours.

Minimal medium for *E.coli*: 12 g Tris, 0.62 g KCl, 0.96 g $(NH_4)HPO_4$, 0.063 g $MgSO_4.7H_2O$, 0.33 mg $FeSO_4.H_2O$, 4 g sodium fumarate, 5 mL glycerol and 3.6 g glucose with distilled water to bring volume to 1000 mL and pH adjusted to 7.2 using HCl. Glucose was sterilised separately.

The optical density at 600 nm was converted to the cell concentration (mg dry weight/cm^3) using a previously identified calibration[5].

5.2.2 Biosorption and Bioreduction of Platinum

For the bioreduction 2 mM K_2PtCl_6 (≥99.9 %, Aldrich) in 0.01 M HNO_3 (Sigma Aldrich) was used as the platinum source. Prior to use this was degassed and stored under OFN at 30 °C. Cell suspension was added to the platinum solution such that the platinum quantity relative to the biomass was 5 % w/w. An additional amount of pH 7.0, 20 mM MOPS buffer (also previously degassed and stored under OFN) was added such that the ratio between platinum solution and MOPS buffer was 3:1. The ratio is required to maintain a low pH of around pH 2.5 as this has been found to elicit optimum metal uptake[24,40,56].

Following inoculation, the mixture was placed in a heater shaker at 37 °C and 180 rpm for 30 minutes to allow for biosorption to occur. Subsequently the solution was sparged with hydrogen (30 min) then pressurised under H_2 (1 bar) and returned to the heater shaker (overnight) to make, from *D.desulfuricans* and *E.coli* respectively, Dd-Pt and Ec-Pt, loaded to 5 % mass Pt. Complete removal of Pt onto the cells was confirmed by analysis[168] of the spent solution.

5.2.3 Sample Processing and Cleaning of Materials

Prior to cleaning, the biologically supported platinum (bio-Pt) samples were centrifuged and washed in distilled water 3 times to remove residual MOPS, and resuspended in ultra pure water. Native washed but otherwise uncleaned bio-Pt and commercial Tanaka Kikinzoku Kogyo (TKK) TEC10E50E (45.9 % Pt on C) platinum catalyst were used as controls.

For carbonisation the washed but otherwise uncleaned bio-Pt (100 mg) was suspended in 2 mL ultra pure water and placed into an alumina boat, which was in turn placed inside a quartz heating vessel that was connected to oxygen free nitrogen at 50 mL/min. This was heated within a furnace (THH12/90/305-2408CM&2116O/T, Elite Thermal Systems Ltd) with a temperature increase of 2.9 °C/min to 700 °C, held for 4 hours and cooled to room temperature, following the procedure of Yong *et al.* (2007)[155]. The resulting sample was then ground with an agate mortar and pestle.

For water reflux cleaning the bio-Pt sample (100 mg) was suspended in 10 mL ultra pure water and placed into a round bottomed flask with a condenser above. This was heated in

water to 90 °C, using the method of Lopez-Sanchez *et al.* (2011)[161]; the duration was extended to 36 hours due to the difference in stability between PVA and biomass. Once complete the bio-Pt was collected, washed, then resuspended in 200 µL ultra pure water.

A phenol-chloroform extraction was made by adding the bio-Pt (100 mg suspended in 10 mL distilled water) to a separating funnel. The same volume of phenol-chloroform-isoamyl alcohol mixture 25:24:1 (v/v/v) saturated with 100 mM tris buffer, pH 8.0 (Sigma) was added. The mixture was vigorously agitated by hand (5 min), then stood at room temperature (48 hours) to separate. The platinum bearing portion of the sample located mainly at the phase interface was collected, together with a small contaminating amount of the other phases. When the bulk of the aqueous and organic layers were removed, the nanoparticles dropped out of solution. Pt nanoparticles were further isolated by centrifugation (4,000 g) then resuspended in NaOH (5.5 M, 10 mL, 48 hours). Test samples had shown that direct resuspension in water, ethanol, methanol or acetone could not be achieved as the nanoparticles did not disperse. The residual suspended solid, containing platinum, was collected by centrifugation (4,000 g), washed in distilled water three times and finally resuspended in 200 µL ultra pure water.

For NaOH cleaning of bio-Pt samples (100 mg), the bio-Pt was washed three times in distilled water then suspended in 20 mL NaOH (5.5 M). The mixture was occasionally agitated and allowed to stand overnight at room temperature before centrifugation and resuspension in fresh NaOH[169]. This process was repeated 25 times. Remaining sample was washed three times in distilled water then resuspended in 200 µL ultrapure water. Once the NaOH had compromised the cell wall materials, the intracellular proteins and Pt-nanoparticles were

released. The NaOH was neutralised using HCl before centrifugation. A similar procedure was employed using water instead of NaOH as a control to ensure that any effects observed were due to the NaOH and not the water (no HCl was used in this case).

5.2.4 Preparation for Electrochemical Analysis

Electrochemical testing utilised 3 mm diameter glassy carbon (GC) electrodes which had been polished using 1 µm, 0.3 µm and 0.05 µm diameter alumina slurries (Micropolish, Buehler). Where possible the Pt samples were applied directly to the electrode by dropping a volume of 5 µL of sample solution upon the GC disc. This was only possible for non-carbonised samples, probably due to the presence of adhesive organic carbon material. The carbonised samples and the TKK commercial catalyst were in the form of a powder (platinum on carbon) therefore inks were made for application to electrodes according to the method of Takahashi and Kocha (2012)[170]. Immediately prior to deposition upon the electrode all samples were subjected to sonication within an ultrasonic bath (3 min) to improve Pt distribution across the electrode. In all cases initial tests used a range of sample concentrations to determine the loading which would give the optimum value for the specific catalysis. This was determined by testing a minimum of 4 different loadings with cyclic voltammetry (CV) and oxygen reduction reaction (ORR) analysis allowing for the plotting of loading against specific activity and diffusion limited current (Appendix IV) as per the method of Mayrhofer *et al.* (2008)[171]. From these the optimum loading (loading of highest overall magnitude across both tests) was obtained to ensure there was sufficient

platinum present for good oxygen reduction activity, but sufficiently low to be utilised maximally. Whilst the specific activity test (kinetic current per unit electrochemical surface area of Pt) can be expected to be poorer as platinum loading is increased, this would not be typically expected of the diffusion limited current test. The poorer diffusion limited current measured as Pt loading was increased in these tests likely originates from the increased amount of organic material hindering diffusion. Samples where Levich analysis showed the sample was not viable were not tested as fully due to time limitations.

5.2.5 Electrochemical Analysis

Electrochemical measurements were done at 298 K, controlled using a heated water bath and a pump feeding water into a jacket on the electrochemical cell. Measurements were made using a 3 electrode arrangement. The working electrode was the sample laden GC electrode, the counter electrode was a piece of Pt mesh and the reference electrode was a leakless Ag/AgCl reference electrode (eDaq, UK). The reference electrode was regularly calibrated and the potential was found to be consistent to within 5 mV. Experimental control was via an Autolab PGSTAT302N potentiostat operated using Nova 1.10 software (Metrohm, UK) and a rotating disc electrode setup (Origalys, France). The electrolyte employed was 0.1 M $HClO_{4\ (aq)}$, prepared from 70 % (AR, Fisher, UK) which was purged with either oxygen free nitrogen (BOC, UK) or 99.999 % O_2 (BOC Special Gases, UK) as appropriate (20 min prior to measurement).

Prior to measurements an electrochemical cleaning step was incorporated to enable catalytic activity on the surface of the platinum. This was conducted in nitrogen saturated electrolyte solution from -0.20 V to 0.85 V vs. sat. Ag/AgCl at a scan rate of 250 mV/s, which was done until a stable voltammogram was obtained (usually 50-100 cycles).

Electrochemical analysis involved a cyclic voltammogram (CV) using the same potential range as the cleaning, but using a scan rate of 25 mV/s. This was followed by linear sweeps using the same potential range and scan rate of 25 mV/s and with rotation speeds of 400, 625, 900, 1225, 1600, 2025 and 2500 rpm. The linear sweeps were repeated in oxygen saturated solution. The CV was repeated in nitrogen solution and the impedance at open circuit potential was measured.

The CVs were processed using Nova to determine the charge measured during hydrogen desorption by measurement of the area under the hydrogen desorption peak. With this, the electrochemical surface area, A_{EC}, and roughness factor, r_f, were calculated from Equation 5.1[171]. To ensure that the software was producing a true value, charge measurements it produced were compared with calculations from raw data using the trapezium rule.

$$r_f = \frac{A_{EC}}{A_{geo}} = \frac{Q_H}{\Gamma A_{\mathrm{geo}}} \tag{5.1}$$

where r_f is the roughness factor, A_{EC} is the platinum surface area, A_{geo} is the electrode area, Q_H is the charge measured upon desorption of a monolayer of underpotentially deposited hydrogen and Γ is the charge required to reduce a monolayer of protons. For this work the value of 210 μC cm_{Pt}^{-2} has been used[172].

The linear sweep data was normalised by the subtraction of linear sweep voltammogram (LSV) data in nitrogen saturated electrolyte solution from LSV data in oxygen saturated electrolyte in otherwise identical conditions. The data from this was analysed via Levich, Koutecký-Levich and Tafel plots to establish any diffusion limitation (and its degree), to compare kinetic current densities and to determine the number of electrons transferred in the reaction.

The Levich analysis utilises a plot of diffusion limited current against $\omega^{1/2}$, the relationship of which is described via Equation 5.2[143], which includes a range of known quantities for the reaction, electrolyte and electrode used. From these known quantities, information is revealed about the reaction kinetics (from the linearity of the plot), and whether the electrode surface is being effectively utilised.

$$i_{lim} = 0.62nFAD_O^{2/3}\omega^{1/2}\nu^{-1/6}C_O^* \quad (5.2)$$

where i_{lim} is the limiting current, n is the number of electrons transferred in the half reaction, F is the Faraday constant, A is the electrode area, D_O is the diffusion coefficient, ω is the electrode rotation rate (radians per second), ν is the kinematic viscosity and C_O^* is the bulk analyte concentration.

A Koutecký-Levich plot, from Equation 5.3[143], was used to obtain information about the kinetic current density, j_k, which is determined from the intercept on a plot of j^{-1} against $\omega^{-1/2}$. From the slope of this plot, it is possible to determine the number of electrons transferred per oxygen molecule, and thus gain information about the reaction.

$$\frac{1}{j} = \frac{1}{j_k} + \frac{1}{j_d} \tag{5.3}$$

where j is the total current density at a particular potential, j_k is the kinetic current density at that potential and j_d is the diffusion limited current density, as described in Equation 5.2.

Tafel plots were created of $\log_{10} j_k$ against the overpotential, η, such that the intercept is $\log_{10} j_0$, where j_0 is the exchange current density, and the slope shows the number of electrons transferred in the rate limiting step via Equation 5.4.

$$slope = -\frac{\alpha_c nF}{2.3RT} \tag{5.4}$$

where α_c is the cathodic transfer coefficient, n is the number of electrons transferred in the rate limiting step, F is the Faraday constant, R is the ideal gas constant and T is the temperature.

Tafel plots were created twice per experiment. One was plotted using the kinetic current density values obtained from the Koutecký-Levich plot utilising the different rotation speeds. The other used values of j_k obtained through Equation 5.5[171], from data obtained at 1600 rpm.

$$j_k = \frac{i_k}{A_{EC}} = \frac{i_d \, x \, i}{i_d - i} x \frac{1}{\mathrm{r_f} \, x \, A_{geo}} \tag{5.5}$$

5.2.6 Physical Characterisation of Bio-Pt Samples

Physical characterisation of the catalyst samples was done using transmission electron microscopy (TEM: FEI Tecnai TF20: 200 kV). For this, carbon coated copper 400 mesh grids (Agar Scientific) were loaded with sample via pipetting (2 µL per grid). Thin film X-ray diffraction (XRD: Bruker D2 PHASER with LYNXEYE detector: Co-Kα X-ray source: 40-50° scans, 13 min each: 15 rpm sample stage rotation) was also employed. For this, sample preparation involved diluting 5 µL of samples into water, water:isopropyl alcohol mixture (3:1 v/v) for the ink based samples, which were then applied to silicon wafer, roughly 1 cm^2 in 10 µL quantities, over a course of deposition and evaporation steps. XRD data analysis was done using Origin software to achieve peak fitting. This data was then further analysed using the Scherrer equation (Equation 5.6) to gain information about the particle size.

$$B = K\lambda / \left(Lcos\frac{\chi}{2}\right) \tag{5.6}$$

where B is the full width half maximum value of the diffraction peak in radians after subtracting the instrumental broadening, λ is the wavelength of the incident x-rays, L is the crystallite diameter, χ/2 is the Bragg angle and K is a dimensionless shape factor. For this work K has been assigned a value of 0.9[173].

Inductively coupled plasma mass spectrometry (ICP-MS) measurements were conducted to determine the quantity of Pt present in the samples post cleaning using an Agilent 7500ce ICP-MS with an octopole reaction system (ORS) to remove polyatomic interferences. Pt was analysed at mass 195. The plasma runs with an RF power of 1500 W. A Miramist nebuliser was used for sample introduction. Detection limits were approximately 0.005 ppb for Pt. For

this a small volume of the sample was suspended in freshly prepared aqua regia to solubilise the Pt nanoparticles (2 days). The sample was then diluted to 0.07 % HNO_3 / 0.11 % HCl for ICP-MS analysis.

5.3 Results and Discussion

Cyclic voltammetry results give an indication of the availability of platinum, and thus the effectiveness of each cleaning technique. In the case of Ec-Pt (Figure 5.1) the magnitude of the ECSA observed followed the order NaOH washed >> water washed > sintered > refluxed > phenol chloroform extracted ≈ native. The Dd-Pt samples (Figure 5.2) ECSA magnitude follows the order phenol chloroform extraction >> NaOH washed > refluxed > sintered > water washed > native. The sintered sample in each case possesses a very large capacitance, shown by the large baseline current, likely due to the remaining carbon. The best sample for both Ec-Pt and Dd-Pt possesses the structure that would be expected for Pt^{174}, as shown in Figure 5.1a and Figure 5.2a.

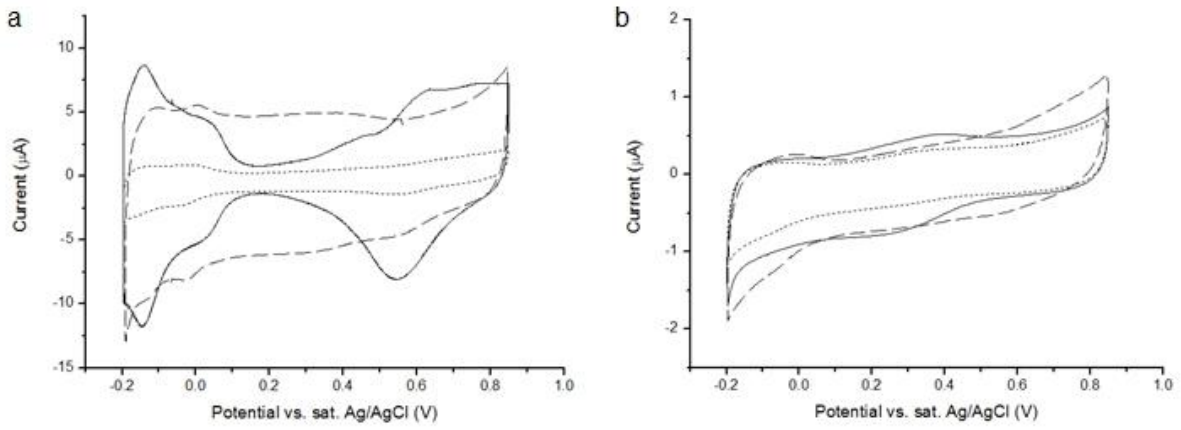

Figure 5.1, cyclic voltammograms, 25 mV/s, of cleaned bio-Pt produced using E.coli. a:- NaOH washed – solid line; sintered – dashed line; water washed – dotted line. b:- phenol chloroform extracted – solid line; water refluxed – dashed line; native – dotted line).

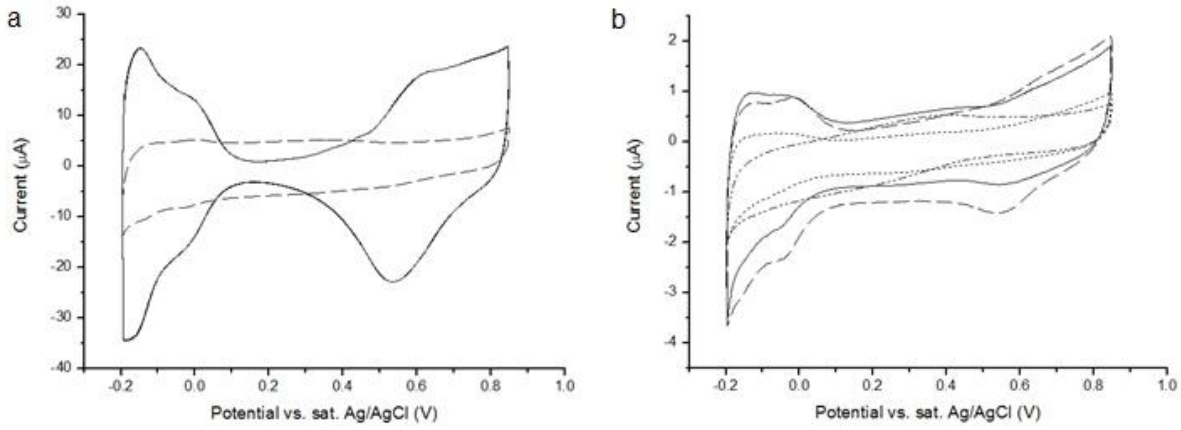

Figure 5.2, cyclic voltammograms, 25 mV/s, of cleaned bio-Pt produced using D.desulfuricans. a:- phenol chloroform extracted – solid line; sintered – dashed line. b:- NaOH washed – solid line; water washed – dashed line; water refluxed – dotted line; native – dotted dashed line).

The Levich plots (Figure 5.3) show that most samples possess limiting current, i_{lim}, below the theoretically expected values, determined from Equation 5.2. In the case of the uncleaned

control samples the current is 1 % of the expected value. Whilst the cleaned samples show improvements they are all less than the reference material (TKK). Some also show a slight non-linearity in the plots, appearing to tend towards a maximum value of current. This indicates that the reaction is being inhibited by the remaining biomass, likely due to impaired O_2 transport to the Pt surface. For Ec-Pt (Figure 5.3a) and Dd-Pt (Figure 5.3b), a single sample showed i_{lim} comparable to the TKK catalyst, i.e. NaOH cleaned and phenol chloroform cleaned in the case of Ec-Pt and Dd-Pt respectively, which were within 10 % of the value predicted by the Levich equation. The other cleaning procedures in each case are either incapable of providing the necessary Pt surface or would require more extensive application beyond the current scope of this work. Although sintered biomass produced an acceptable PEFC catalyst[155], Figure 5.3 shows clearly that chemical cleaning to (partially) remove biomass components is a preferable approach.

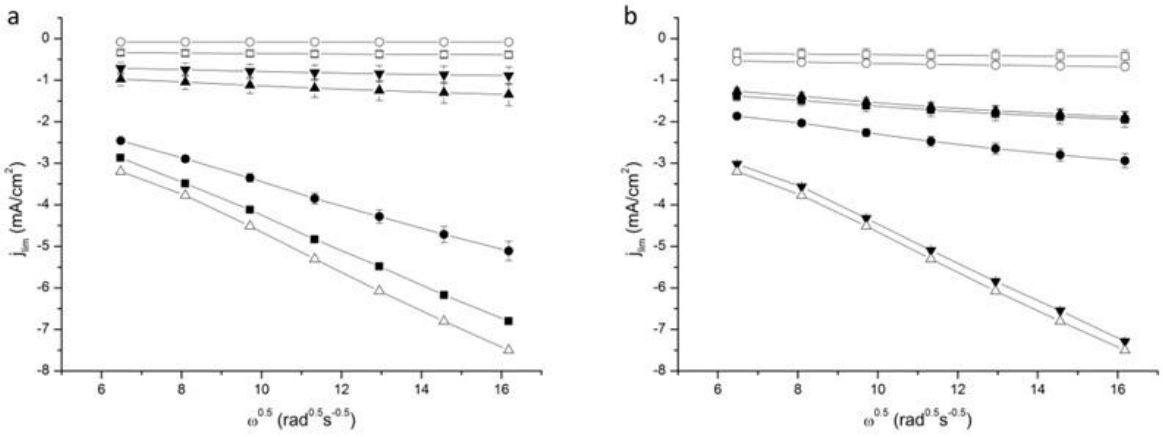

Figure 5.3, Levich plots, 25 mV/s, of Ec-Pt (a) and Dd-Pt (b) following NaOH (■), sintered (●), water washed (▲), phenol chloroform (▼), refluxed (□), uncleaned (○) and TKK (△). Error bars show standard error, where no error is shown this was within the dimensions of the symbols.

A comparison of the various cleaning procedures, focussing upon Ec-Pt, was investigated by TEM (Figure 5.4). The native, water washed and refluxed samples (Figure 5.4a-c) reveal rod shaped portions of biomass of the size and shape expected for *E.coli*, confirming that these cleaning methods have not disrupted the cell structure sufficiently to access the Pt within the samples. The presence of some disruption can clearly be seen in the water washed sample (Figure 5.4b, left arrow), with release of Pt nanoparticles (right arrow) that could potentially be accessed electrochemically. This would account for the superior limiting current compared to the native and refluxed samples. Whilst more biomass was removed from the phenol chloroform extracted sample (Figure 5.4d), the Pt still remains encased in residual biomass which explains the poor limiting current detected in electrochemical measurements.

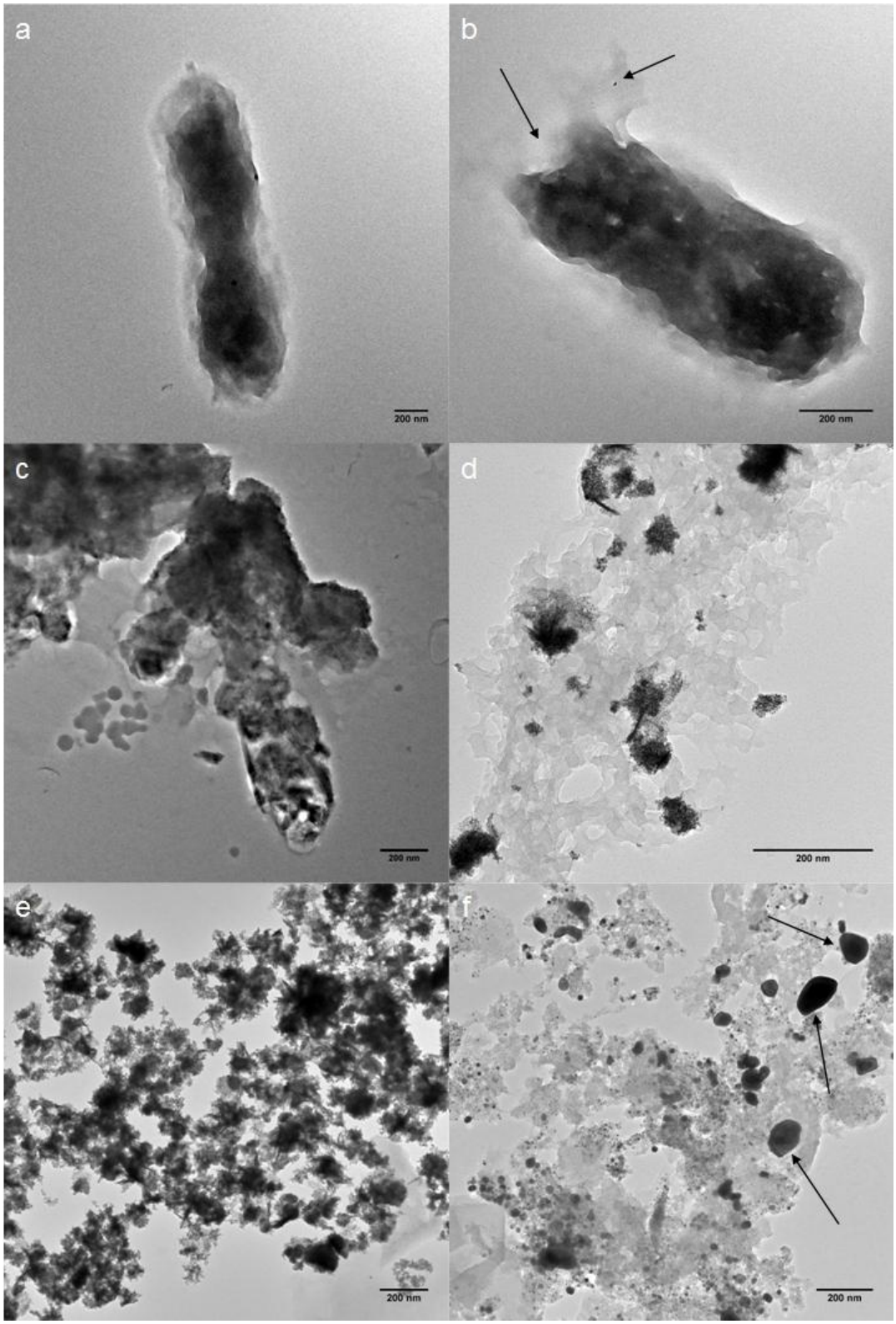

Figure 5.4, TEM images of Ec-Pt samples. a, native; b, water washed; c, water refluxed; d, phenol chloroform extracted; e, NaOH washed; f, sintered.

The NaOH washed sample (Figure 5.4e), has much less residual biomass than the other samples; confirming that the NaOH component and not the water component is responsible for the removal of biomass. As the presence of poorly conducting biomass was expected to inhibit electrochemical catalysis, this provides circumstantial evidence supporting the theory that the biomass component is the cause of inferior electron transfer to the Pt catalytic sites. Sintering has led to the formation of larger particles (Figure 5.4f arrowed), probably through Ostwald ripening[175]. Some of these larger particles appear to possess some surfaces free from biomass, which would explain why the limiting current for this sample is only surpassed by the thoroughly cleaned samples and the TKK control. However, in this study the sintered bio-Pt samples have not performed comparably to commercial Pt, whereas Yong *et al.* (2007)[155] found that it did. This discrepancy is likely the result of the lack of carbonisation, as Figure 5.4f shows that the carbon is still organic in nature rather than graphitic as was desired.

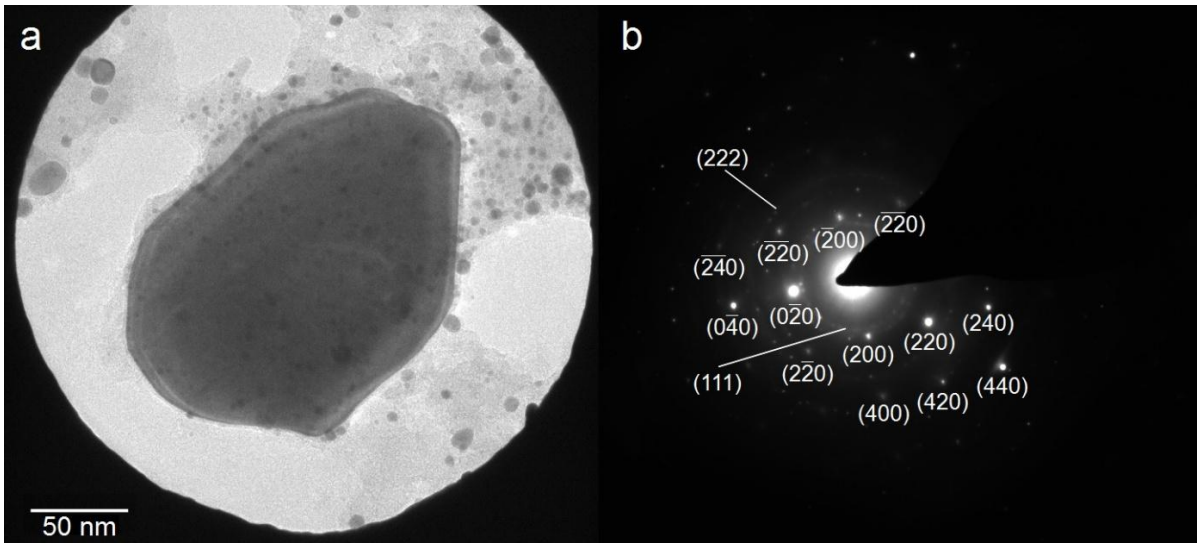

Figure 5.5, TEM image of Ec-Pt sintered sample (a) and the diffraction pattern it produced (b), with diffraction spots and rings indexed.

Figure 5.5 further investigates the structure of the larger particles observed with sintered Ec-Pt. The diffraction pattern produced is predominantly that of a single crystal as there are very clear spots produced, which also appears to be a single phase FCC structure. The smaller particles present in the image explain the presence of the faint rings in the diffraction pattern. This gives strong indication that the particles in this sample are not agglomerates of smaller particles. XRD data (Figure 5.6) indicates that particle size growth occurs regardless of the cleaning methodology utilised. This particle growth appears to be related to the aggressiveness of the preparation technique. Particle size determined by XRD (using a Gaussian fit) is shown in Table 5.1; however, accuracy is limited due to the broad peaks producing poor signal to noise.

Table 5.1, summary of particle sizes of Ec-Pt determined by XRD.

Sample preparation	Particle size (nm)
Sintered	50.7±0.6
Phenol chloroform extracted	6.8±1.1
NaOH washed	5.0±0.3
Water refluxed	3.9±1.0
Water washed	2.4±0.6
Native	1.3±1.3

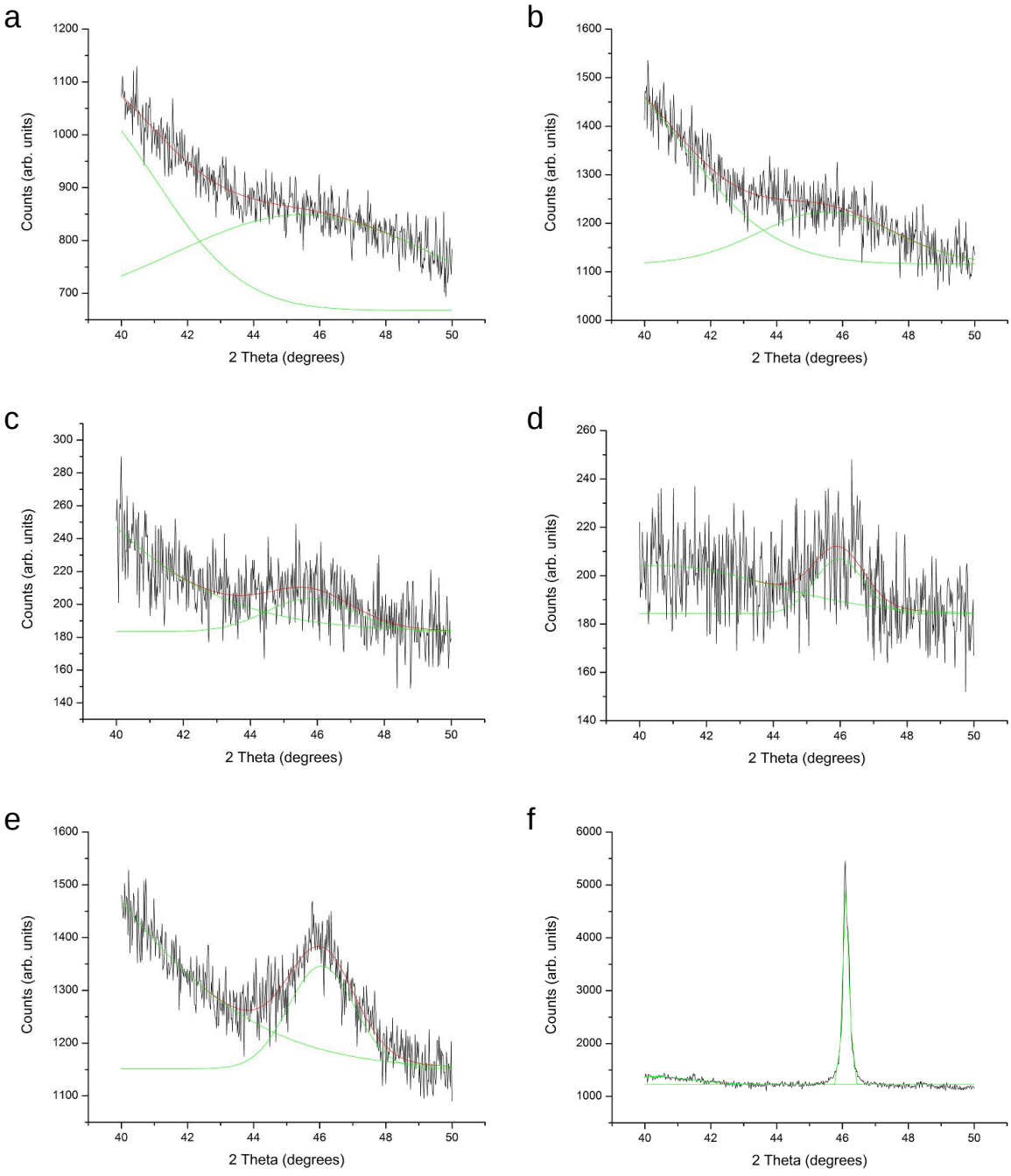

Figure 5.6, XRD data for Ec-Pt samples in the region of the Pt (111) peak, with Gaussian fit shown. a, native; b, water washed; c, water refluxed; d, phenol chloroform extracted; e, NaOH washed; f, sintered.

NaOH washed Ec-Pt and phenol chloroform extracted Dd-Pt were further investigated as these showed potential suitability for electrochemical catalysis of the ORR. Figure 5.7 shows apparent differences between them. This Dd-Pt sample, whilst cleaned sufficiently to allow for electrochemical application, still possesses enough biomass to prevent the same degree of agglomeration which has occurred in the Ec-Pt sample. It is unclear if these isolated nanoparticles are contributing to the electrochemical catalysis as there are still a large proportion of agglomerated nanoparticles which are not encased in biomass.

Comparison of CVs confirms unequivocally that the two biomass types respond differently to the use of cleaning procedures. While the Ec-Pt was revealed following NaOH washing (Figure 5.1) this procedure was ineffective for Dd-Pt (Figure 5.2) while, conversely, the phenol chloroform extraction procedure was highly effective for Dd-Pt but not for Ec-Pt.

Figure 5.7, and other micrographs at the same resolution, allowed for nanoparticle size measurements to be made. As the Dd-Pt sample shows isolated particles within the remaining biomass it was possible to use automated particle sizing in ImageJ via the use of thresholding to set the image to black and white, followed by the measurement of the black particles[176]. The same method was not possible for the Ec-Pt NaOH sample as no isolated particles could be located, thus measurement was done by the manual measurement of particles at the edge of clusters, also using ImageJ. The NP size was calculated as 4.0 and 1.2 nm for the Ec-Pt and Dd-Pt samples respectively (Table 5.2), in agreement with the calculations using XRD for Ec-Pt (5.0 nm) but similar calculations were not possible for Dd-Pt as no Pt XRD peaks could be distinguished from background noise. From these, the nominal nanoparticle surface area per gram of Pt was calculated using average particle

measurements, assuming that the nanoparticles are spheres and using the Pt density as 21.45 g/cm^3 [177]. However, the total available surface area per gram of Pt for NaOH washed Ec-Pt and phenol chloroform extracted Dd-Pt will be lower than is indicated from the single particle measurements due to the clustering that has occurred during cleaning.

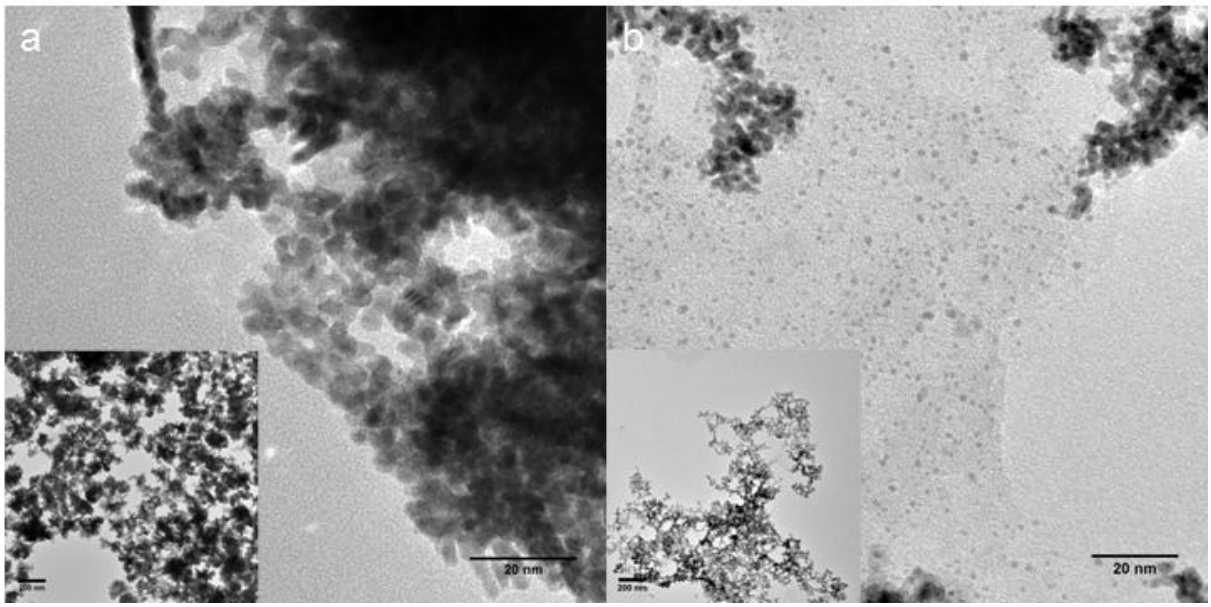

Figure 5.7, TEM images of Ec-Pt NaOH (a) and Dd-Pt phenol chloroform (b). Lower magnification images inset.

The intercepts of the Koutecký-Levich plots (Figure 5.8) show the theoretical situation of infinite electrode rotation rate where the total current density, j, is equal to the kinetic current, j_k. As the current is proportional to the rate of reaction, the kinetic current allows for comparison of reaction rate under the circumstance of a kinetically limited reaction thus showing which catalyst leads to a greater improvement in reaction rate.

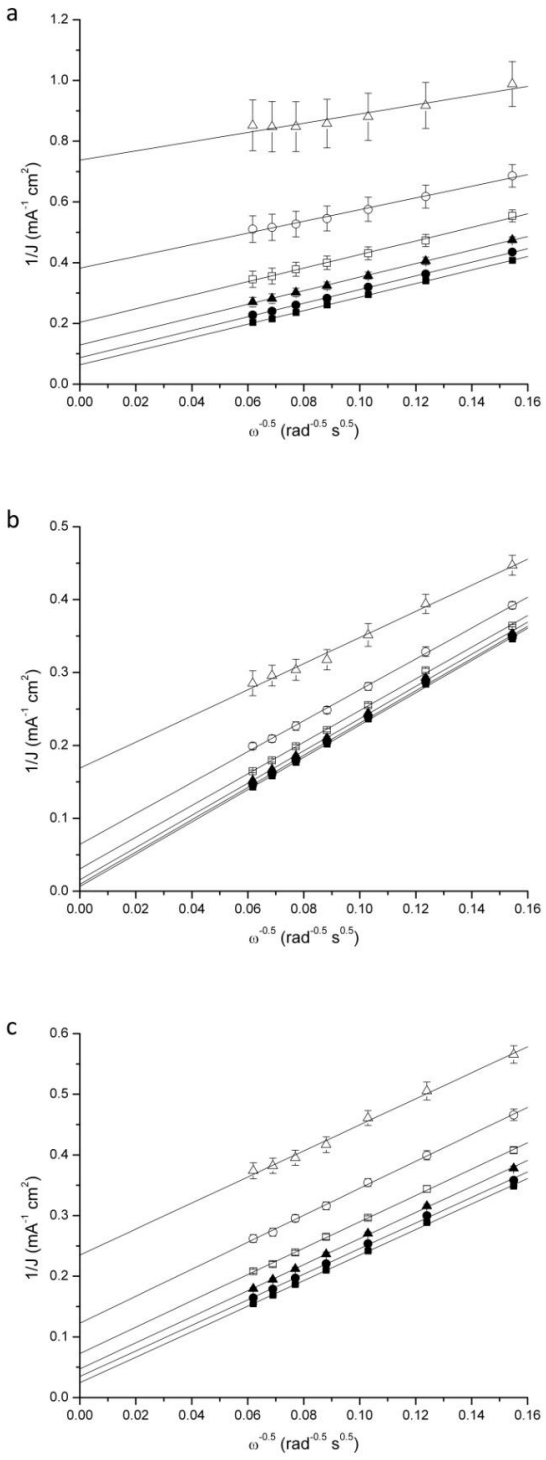

Figure 5.8, Koutecký-Levich plots of Ec-Pt NaOH (a), Dd-Pt phenol chloroform (b) and TKK (c). Data shown at 0.56 V (■), 0.58 V (●), 0.60 V (▲), 0.62 V (□), 0.64 V (○) and 0.66 V (△) vs. sat. Ag/AgCl. Error bars represent standard error.

Figure 5.8 shows that the intercept is smaller at each potential for the Dd-Pt sample than the TKK, thus the kinetic current density, j_k, for Dd-Pt is superior to TKK. The slope of the plots in Figure 5.8 allows for the determination of the electrons transferred per oxygen molecule; the average value of this is shown in Table 5.2. For a reaction where water is being produced there would be 4 electrons transferred whereas less desirable products, such as hydrogen peroxide, would lead to a lower value. All samples here are transferring approximately 4 electrons per oxygen molecule thus the reaction in each case is concluded to be primarily producing water.

Table 5.2, summary of ORR electrocatalytic properties for ORR reaction. Particle size was determined by TEM, A_{phys} is the Pt surface area calculated from particle size and bulk Pt density, ECSA is the electrochemically active surface area determined from the desorption of underpotentially deposited hydrogen, SA is the specific activity, MA is the mass activity, E_{half} is the half-wave potential and ET is the number of electrons transferred per O_2. Specific and mass activities were measured at 0.64 V vs. sat. Ag/AgCl. Standard error is shown.

Catalyst	Particle size (nm)	A_{phys} ($m^2 g_{Pt}^{-1}$)	ECSA ($m^2 g_{Pt}^{-1}$)	SA (mA cm^{-2})	MA (mA mg_{Pt}^{-1})	E_{half} (mV)	ET	Tafel slope (mV dec^{-1})
Ec-Pt NaOH	4.0±0.1	35±1	11.3±1.7	0.68±0.15	75±17	615±9	3.78±0.23	-58±2
Dd-Pt phenol chloroform	1.2±0.1	118±1	21.2±0.6	1.43±0.28	304±53	663±4	3.84±0.12	-55±2
TKK			83.7±0.2	0.45±0.02	374±4	645±2	3.86±0.07	-59±2

However, Table 5.2 shows that the mass related properties of the bio-Pt samples (particularly Ec-Pt) are inferior to TKK, possibly attributable to the clustering observed in Figure 5.7. The electrons transferred (Figure 5.8) and the Tafel slopes, calculated in the range 0.64-0.70 V vs. sat. Ag/AgCl (Figure 5.9a) are approximately 4 and 59 mV dec^{-1} respectively, indicating that four electrons are transferred per oxygen molecule, and two electrons are transferred in the rate limiting step as expected[178]. Half-wave potentials, the potential at which the current is half the value of i_{lim}, (Figure 5.9b) show that the Dd-Pt phenol chloroform sample is outperforming TKK by a significant margin. Furthermore, both bio-Pt samples show greater specific activity at 0.64 V vs. sat. Ag/AgCl than TKK. Hence, it is concluded that both bio-derived Pt catalysts function for the oxygen reduction reaction. It is unlikely that the improvement in activity arises from the biomass, which was concluded above to be a hindrance to electron transfer, thus we postulate that the improvement is probably the result of structural differences in the bio-Pt as compared to TKK.

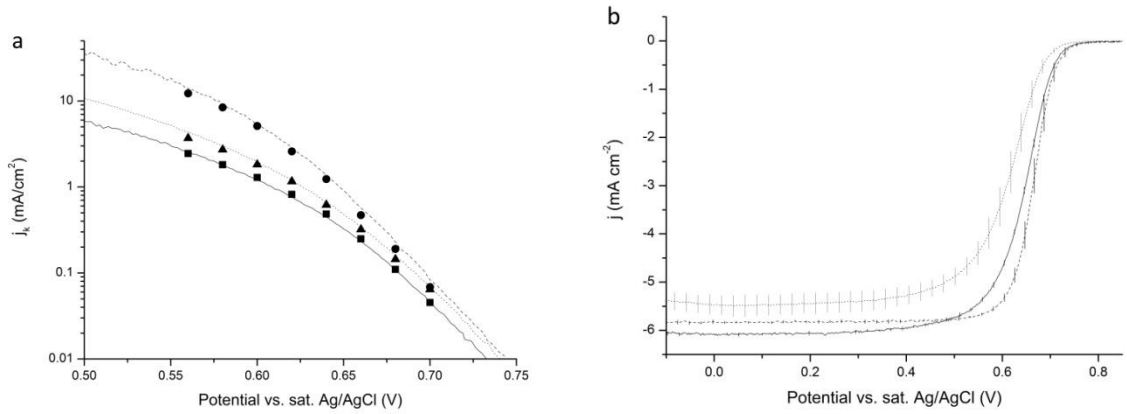

Figure 5.9, a, Tafel plots of TKK (■, solid line), phenol chloroform extracted Dd-Pt (●, dashed line) and NaOH cleaned Ec-Pt (▲, dotted line). Kinetic current density values determined from Koutecký-Levich plots are shown as symbols and kinetic current density values obtained from Equation 5.5 are shown as lines (1600 rpm). b, linear sweep voltammograms at 1600 rpm, 25 mV/s. TKK (solid line). Dd-Pt phenol chloroform (dashed line). Ec-Pt NaOH (dotted line).

These improvements cannot be attributed to being an effect arising from particle size; Nesselberger *et al.* (2011)[179] showed that such differences in particle size do not impact upon the specific activity. It is widely acknowledged that hydrogen adsorbs more strongly to some Pt crystal planes than it does to others[180-182]. Hence, it is possible to obtain information about the crystal facing of the Pt catalyst by comparing the CV against similar single crystal samples i.e. it can be determined that peaks at -0.131 to -0.136 V vs. sat. Ag/AgCl and -0.056 V vs. sat. Ag/AgCl are indicative of the (110) crystal orientation[183]. A pure (111) crystal has a 'butterfly' appearance, with minimal current between ca. 0.144 V and 0.344 V vs. sat. Ag/AgCl, with only one distinct peak located at 0.544 V vs. sat. Ag/AgCl, albeit associated with OH adsorption[182,184,185]. A pure (100) crystal shows a broad primary peak centred

~0.09 V vs. sat. Ag/AgCl[186]. A stepped structure will differ from these, for a Pt(S)-[n(110) x (100)] structure both (110) peaks shift negatively[187], whereas only the higher potential peak shifts negatively for Pt(S)-[n(110) x (111)][188]. In each case both peaks decrease in intensity as n decreases.

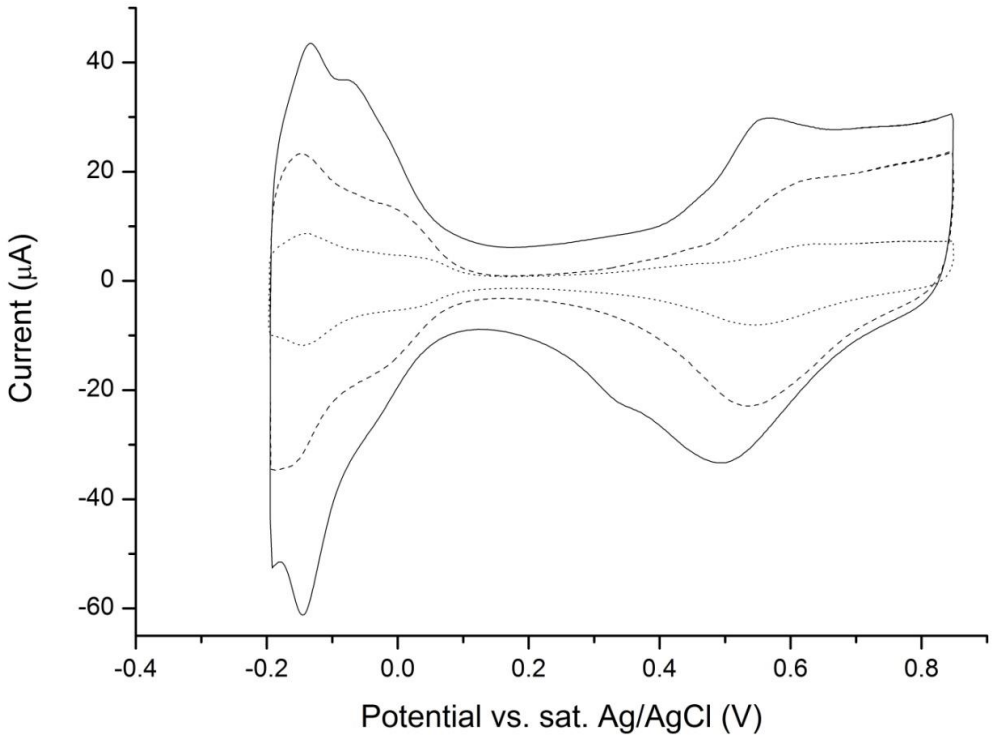

Figure 5.10, cyclic voltammograms at 25 mV/s. Solid line – TKK. Dashed line – Dd-Pt phenol chloroform. Dotted line – Ec-Pt NaOH.

By the comparison of the above values against those present for the TKK control (Figure 5.10) the peaks at -0.135 V and -0.08 V vs. sat. Ag/AgCl indicate the presence of a Pt(S)-[n(110) x (111)] structure as the initial peak is where would be expected for a (110) structure but the second peak is shifted negative of the -0.056 V that a (110) structure would

possess[188]. This assignation is supported by the broad peak at approximately 0.56 V vs. sat. Ag/AgCl, which indicates the presence of (111) structure. For the Ec-Pt NaOH and Dd-Pt phenol chloroform samples, the situation is less clear. In both cases only one peak is clearly present for (110) Pt suggesting that the structures are much more stepped, and there is no visible (111) peak beyond what could be accounted as arising from oxygen adsorption. In each case the clearly visible (110) peak has been shifted to negative potential, indicating a Pt(S)-[n(110) x (100)] structure[187]. Of the two bio-Pt samples the shift of the (110) peak indicates that n is greater for the Ec-Pt sample than the Dd-Pt one, however the lack of a (100) peak in each case indicates that neither possesses surfaces of this orientation. As a result it is likely that the majority of surfaces are stepped, which is unsurprising as Tritsaris *et al.* (2011)[189] has shown that the proportion of the surface of a nanoparticle that is stepped increases as the diameter decreases[189]. This expectation is further supported as some stepped surfaces have been found to possess greater half-wave potential than (100), (110) or (111) oriented Pt as is seen here with Dd-Pt, and others to be poorer, as is seen here with Ec-Pt (Figure 5.9b)[190,191].

5.4 Conclusion

Bio-Pt shows promise as being able to produce an effective ORR catalyst. Once the bulk of the biomass component is removed, it can achieve superior specific activity and half-wave potential when compared to TKK. This study shows that the bio-Pt formed by different

species of bacteria produce nanoparticles that differ in size and also in their structure, with more 'steps' being apparent in the smaller NPs produced on *Desulfovibrio desulfuricans*.

Figure 5.7 shows that a similar material is produced by each type of bio-Pt after appropriate 'cleaning'. Considering the potential for large scale production of catalyst, the use of *E.coli* is preferable to *D.desulfuricans* because it is already grown commercially at scale under high-yield conditions whereas *D.desulfuricans*, being obligately anaerobic, is low yield and not readily scalable. The major benefits of using *D.desulfuricans* compared to *E.coli* is that the nanoparticle size is smaller, leading to superior mass activity, and a more stepped structure, producing superior half wave potential. Both of these benefits result from the Pt nanoparticle structure. Nanoparticle formation on bacteria is heavily influenced by a range of criteria including, but not limited to, species[5,7,9,13,24,45,62,63], thus it is possible that Ec-Pt could be obtained in a form comparable to that of the Dd-Pt shown here, requiring only a minor change in preparation. One possibility for this is using formate as the reducing agent rather than hydrogen, which has been previously shown to produce smaller, thus probably more stepped, nanoparticles.

5.5 Acknowledgements

The authors are grateful to the Leeds EPSRC Nanoscience and Nanotechnology Facility (LENNF) and Dr. Zabeada Aslam for the TEM work done for this project.

6. MAGNETIC PROPERTIES OF BIO-PD STUDIED BY POPULATION AVERAGED AND INTERNAL MAGNETOMETRY TECHNIQUES

Palladium bionanomaterial manufactured using the sulphate-reducing bacterium *Desulfovibrio desulfuricans* has been reported to possess magnetic properties when analysed using Muon Spin Rotation Spectroscopy (μSR). In this study, time-resolved μSR was applied to identify and delineate behaviour attributable to the presence of paramagnetism, superparamagnetism and ferromagnetism occurring within the bionanomaterial. To gain insight into intra-sample environments, high resolution Scanning Transmission Electron Microscopy (STEM) was utilised to determine the palladium nanoparticle arrangements within the bacterial cells, enabling the allocation of three palladium nanoparticle types as responsible for the origin for each of the magnetic environments.

6.1 Justification for Using Bio-Pd

The electrochemical part of this thesis focusses upon the use of bio-Pt whereas the magnetism work has been done using bio-Pd. This is because bio-Pd and bio-Pt possess similar properties, but the magnetism can be expected to be greater in the case of bio-Pd as bulk Pd is closer than bulk Pt to fulfilling the Stoner Criterion for ferromagnetism[192]. Furthermore bio-Pd has already undergone some muon spin rotation (μSR) analysis which showed that ferromagnetism was present, but was unable to allow any in depth analysis due to having been done using a pulsed muon source which lacked the time resolution necessary to observe the rapidly relaxing magnetic component[193]. To achieve this, in depth analysis a

continuous muon source with greater time resolution was required. As μSR studies require cyclotron time, which is in high demand, it is necessary to submit an application with a strong scientific basis to be able to gain access. With a preliminary study having been done with bio-Pd, and a greater literature presence of ferromagnetic Pd than ferromagnetic Pt, bio-Pd had the greater chance of a successful application.

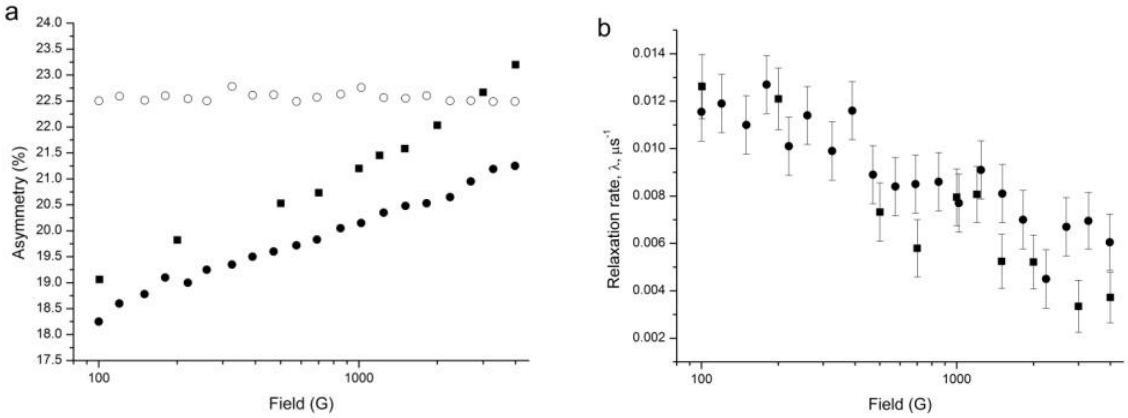

Figure 6.1, longitudinal field dependence of asymmetry (a) and relaxation rate (b) for magnetic bio-Pt (■), magnetic bio-Pd (●) and non-magnetic bio-Pd (○) measured at 300 K. Pd data adapted from Creamer et al*. (2011)*[193]*.*

A brief bio-Pt study (Figure 6.1) was done with a pulsed muon source to allow for comparison against the prior bio-Pd study[193]. By comparison, the bio-Pt asymmetry recovers by a greater amount than the bio-Pd as the applied field is increased which indicates that the magnetism is weaker in bio-Pt than in bio-Pd, as expected. The relaxation rates for bio-Pt and bio-Pd are the same within error. These show that the two materials possess similar properties under such an investigation, thus indicating that the origin of the magnetism could be the same for each material.

6.2 Introduction

Palladium nanoparticles have received a great deal of attention for catalysis of various reactions such as sensing[194-196], synthesis[197,198], dehalogenation[199-201] or oxidation[202-204] of a range of chemicals, hydrogen storage[205,206] and because of their magnetism[193,207-209]. Ferromagnetism of Pd is of particular interest as it is not a property shown by bulk Pd[210]; however Pd is known to be a paramagnetic material near to the ferromagnetic transition point, by analysis using Stoner's Criterion[192,211]. There have been investigations into the magnetism of this material where the nanoparticles have been prepared through chemical[207-209,212,213] or physical means[211,214] which have shown that magnetism may originate from the surface or the core of Pd nanoparticles. Surface ferromagnetism is proposed to arise due to the increase in the density of states at the nanoparticle surface[211,213] but may be blocked by adsorption of entities[215], whereas core ferromagnetism originates through alteration of the crystal structure relative to bulk[216-218], while the intensity of the core magnetisation is related to the occurrence of defects[219] and the degree of strain in the structure[214].

This work focusses upon Pd nanoparticles formed using the biological matrix of *Desulfovibrio desulfuricans* to assist in the reduction of Pd(II) to Pd(0) and to provide stabilisation against nanoparticle agglomeration[16,23]. Using the organism *D.fructosivorans*, Mikheenko *et al.* (2008)[16] provided evidence of the involvement of periplasmic hydrogenases (located near the bacterial surface), while Omajali *et al.* (2015)[30] showed the contribution of additional, intracellular mechanism(s) of intracellular Pd nanoparticle formation which are still not elucidated. The size and shape of the nanoparticles produced can be controlled by a range of

parameters, including pH[45], precious metal precursor[35,62] or reducing agent[35] which, in turn, can influence their ferromagnetism[213,216,220].

Bio-manufacturing and stabilization of Pd(0) nanoparticles enabled early observation of the magnetic property of 'bio-Pd' nanoparticles[221]. Creamer *et al.* (2011)[193] compared two bio-Pd samples, one possessing magnetisation in the order of 100 times greater than the other, as determined by SQUID magnetometry[193]. Muon spin rotation spectroscopy (μSR) revealed a difference in the asymmetry observed for these two samples with the less magnetically active sample displaying uniform asymmetry across a range of applied fields, whereas the strongly magnetic sample had a non-constant asymmetry as an external field was applied. This 'missing fraction' could not be investigated further due to the nature of the muon source used at the ISIS facility (Rutherford Appleton Laboratory, Harwell Oxford). Being a pulsed source, the EMU spectrometer implants a pulse of positive muons into the sample, 80 ns full width half maximum (fwhm),[222] and consequently there is a small time window after implantation which precludes investigation of the magnetism in this time frame. To gain further insight, greater time resolution is required to allow probing of the fast relaxing function of the muon decay, which formed the objective of this work.

This study utilises SQUID magnetometry and μSR analysis, with the latter achieved via a continuous implantation methodology where a single muon at a time is implanted into the sample for analysis, which allows for an improvement in the time resolution of the instrument to 1.25 ns[223].

This study also utilised a lower loading of Pd on biomass than described in earlier work, with

5 % (w/w) being used instead of 25 % (w/w)[193] in order to facilitate the production of smaller nanoparticles, with the goal of enhancing the magnetisation[213] and also potentially improving the catalytic properties by increasing the surface area per unit mass. This work is complemented by scanning transmission electron microscopy (STEM) coupled with a High Angle Annular Dark Field (HAADF) detector to facilitate understanding of the physical and biochemical parameters of bio-Pd biofabrication prior to future applications of synthetic biology to achieve a level of manufacturing control towards specific applications that physico-chemical methods cannot emulate.

6.3 Materials and Methods

6.3.1 Manufacture of Palladium-Loaded Bacterial Cells (Bio-Pd)

D. desulfuricans NCIMB 8307 was grown as described previously[8]. Cells were grown to the mid-exponential phase of growth before harvesting[193], washed three times in 20 mM MOPS-NaOH buffer (Sigma), pH 7.0, and resuspended in the same buffer to 30 mg of biomass (dry mass)/ml. An amount of this was then introduced to an anaerobic (degassed) solution of Na_2PdCl_4 (Aldrich, 99.995%) to allow for the dry mass of the product to be 5 % Pd and 95 % biomass (w/w). This suspension was left at 30 °C (30 mins) for biosorption of soluble Pd(II) ions. Hydrogen was then sparged through the solution (30 mins) resulting in the reduction of the Pd(II) which formed Pd nanoparticles on the biomass[16]. The mixture was incubated at 30 °C overnight to allow for complete reduction, confirmed by assay of the residual solution[23]. Palladised cells were washed three times in distilled water, then once in acetone

and left to dry in air. Dried preparations were ground to a fine powder using an agate mortar and pestle. All handling avoided the use of metallic implements.

Samples were prepared from multiple bacterial growth preparations which were combined. Palladisation was carried out using 2 mM (preparation A) and 10 mM (preparation B) palladium salts in 0.01 M HNO_3 with the cell concentration adjusted to give 5 % loading of Pd(0) in each case; experiments were done twice. For superconducting quantum interference device (SQUID) magnetometry each of the four 'bio-Pd' preparations was individually tested. For μSR analysis the two samples of each preparation were combined such that there was one common sample of each preparation.

6.3.2 Population Averaged Magnetometry

SQUID magnetometry (MPMS, Quantum Design, USA) was applied to gain an understanding of the bulk magnetic moments (emu/g) of the Bio-Pd powders. Prior to μSR analysis the induced magnetism was measured over a range of applied fields at 300 K as a screening procedure. Following the μSR analysis (below), the SQUID magnetometry was repeated utilizing the field and temperature combinations that had been used for the μSR analysis. The magnetic field was varied between ± 5400 Oe for the field scans, and the temperature between 5 and 300 K for temperature scans. All SQUID measurements were normalised to one gram of palladium, with the accuracy limited by mass determination.

6.3.3 Internal Magnetometry

Internal magnetometry measurements were made using Muon Spin Rotation Spectroscopy (μSR), which were done at the Paul Scherrer Institut, Switzerland (PSI) continuous muon source using the General Purpose Surface-Muon Instrument (GPS). This instrument operates using positive muons supplied with a standard momentum of 28 MeV/c, where muon polarization is >95 %. The detector arrangement consists of a total of 5 positron scintillation detectors, forward, backward, above, below and right with respect to the beam momentum[111]. Sample preparation involved pressing the bio-Pd powders into discs (6 mm diameter; force of 11 kN). These discs were then taped in place using silver on polyester tape (3M) and installed into the closed cycle cryostat (Janis with Sumitomo Heavy Industries Cold-Head).

Data from μSR was processed using the 'musrfit' package[224]. The time dependent decay asymmetry for the recorded counts of the forward (N_F) and backward (N_B) detectors can be described by the relationship in Equation 2.11. For this calculation scans were carried out with the application of a low intensity field transverse to the muon spin polarisation to allow for the calculation of alpha, which was used in subsequent processing of data from longitudinal field runs. The time dependence of the asymmetry can be described by Equation 2.12.

6.3.4 Analysis of the Palladium Component Using Electron Microscopy

Sample preparation for transmission electron microscopy used bio-Pd which had not

undergone a drying process. The fresh sample was resuspended in a fixative solution of 2.5 % glutaraldehyde in 0.1 M cacodylate buffer which was dehydrated using an ethanol series, set in resin and sectioned, with the sections placed onto a carbon coated copper grid[16]. Preliminary screening of samples was done at the University of Birmingham using a Jeol 1200EX TEM (80 kV). More detailed investigations of selected samples were made at the Universidad de Granada using a high resolution STEM/HAADF FEI TITAN G2 environmental TEM operating at 300 kV. Image analysis was carried out using 'ImageJ'[176].

6.4 Results and Discussion

For this study all samples comprised 95 % *Desulfovibrio desulfuricans*, 5 % palladium nanoparticles (w/w %), with an undetermined quantity of hydrogen probably remaining within the nanoparticles. Although samples were prepared using Pd salt precursor at two concentrations, the ratio of cells:metal was maintained at the same value in each preparation. However, cells in preparation B had suffered a 5-fold greater 'metal-shock' than those in preparation A, with the Pd (II) solution being roughly pH 2.3 in each case. Continued cell integrity and metabolism were confirmed by flow cytometry during exposure to 2 mM Pd(II)[30] but the biochemical impact of 10 mM Pd(II) was not investigated.

SQUID magnetometry measurements provide information about the population averaged magnetism of the sample (Figure 6.2). Both samples showed the non-linearity and hysteresis to indicate ferromagnetism, but with significant differences between them. Figure 6.2b shows that the coercivity and, to a lesser extent, the remanent magnetization were greater

in preparation B (from 10 mM solution) than in preparation A (from 2 mM solution), whereas the ferromagnetic saturation magnetization appears greater in the latter. However, due to the expected presence of paramagnetism within the samples, the determination of the saturation value of the ferromagnetic component is difficult.

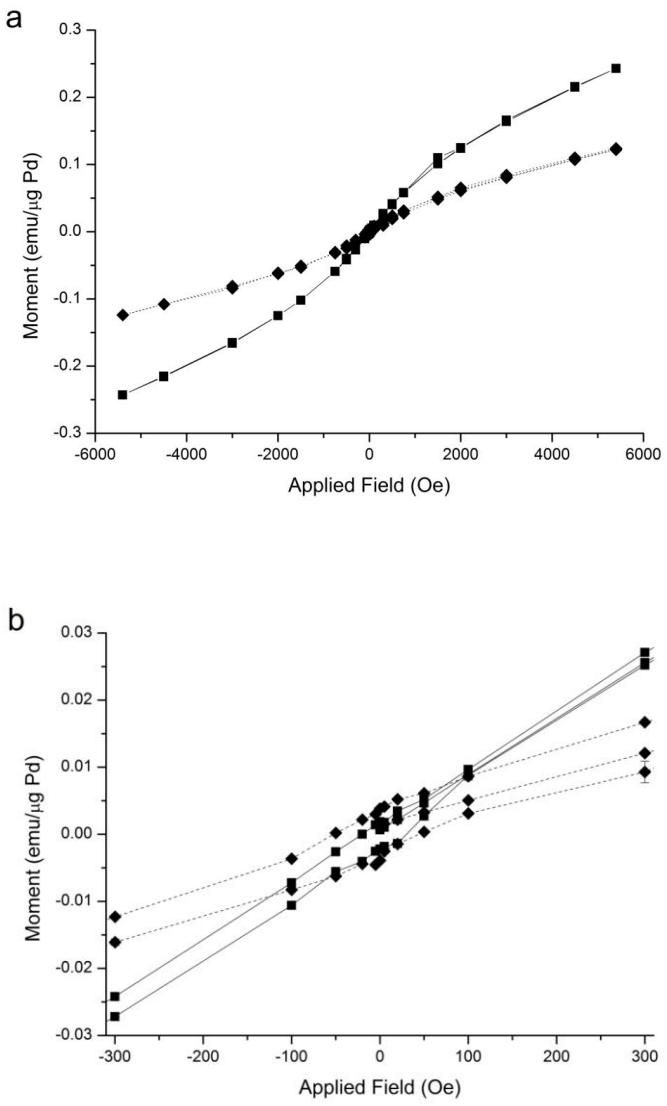

Figure 6.2, SQUID magnetometry moment normalised per mg of Pd against applied field at 5K. a: whole scale. b: expanded low field region. Error bars represent standard error. Samples were prepared using Pd(II) at: ■ and solid line, 2 mM; ◆ and dotted line, 10 mM.

Nanoparticle size has been shown to increase as Pd precursor concentration increases[35,63], thus it is to be expected that preparation B would comprise larger nanoparticles. However, Angappane *et al.* (2008)[213] showed that the magnetization, remanence and coercivity of Pd increases as particle size decreases; which is not observed here as the smaller nanoparticles expected for sample A possess poorer remanence and coercivity, but superior apparent magnetization (Figure 6.2). Such a difference could be explained if there are multiple magnetic types for the Pd present within the samples.

To gain further insight into the nature of this magnetism it was necessary to obtain local magnetism data via μSR as the population averaged measurements would include a range of different local magnetic environments. Measurements were made between zero applied field and 5400 G and between 5 K and 300 K. For this analysis $G_Z(t)$ (from Equation 2.12) includes 4 components, a non relaxing background component, a slow relaxing component and two fast relaxing components. The components can be expressed as shown in Equation 6.1.

$$G_z(t) = a_0 + a_S e^{\lambda_S} + a_{F1} e^{\lambda_{F1}} + a_{F2} e^{\lambda_{F2}} \quad (6.1)$$

where a_0 is the non relaxing background, a_S, a_{F1} and a_{F2} are the asymmetries of the relaxing components and λ_i are the corresponding relaxation rates with $\lambda_{F2} >> \lambda_{F1} >> \lambda_S$.

For the purposes of analysis it is assumed that the non relaxing background arises from muons stopped in the cryostat walls and the sample holder, or within the sample where the spin aligns with the applied field. The slow relaxing component (λ_S) arises from muons situated in biomass far from Pd. The first fast relaxing component (λ_{F1}) arises from muons

situated either in Pd nanoparticles or in biomass near to Pd nanoparticles. The second fast relaxing component (λ_{F2}), or 'missing fraction' as the relaxation is too rapid for analysis, arises from muonium formation within the biomass.

When the analysis as described in Equation 6.1 is applied to the muon data, 6 parameters are obtained (a_0, a_S, λ_S, a_{F1}, λ_{F1}, a_{F2}) as the relaxation rate of muonium (λ_{F2}) is too great to be determined. Analysis of λ_{F1} against applied field at 5 K and 300 K shows a total of three peaks (Figure 6.3), with the peak magnitude decreasing as the applied field increases. By comparing the field scans at 5 K against those at 300 K these peaks can be analysed.

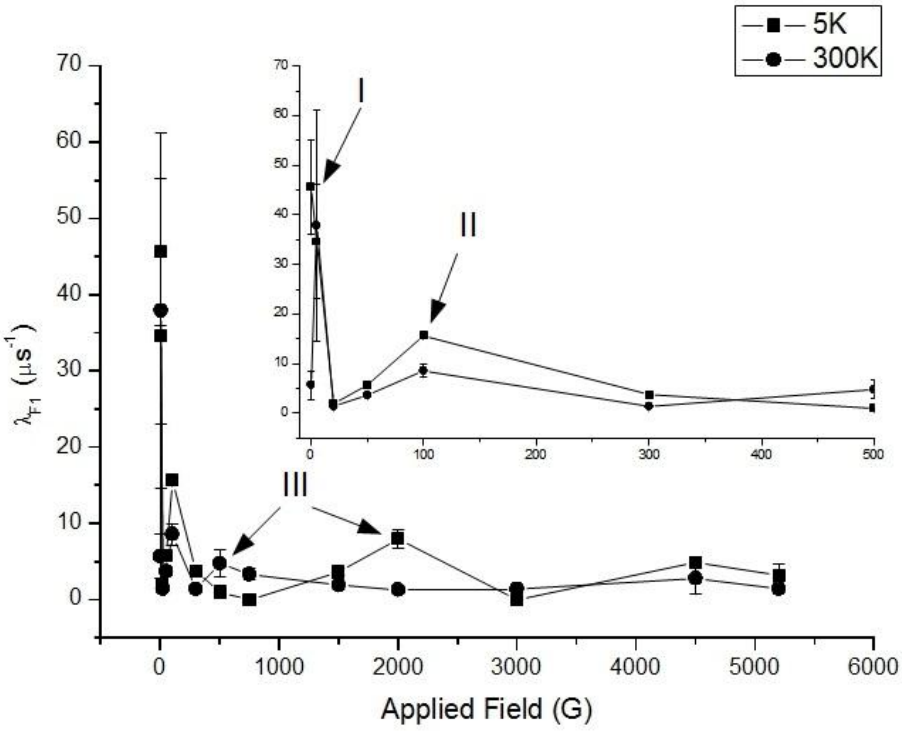

Figure 6.3, fast relaxation function field scan measurements at: ■, 5 K; ●, 300 K; using bio-Pd prepared from 2 mM Pd(II) solution (preparation A). Inset: expanded region from 0-500 G applied field. Peaks I, II and III are shown.

Figure 6.3 shows applied field scan measurements at 5 and 300 K. As an increase in temperature results in a reduction of the magnetic field strength of the Pd, the strength of the muon spin coupling is decreased and the relaxation rate is slower at higher temperatures. The first peak (Figure 6.3, Peak I) is evident at zero field in 5 K and at 5 G when the temperature was 300 K; in both cases this has largely disappeared by 20 G. This suggests that there is a superparamagnetic effect occurring within the sample where the temperature is greater than the blocking temperature i.e. the temperature at which the average relaxation time (in Equation 6.2) and the measurement time are equal. The middle peak (Figure 6.3, Peak II) occurs at 100 G field at both 5 K and 300 K indicating that this portion of the magnetism is not dynamic. The final peak (Figure 6.3, Peak III) occurs at a greater field in the 5 K environment than the 300 K one, indicating that this region is dynamic and ferromagnetic.

$$\tau_N = \tau_0 e^{\frac{KV}{k_B T}} \tag{6.2}$$

where τ_N is the Néel relaxation time, τ_0 is the attempt time, K is the magnetic anisotropy energy density of the nanoparticle, V is the volume, k_B is the Boltzmann constant and T is the absolute temperature.

To gain a greater insight into the origin of the three identified magnetic field types (superparamagnetic, non-dynamic and dynamic) further investigation of the Pd nanoparticles was necessary. STEM was used to identify structures within the sample which could potentially underlie the three different forms of magnetism identified by μSR. Electron opaque deposits in Figure 6.4 were identified by energy dispersive X-ray (EDX) microanalysis

as Pd (Figures 6.6 and 6.7), which also showed that Fe and Ni were not present beyond background level in either preparation. In Figure 6.4a, the bacterial cells are visible but are relatively ill-defined in the absence of staining agents. Higher magnification (Figure 6.4b) reveals the Pd to occur either as isolated particles or as clusters. Higher magnification shows the structure of the nanoparticles in the cell matrix (Figure 6.5a), to comprise a mixture of particles where some have a crystalline structure (Type I) whereas others are amorphous (Type II), providing different electronic environments[225]. The final electronic environment is particles which reside within clusters (Type III). We suggest that these three types of nanoparticles give rise to the three types of magnetic behaviour revealed by μSR.

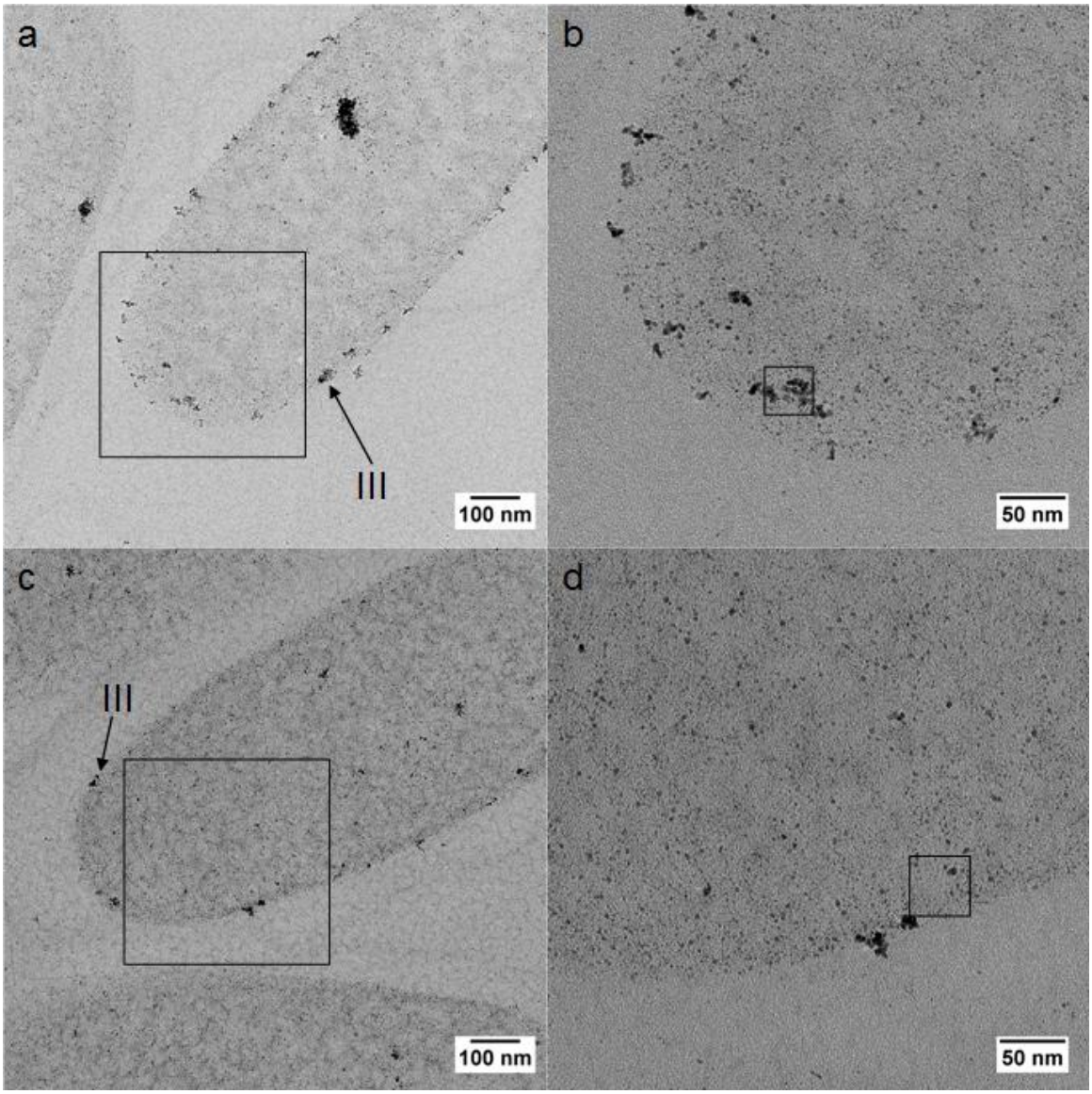

Figure 6.4, STEM micrograph of palladized cells which were prepared with a 2 mM Pd (a-b) or 10 mM (c-d) precursor solution. Boxes in a and c indicate the location of the image to the right and boxes in b and d are shown in Figure 6.5a and b respectively. Examples of type III structure indicated in a and c.

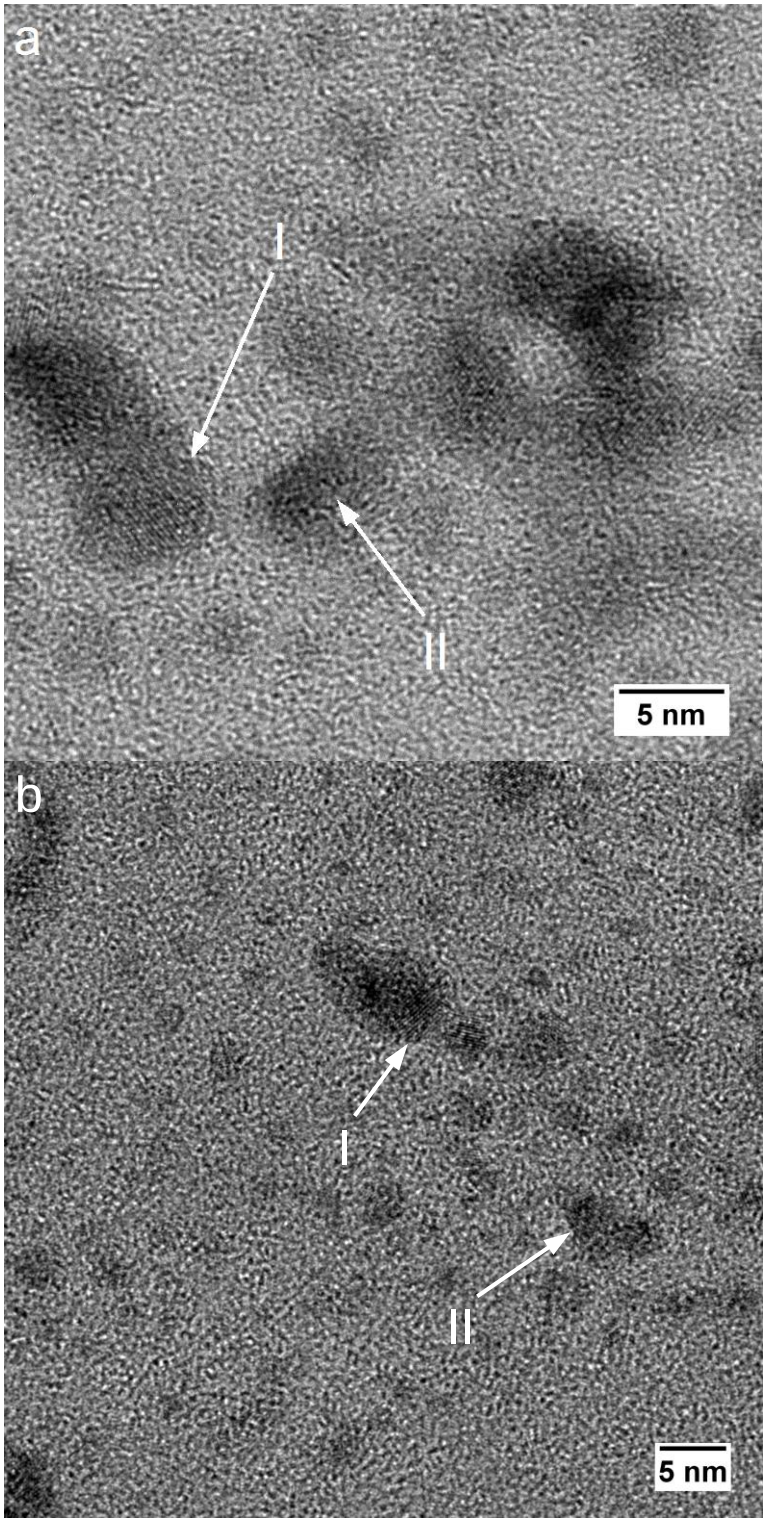

Figure 6.5, STEM micrograph of palladized cells which were prepared with a 2 mM Pd (a) (location indicated in Figure 6.4b) or 10 mM (b) precursor solution (location indicated in Figure 6.4d). Examples of type I and type II structure indicated.

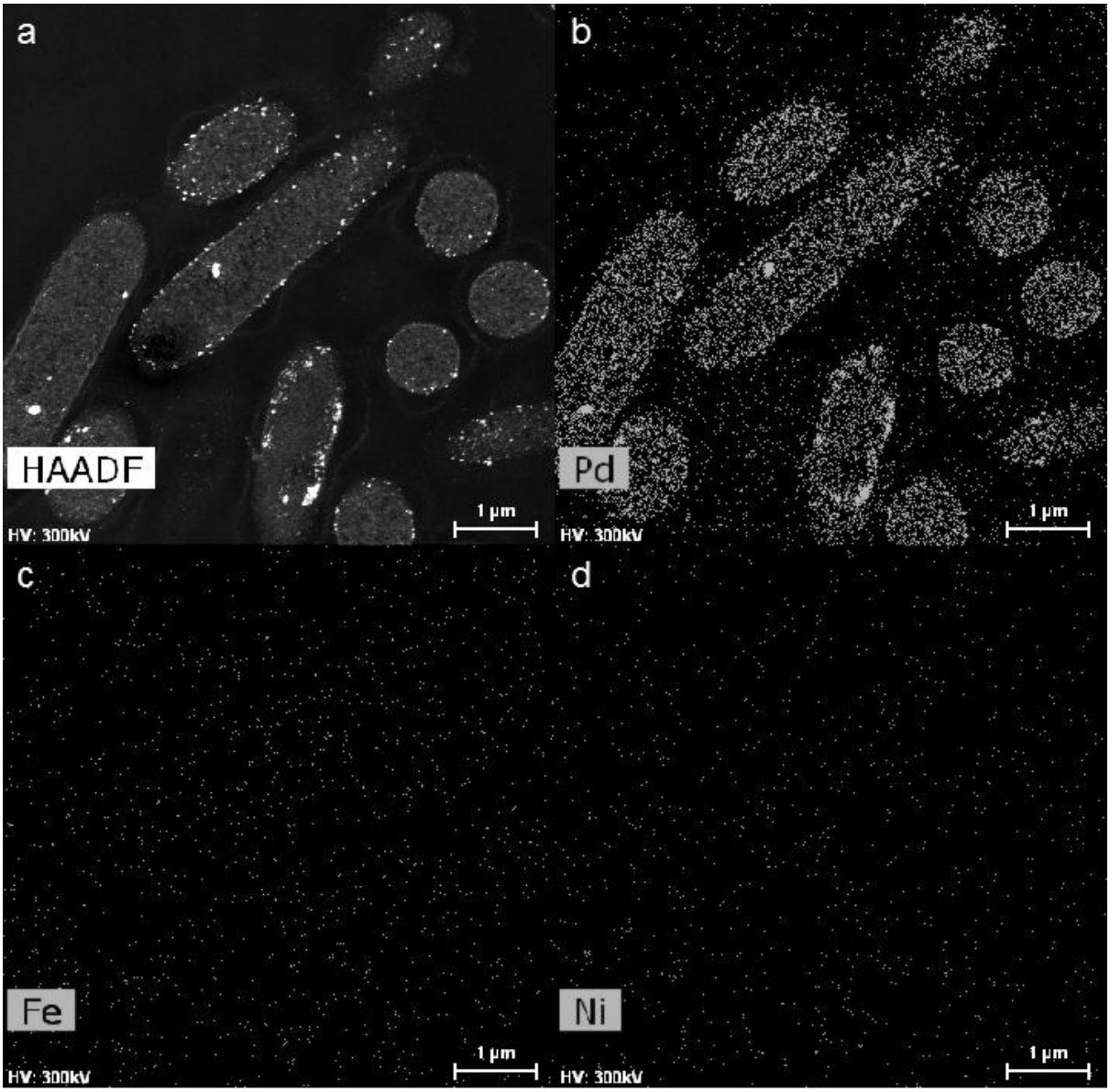

Figure 6.6, a HAADF image of magnetic bio-Pd preparation A. EDX images of the Pd, b, Fe, c, and Ni, d, content of the bio-Pd shown in a. Presence of the specific element is indicated by grey colour, whereas black colour indicates that none of the specific element is present in the bio-Pd represented in that area of image.

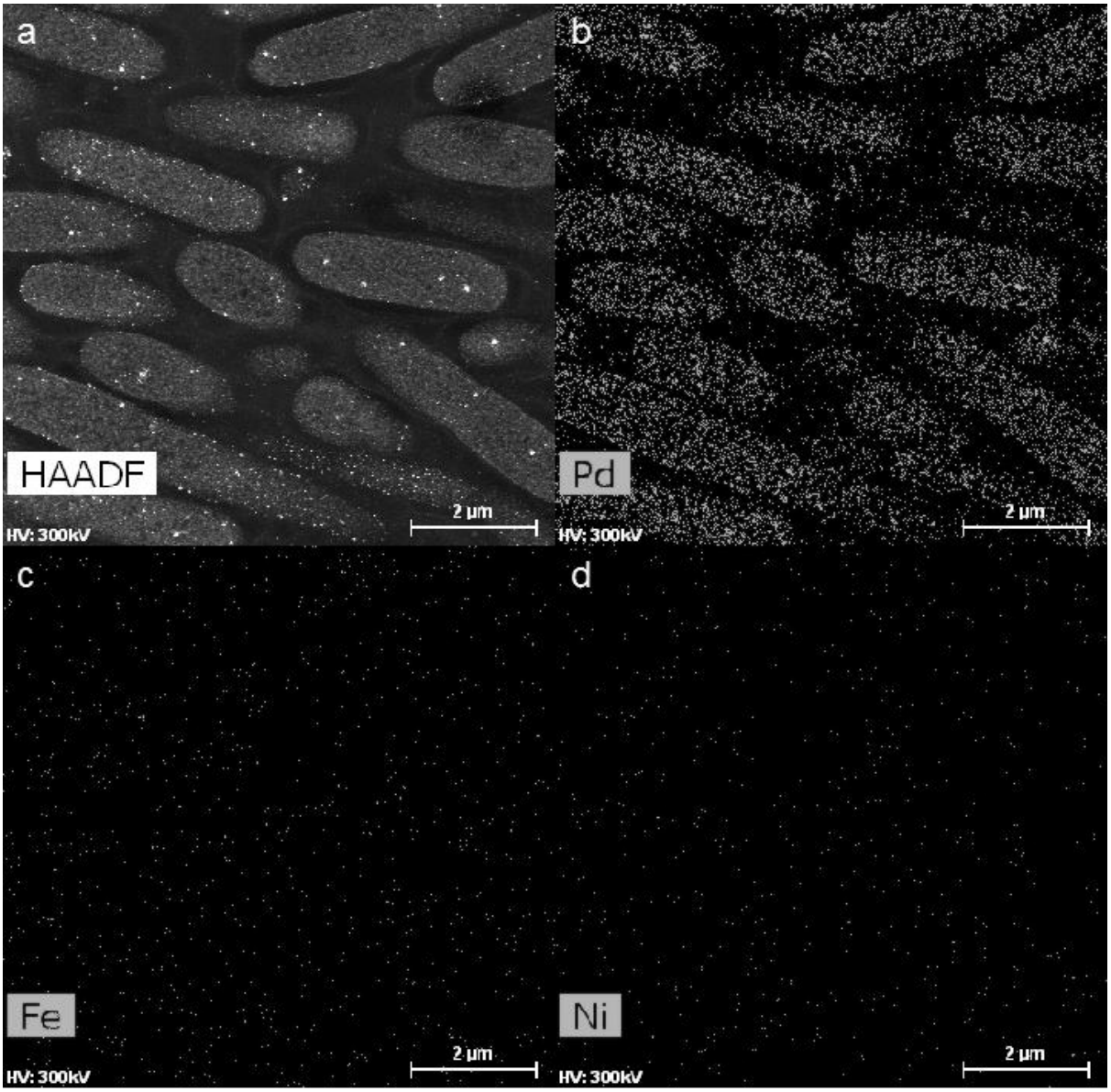

Figure 6.7, a HAADF image of magnetic bio-Pd preparation B. EDX images of the Pd, b, Fe, c, and Ni, d, content of the bio-Pd shown in a. Presence of the specific element is indicated by grey colour, whereas black colour indicates that none of the specific element is present in the bio-Pd represented in that area of image.

Hence, there are correspondingly 3 types of magnetism observed deriving from the Pd in preparation A. We suggest that the superparamagnetic portion (Peak I) identified in the µSR

analysis probably arises due to the presence of the single crystalline nanoparticles (Type I). The non-dynamic portion (Peak II) may be attributable to the paramagnetism exhibited by the amorphous nanoparticles (Type II). The ferromagnetic portion (Peak III) is exhibited by clusters comprised of crystalline nanoparticles or, possibly, a mixture of crystalline and amorphous nanoparticles (Type III). This interaction between the magnetic dipoles of neighbouring nanoparticles produces the necessary long range order for ferromagnetism, or rather superferromagnetism in this case[226-228]. As the same three types of structure can be observed in Preparation B (Figure 6.4b and d and Figure 6.5b), three magnetic types would also be expected.

μSR analysis of preparations A and B are compared in Figure 6.8. The similar behaviour in zero field to 20 G (Peak I) suggests that superparamagnetism is present in both. The peak around 2,000 G applied field (Peak III) is present in both preparations, as it is smaller in B it indicates a weaker form of the ferromagnetic behaviour. The paramagnetic peak (Peak II) from preparation A is also present in preparation B; however it is of greater magnitude in B than in A, and occurs at greater applied field, 300 G applied field in B compared to 100 G applied field in A (Figure 6.8, inset). Given these observations, the two samples might be expected to show differences in the arrangement of amorphous particles and the clusters. Accordingly STEM (Figure 6.4) shows fewer clusters present in preparation B than in preparation A, and comparison of Figure 6.5a and b shows that a greater proportion of amorphous nanoparticles are present in the case of preparation B.

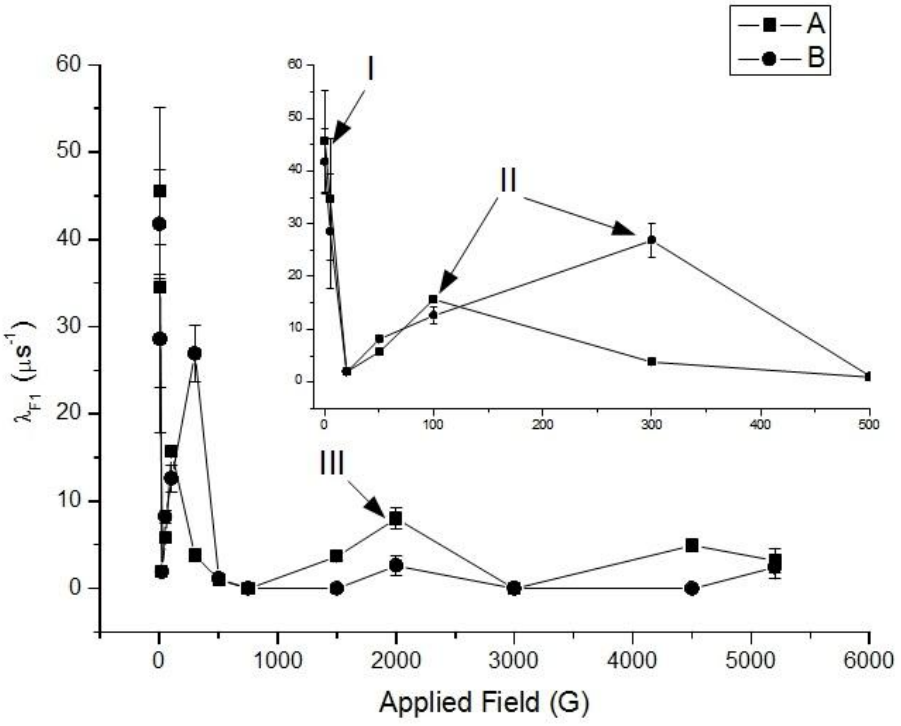

Figure 6.8, field scans at 5 K of the two differently prepared bio-Pd samples. Peaks I, II and III are shown.

High angle annular dark field (HAADF) micrographs (Figure 6.9) permitted measurement of the single nanoparticle diameters with TEM, showing that there are differences between the two samples. Individual particles appear to be of similar sizes with both samples having particles within the same size range but analysis of a population (Figure 6.9a and b) shows that the nanoparticles from preparation A tend towards a lower size than those of preparation B (Figure 6.9c), although the nanoparticles in preparation A have a greater tendency to form clusters than those of preparation B (Figure 6.4). The majority of the nanoparticles present in this study lie below the superparamagnetic limit where the nanoparticle possesses a single magnetic domain and behaves as a superparamagnet rather than a ferromagnet, which occurs between 0.9 and 2.0 nm diameter[207]. This high proportion

of small nanoparticles supports the assertion that the dynamic magnetism arises from superferromagnetism as the majority of the individual particles would not be expected to be ferromagnetic.

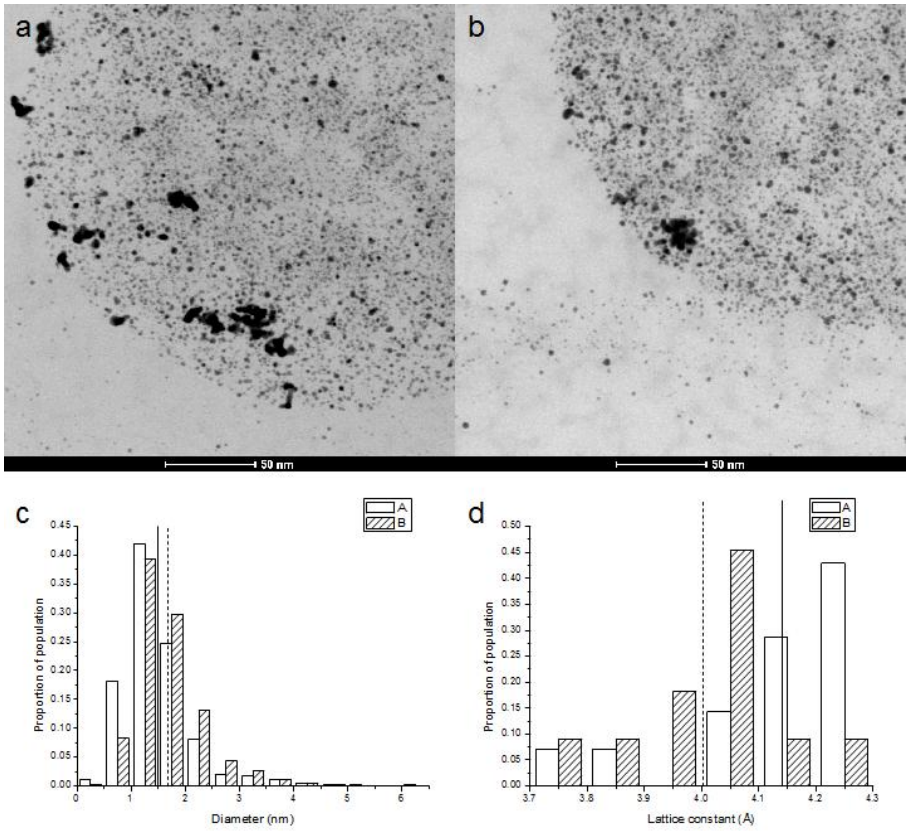

Figure 6.9, HAADF micrographs of preparation A (a), preparation B (b). These were analysed to generate a particle size diameter plot (c) as a proportion of population (n > 750; total population = 1) of bio-Pd from preparation A (2 mM Pd(II), □ / solid line) and B (10 mM Pd(II), ▨/ dashed line). Vertical lines represent mean particle size. A lattice constant plot (n > 10; total population = 1) generated from high resolution STEM analysis is also shown (d). Vertical lines represent mean lattice constant. Individual particle sizes and lattice constants were estimated from populations processed manually using ImageJ, particle clusters have not been included in this analysis.

The nanoparticle size difference between preparations could explain the difference observed between the relaxation rates of the paramagnetic sites. The muon relaxation rate is tied to the strength and also the orientation of the magnetic fields in their local environment[229]. If this environment is dominated by a paramagnetic particle, the field will increase as the applied field increases, up until the point where the internal field aligns with the applied field; at which point the relaxation rate will fall to zero. As the particles are of greater average size in preparation B they would require a greater energy input to cause this alignment. This would result in the relaxation rate increasing through a stronger applied field before falling, and achieving a greater magnitude in the process as is observed here.

To gain further insight into the superparamagnetic and superferromagnetic components of the magnetism arising from core behaviour we investigated the crystal structure of the crystalline nanoparticles by estimating the d-spacing of various particles ($n > 10$) from high resolution STEM images. These were converted into lattice constants with a [111] face-centred cubic (FCC) structure. Measurements were taken across multiple lattice fringes (usually 8-10). When the values from Figure 6.9d are compared to the bulk figure of 3.8898 Å[230] it can be seen that more than 80 % of the nanoparticles in each preparation have an expanded lattice. An expanded lattice results in an increased density of states, helping Pd fulfil the Stoner Criterion for ferromagnetism[217]. The onset of ferromagnetism is predicted to occur with a lattice expansion of 5-6 % greater than the equilibrium value[192,231,232], this is 4.08-4.12 Å. Approximately 60-80 % of the crystalline Pd in preparation A and 15-30 % of the crystalline Pd in preparation B have a structure within the ferromagnetic region, depending upon exactly what degree of strain is necessary.

Of the two samples, preparation A shows the greater ferromagnetic properties under μSR analysis (Figure 6.8) in accordance with the lattice expansion data of Figure 6.9d, yet preparation B shows the greater coercivity and remanence (from SQUID magnetometry, Figure 6.2). As the SQUID magnetometer measures the population averaged magnetism it is not possible to separate the various magnetic effects occurring; such resolution is provided by μSR. The lower coercivity in preparation A is likely the result of a greater quantity of superparamagnetic crystalline nanoparticles that rapidly align with the applied field, overwhelming the much smaller quantity of superferromagnetic clusters. From Equation 6.2, it is clear the greater particle volume of preparation B results in a larger relaxation time which we believe is the cause of its greater remanence.

6.5 Conclusion

A μSR investigation over a range of applied magnetic fields has indicated that there are three different magnetic effects originating from the Pd in a bio-Pd sample. Through application of temperature control, these effects have been determined to consist of a mixture of dynamic and non-dynamic properties. These effects have been correlated with 3 types of Pd structures determined through the application of STEM. A second sample with a different preparation procedure (greater Pd(II) concentration but the same overall loading) that would involve a more rapid Pd uptake process (i.e. increased stress on the cells) provides supporting evidence. This work indicates that the magnetism found within bio-Pd samples is a core based phenomenon which results from an expanded lattice.

6.6 Acknowledgements

The authors are grateful to Maria del Mar Abad Ortega, University of Grenada, for the TEM work done for this project. The authors would also like to thank Dr. Elizabeth Blackburn for helpful discussions.

7. USE OF MAGNETIC BIO-PT AS THE ELECTROCATALYST IN THE OXYGEN REDUCTION REACTION

Polymer electrolyte fuel cells (PEFCs) operate through the electrochemical oxidation of hydrogen and reduction of oxygen to produce an electric current that can be used to do work. Many potential applications of PEFCs avoid the use of an integrated oxygen supply as O_2 is freely available from the air. However oxygen is a minority component of air; this results in a lower partial pressure of oxygen in the fuel cell than from a pure supply. Through the application of a magnetic field it is possible to enrich the (paramagnetic) oxygen at the catalytic sites and thus improve the current generated. The magnetic field for this study is an innate feature of the bio-Pt(0) catalyst, thus promoting enrichment of oxygen. Tests were done using non-magnetised, sub-optimally magnetised and optimally magnetised catalysts using magnetic 'bio-Pt' catalyst and commercially available non-magnetic catalyst (Tanaka Kikinzoku Kogyo), revealing the benefit of an optimally magnetised magnetic catalyst upon the diffusion limited current which surpassed that of the commercial material.

7.1 Introduction

In a polymer electrolyte fuel cell (PEFC) the cathodic oxygen reduction reaction (ORR) is substantially slower than the anodic hydrogen oxidation reaction[233]. There has been a great focus towards improving the power output of PEFCs, including significant efforts towards increasing the rate of this half reaction[234-236]. Whilst typically the oxygen is provided by utilising air, it is possible to improve performance by increasing the oxygen proportion in the

feed[237]. However, oxygen is less than 21 % of the atmospheric composition. Other molecules can inhibit performance by passively or actively blocking the platinum catalyst sites, limiting the catalyst utilisation. Nitrogen does not take part in the reaction, and does not interact with the platinum catalyst, but it can be viewed as a diluent which passively blocks the catalyst[238]. Other molecules, such as carbon monoxide (if present), actively block catalyst sites by interacting with the platinum[239].

A pure oxygen supply may be suitable for some niche situations where cost and gas storage are not limitations; however for many applications this would be unsuitable[240-242]. Therefore, most operations result in much of the platinum catalyst being under-utilised. A major limitation of widespread implementation of PEFCs and hence the 'hydrogen economy' is the high cost of platinum. To minimise the impact of this problem it is necessary to increase the incidence of oxygen upon the catalyst, e.g. by improving the diffusion of oxygen to the catalytic sites[243,244].

Much of the core understanding of the magnetic properties of gases comes from the work of Faraday, who observed that nitrogen, relative to oxygen, was deflected away from a magnetic field, indicating that nitrogen is more diamagnetic than oxygen[245]. Later, with a greater understanding of molecular orbital states and interaction between magnetic fields and electron spin states, it was realised that the dioxygen molecule exhibits paramagnetism[246]. As such, the application of a magnetic field could provide the desired improvement in oxygen convection.

In the case of materials where the highest energy occupied molecular orbital (HOMO) is not fully occupied, electrons will occupy an energy state singly where possible; due to Hund's rule of maximum multiplicity[247]. This leads to a scenario with one or more electrons where their spin state is free to reorient, provided they all maintain the same orientation; this is a paramagnetic material. When there is no external magnetic field and no intermolecular coupling between spin states (as is present in ferromagnetic materials) the net magnetic moment of the material will be zero. When an external magnetic field is present the electron spins are more likely to occupy the energetically favourable spin state, resulting in a net magnetic moment aligning with the magnetic field. For paramagnetic materials the quantity of electrons bearing the energetically preferential spin is determined by the strength of the field and the local temperature, as the field will cause the electron spins to align; however, the temperature causes increased randomness as it rises[248]. A paramagnetic material responds to an external field but it does not generate one in isolation.

If the HOMO is fully occupied then electron spins are effectively locked due to Pauli's Exclusion Principle preventing two electrons in the same energy state bearing the same spin; this is a diamagnetic material. For such materials there is no energy benefit from exposure to magnetic fields as the electron spins do not allow for any net alignment with the field. Furthermore, the field induces a current in the molecules, which in turn leads to a magnetic field. This field is oriented such that it opposes the field which created it, thus leading to a repulsive force[248]. Whilst this effect also occurs in paramagnetic materials, the magnitude of the field arising from spin alignment is much greater than that of the induced currents.

Studies investigating the enrichment of oxygen to the catalyst have utilised the application of a magnetic field within the catalyst layer[249,250]. It is important to note that for the magnetic field to promote enrichment the field should be of a non-uniform nature[251]; Coey *et al.* (2007) showed that the force exerted on a fluid by a uniform magnetic fluid is minimal and, with the exception of ferrofluids, incapable of having any appreciable effect upon convection[252]. As oxygen is paramagnetic it has magnetic susceptibility that is not sufficient to result in any enrichment in a uniform magnetic field. When the magnetic field is non-uniform, the force exerted upon a species is described by Equation 7.1[251,253].

$$F_K = \frac{\chi}{\mu_0} B \nabla B \tag{7.1}$$

where F_K is the Kelvin force, χ is the volume magnetic susceptibility, μ_0 is the magnetic permeability of vacuum, B is the magnetic flux density[251].

Monzon and Coey (2014)[254] use this equation to demonstrate that a non-uniform field can influence the convection of paramagnetic species, such as oxygen. Hence, it was shown that a properly aligned magnetic field is capable of achieving oxygen enrichment, due to oxygen paramagnetism, whilst other fluids typically present for the oxygen reduction reaction (such as nitrogen when an air feed is used) are diamagnetic[255]. These diamagnetic species experience an equivalent effect to that of oxygen, but with opposite orientation due to having negative magnetic susceptibility. The optimal orientation for the non-uniform magnetic field is perpendicular to the plane of the catalyst layer as this will allow the field to best extend out into the fluid[252,253].

Furthermore the Lorentz force also provides a benefit to convection. The interaction between the orientation of the magnetic field and the direction of current lead to the appearance of a Lorentz force travelling circularly around the plane of the electrode[256]. As such, this improves the convection of species to the catalyst, reducing the thickness of the diffusion layer and increasing the limiting current (Equation 7.2).

$$i_{lim} = nFAm_O C_O^* \tag{7.2}$$

$$m_O = D_O/\delta_O \tag{7.3}$$

where i_{lim} is the limiting current, n is the electrons transferred, F is the Faraday constant, A is the electrode surface area, m_O is the mass-transfer coefficient of the oxidising species (Equation 7.3), C_O^* is the bulk concentration of the oxidising species, D_O is the diffusion coefficient of the oxidising species, δ_O is the diffusion layer thickness of the oxidising species[143].

Experimental evidence of the influence of magnetic fields upon the oxygen reduction reaction has been shown previously, showing improved current density compared to a non-magnetised sample[249,257] and a shift in the equilibrium potential[250,258]. These previous works investigated the effect of including ferromagnetic particles[257,259] or wires[260] within the catalyst layer to provide the magnetic field, increasing the complexity of the catalyst. The objective of this study was to use a ferromagnetic catalyst to produce the same effect i.e. to enrich oxygen directly at the catalytic sites and negate the requirement for additional materials to be introduced into the catalyst layer.

Nanoscale platinum has been found to possess ferromagnetism, provided that it possesses structural defects[261] or due to interaction with surface entities such as thiols[262]. For this investigation the catalyst particles are produced through a bottom-up procedure utilising a biological matrix to assist in nanoparticle formation via dual enzymatic and scaffolding functions. This method was shown to produce palladium nanoparticles with a highly strained structure, which can lead to a ferromagnetic state being achieved (Chapter 6). Hence, nanoscale 'bio-Pd' is suitable for investigation into oxygen enrichment. However, Pt has been shown to be a superior catalyst for the oxygen reduction reaction and can become ferromagnetic in a similar way to nanoscale Pd[262], thus the focus of this work is 'bio-Pt' . This approach has the benefit that it would not require any additional magnetic materials and that the magnetic field would be strongest at the catalyst, rather than near it as in the case of previous investigations. Also, the field would be non-uniform at the nanoscale, originating from the Pt nanoparticles.

7.2 Methods and Materials

7.2.1 Manufacture of Platinum Nanoparticles

Escherichia coli bacteria were used for nanoparticle production; cells were grown as described previously (Chapter 3), washed three times in 20 mM 4-morpholinepropanesulfonic acid (MOPS)/NaOH buffer (Sigma) at pH 7.0, and stored under oxygen free nitrogen (OFN, BOC) overnight at 4 °C (40 mg dry weight/ml) in a small volume of the same buffer, by reference to a previously determined OD_{600}/dry weight conversion. A

solution of 2 mM K_2PtCl_6 (99.9%, Aldrich) in 0.01 M HNO_3 was degassed, placed under OFN, and heated to 37 °C. *E.coli* was added to achieve a respective mass of solids of 5 % Pt and 95 % biomass (w/w) (30 min, 37 °C with occasional shaking) for Pt-biosorption, after which hydrogen was sparged through (30 min) before pressurising at 1 bar (37 °C; 180 rpm; 2 days). Bio-Pt was harvested centrifugally, with metal removal checked by analysis of the supernatant[263]. As the presence of residual biomass inhibits electrochemical catalysis of the ORR in acidic media; cleaning of the catalyst using NaOH was done as reported previously (Chapter 5). An ink containing commercial Tanaka Kikinzoku Kogyo (TKK) TEC10E50E (45.9 % Pt on C) platinum catalyst, prepared as described previously (Chapter 5), was used as a control.

Whilst *Desulfovibrio desulfuricans* has been shown to produce superior bio-Pt fuel cell catalyst than that of *E.coli*, this work has used *E.coli*. The justification for this is that *E.coli* is a better understood species of bacteria and is thus used as the 'laboratory workhorse' as well as in many industrial applications. As such it is much more likely that waste *E.coli* could be sourced than waste *D.desulfuricans*, which is important if the goal is for optimal economy. Furthermore the cleaning processes involved to achieve a suitable electrochemical surface are more environmentally harmful in the case of *D.desulfuricans* as it requires the useful of phenol, chloroform and NaOH rather than NaOH and HCl as is the case for *E.coli*.

7.2.2 Physical Characterisation of Bio-Pt Samples

Magnetic testing used a superconducting quantum interference device (SQUID) magnetometer (MPMS, Quantum Design, USA). The bio-Pt samples were dried before analysis by washing three times in distilled water and once in acetone, then drying overnight in air. Samples were ground using an agate pestle and mortar and placed into a gelatine capsule for measurement. Testing was carried out between ±3000 Oe. Measurements were normalised to 1 g of platinum. SQUID measurements were made prior to cleaning.

Inductively coupled plasma mass spectrometry (ICP-MS) was used to ascertain the Pt (measured at mass 195, detection limit 0.005 ppb) present in the samples post cleaning using an Agilent 7500ce ICP-MS with an octopole reaction system (ORS) to remove polyatomic interferences. The plasma runs with an RF power of 1500 W. A Miramist nebuliser was used for sample introduction. For analysis, a small volume of the sample was suspended in freshly prepared aqua regia (2 days). The Pt-solution was diluted to 0.07 % HNO_3 / 0.11 % HCl for ICP-MS analysis.

7.2.3 Magnetisation of Samples

Catalytic testing was carried out electrochemically. The sample was magnetised by loading wet sample onto a glassy carbon (GC) working electrode whilst exposed to an external magnetic field. This field was provided by a pair of neodymium countersunk cylindrical magnets (25 mm diameter x 20 mm thick with 6 mm hole; first4magnets, UK), aligned such that the north pole of one was facing the south pole of the other (Figure 7.1a) to produce a

near uniform field between them (≈ 0.25 T). The magnets were fixed to an aluminium frame to ensure that the field was fixed over each sample preparation and between samples. Sample loading was carried out either without exposure to the magnetic field, or with the plane of the GC electrode either parallel or perpendicular to the magnetic field(Figure 7.1b). Samples remained exposed to the appropriate magnetic field until the sample had dried (approx. 30 min). Commercial catalyst, Tanaka Kikinzoku Kogyo (TKK) TEC10E50E (45.9% Pt on C), was used as a control.

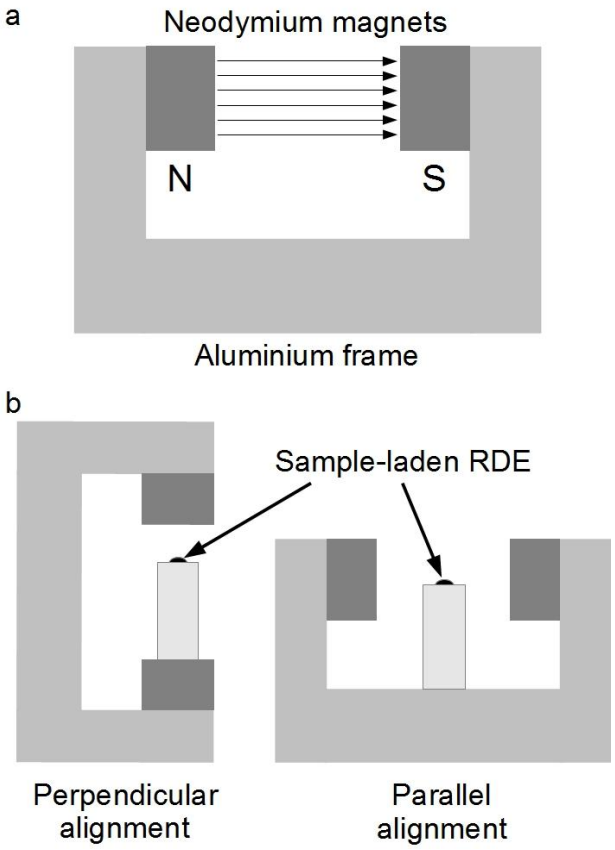

Figure 7.1, magnetic set up used for pre-magnetisation of samples prior to electrochemical analysis. a shows the basic set up with some magnetic field lines between magnets indicated, b shows the wet sample on the rotating disc electrode (RDE) in the perpendicular and parallel magnetisation arrangements.

7.2.4 Electrochemical Analysis

Electrochemical measurements were conducted at 298 K, which was maintained using a heated water bath and a pump, connected to a jacket around the electrochemical cell. A three electrode arrangement was used, where the working electrode was the sample-laden GC electrode, the counter electrode a Pt mesh and the reference a leakless Ag/AgCl reference electrode (eDaq). An Autolab PGSTAT302N potentiostat operated using Nova 1.10 (Metrohm) was used for experimental control. For linear sweep measurements a rotator was used (Origalys). The electrolyte was 0.1 M $HClO_4$, prepared from 70 % (AR, Fisher) which was sparged with OFN, compressed dried and filtered air or O_2 (99.999 %, BOC Special Gases) (at least 20 min) before data acquisition.

Cyclic voltammetry (CV) data was obtained in oxygen depleted electrolyte (pre-sparged with OFN). Linear sweeps were done using each atmosphere, with the nitrogen sweep being subtracted from the air and oxygen sweeps to remove the background.

7.3 Results and Discussion

A non-magnetised preparation allows the magnetic fields within the sample to possess random alignment and therefore they have no net orientation. The magnetic fields within the sample would align with the magnetic field applied during preparation for the ‘parallel’ and ‘perpendicular’ preparations. The field of the sample which was prepared perpendicular to the plane of the GC electrode would extend into the bulk of the electrolyte during testing and might be expected to enrich the oxygen present towards it (see 6.1). The parallel aligned

sample would have field extending across the near-surface region of the electrolyte and thus could be expected to lead to the accumulation of very little additional oxygen.

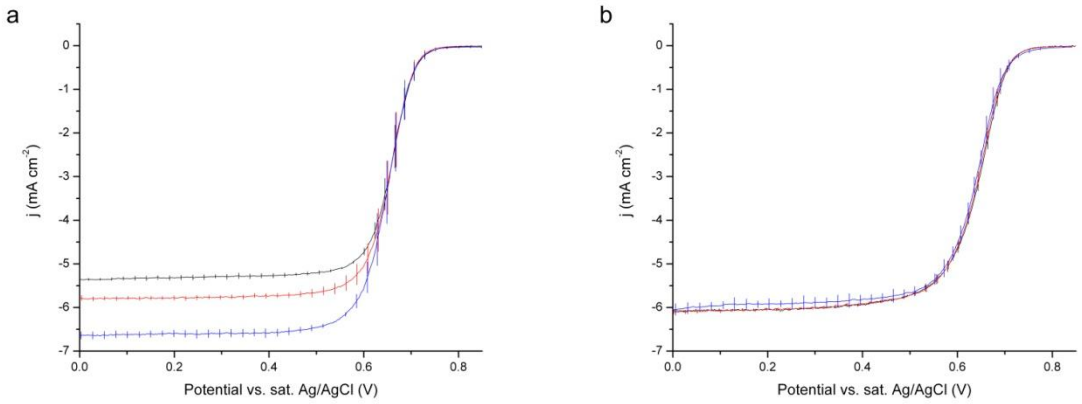

Figure 7.2, linear sweep voltammograms of cleaned bio-Pt (a), TKK (b) at 1600 rpm. Non-magnetised, black line; magnetised parallel to GC disc, red line; magnetised perpendicular to GC disc, blue line. Error bars represent standard error.

Placing the TKK reference material into the magnetic field had no effect, within error, on its electrochemical behaviour (Figure 7.2b). The non-magnetised bio-Pt sample performed similarly to the bio-Pt which was prepared using *E.coli* and NaOH cleaning reported previously (Chapter 5). Hence, oxygen reduction data reveals that the magnetised and non-magnetised measurements show differences for bio-Pt but not for TKK. The bio-Pt sample shows a major improvement in the diffusion limited current obtained from the perpendicularly aligned magnetised sample versus the non-magnetised sample (Figure 7.2a), i.e. pre-magnetisation has a strong effect on the limiting current. Optimal pre-magnetisation shows an increase of 24 %, which approaches the value of 27 % reported by

Okada *et al.* (2003)[257] for a cathode prepared with Nd-Fe-B particles mixed into the catalyst layer.

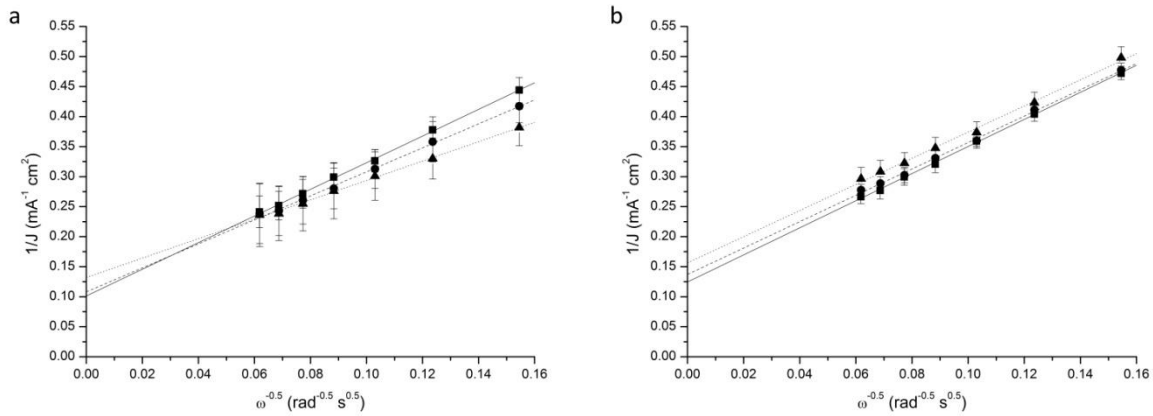

Figure 7.3, Koutecký Levich plots at 0.64 V vs. Ag/AgCl of cleaned bio-Pt (a), TKK (b) at 1600 rpm. Non-magnetised (solid line, ■); magnetised parallel to GC disc (dashed line, ●); magnetised perpendicular to GC disc (dotted line, ▲). Error bars represent standard error.

Half-wave potential values were unchanged, within error, through the magnetic treatment of the samples (Figure 7.2). Koutecký-Levich analysis (Figure 7.3) shows no trend resulting from the introduction of magnetism beyond the change to the value of the slope, which was absent from the TKK sample, either indicating an alteration to the number of electrons transferred in the reaction, or an alteration to the diffusion coefficient when the bio-Pt sample is magnetised. Tafel analysis (Figure 7.4) maintains the expected ~60 mV/decade for each sample regardless of magnetic treatment, showing that the rate limiting step is the expected two electron transfer. As the rate limiting step behaves as expected it is surmised that the reaction processes are unaffected by the introduction of magnetism and that the alteration to the Koutecký-Levich slope is attributable to an enhanced diffusion coefficient

resulting from the magnetic enrichment of oxygen at the catalyst in a similar way to the earlier conclusions of Shi *et al.* (2013)[264], but with no 'dilution' with electrochemically non-contributing metal.

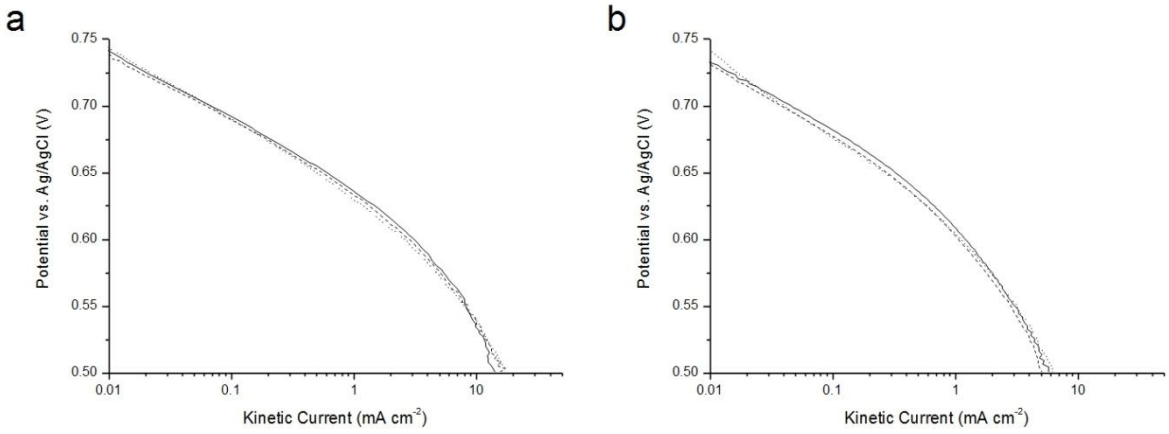

Figure 7.4, Tafel plots at 1600 rpm of cleaned bio-Pt (a), and TKK (b) at 1600 rpm. Non-magnetic, solid line; magnetised parallel to GC disc, dashed line; magnetised perpendicular to GC disc, dotted line.

The diffusion limited current is a value that can be determined from the Levich equation (Equation 7.4). The values in this equation are constants, are determined by the reaction (n) or the materials (D_O and *v*), or are experimentally controlled values (A, ω and C_O^*).

$$i_{lim} = 0.62nFAD_O^{2/3}\omega^{1/2}\nu^{-1/6}C_O^* \quad (7.4)$$

where i_{lim} is the limiting current, n is the number of electrons transferred in the half reaction, F is the Faraday constant, A is the electrode area, D_O is the diffusion coefficient, ω is the electrode rotation rate (radians per second), *v* is the kinematic viscosity and C_O^* is the bulk analyte concentration.

As the controlled parameters were constant and the reaction at the catalyst is expected to be unaffected (supported by the rate limiting step remaining unchanged, Figure 7.4) and kinematic viscosity is determined by the electrolyte, which was unchanged, the improvements in observed current therefore can be expected to indicate improved diffusion of oxygen. Previous experiments following the cleaning of bio-Pt with NaOH indicated that there was a small residual hindrance to the diffusion of oxygen (Chapter 5) which is also present here, yet when the sample was optimally magnetised the 24 % increase in performance allowed it to surpass what would be expected by the Levich equation (using the typical value for the oxygen diffusion coefficient in water at 25 °C) by more than 7 %, attributed to the effect of oxygen enrichment (Figure 7.5). Parallel magnetisation showed a slight improvement over a non-magnetised sample however it is possible that this has arisen due to slight non-linearities in the applied field generated by the external neodymium magnet during sample preparation. The TKK sample shows no indication that a magnetisation step in the sample loading phase of preparation produces this effect, which was expected as it showed near zero response during magnetic analysis.

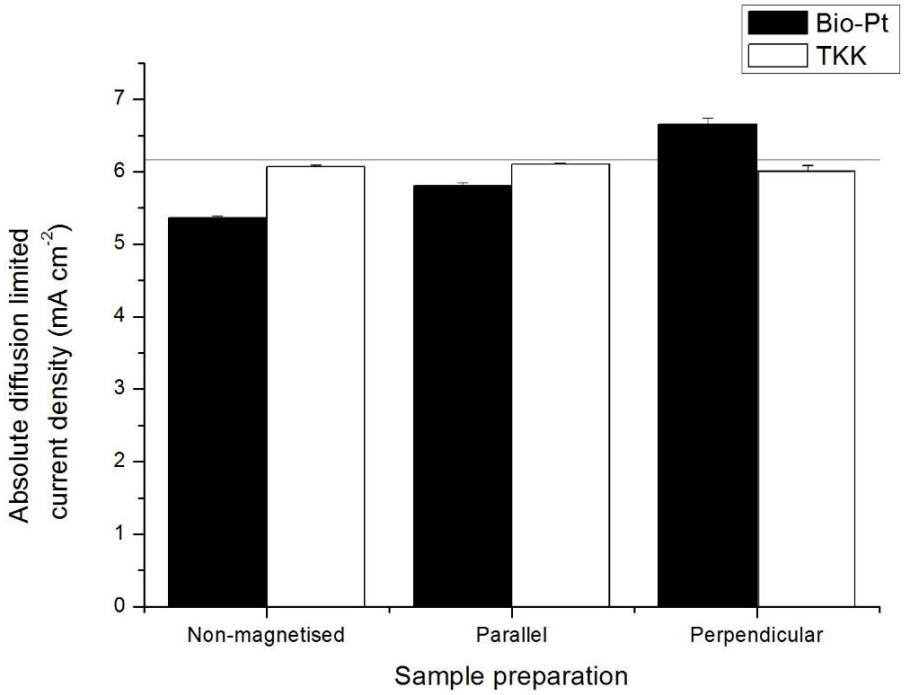

Figure 7.5, impact of sample preparation method upon the diffusion limited current. Levich theory value shown as solid line. Error bars represent standard error.

Magnetic testing of dried samples gives information about the remanent field and the coercivity. The remanence is particularly important as this is the magnetism remaining when there is no external applied field, as was the case for the electrochemical experiments reported here. The coercivity describes the strength of an opposing magnetic field which will demagnetise the sample.

Figure 7.6 shows that TKK possesses extremely weak magnetism, which was expected from the electrochemical results since these showed no change with magnetic preparation procedure. The bio-Pt sample possesses superparamagnetism shown by the rapid alignment of moment with applied field, with the weak coercivity ~10 Oe possibly arising due to the larger particles being in a blocked state[265], or long range interaction between nanoparticles

in close proximity to each other[228]. The maximum remanence measured here for the bio-Pt sample is more than an order of magnitude below the level that Shi *et al.* (2013)[259] found to be effective in their study investigating the effect of magnetism on oxygen diffusion in zinc-air fuel cells and 3 orders of magnitude lower than that of Okada *et al.* (2003)[257] reported in their study on PEFCs. With a large discrepancy between the magnetism measured here and that reported by other authors, it is likely that the magnetic measurements shown in Figure 7.6 (using native, dried bio-Pt) are not representative of the magnetism present during the electrochemical testing (using NaOH 'cleaned' samples) where the bulk of the non-conductive biomass component had been removed (Chapter 5).

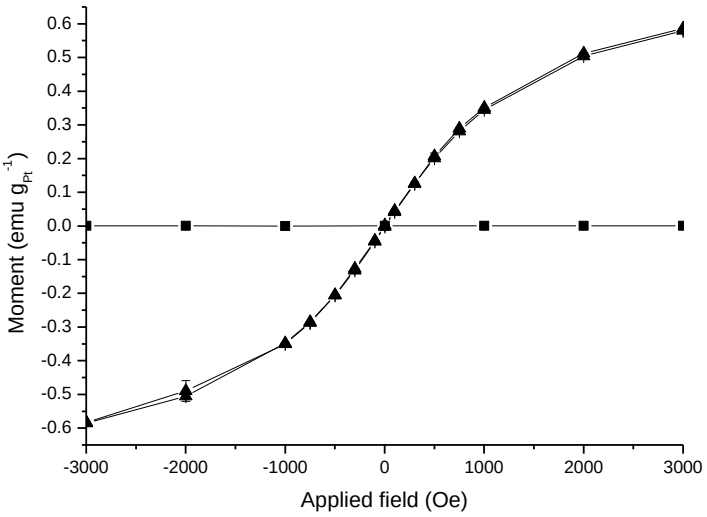

Figure 7.6, moment against applied field, normalised per gram of Pt. Bio-Pt (▲); TKK (■).

Chapter 6 has shown that in a similar biologically supported palladium system, a ferromagnetic component originates from clusters of nanoparticles rather than from individual nanoparticles, which are superparamagnetic. Figure 7.6 indicates that the bio-

catalyst samples possess superparamagnetism, as evidenced by the non-linearity in the moment against applied field, yet very little ferromagnetism, as evidenced by the minimal hysteresis. The small quantities of Pt precluded magnetic measurements after the sacrificial cleaning process, therefore it was necessary to conduct the magnetic measurements shown in Figure 7.6 beforehand. The cleaning procedure used here removes much of the biomatrix, thus causing the nanoparticles to reside within much closer proximity to each other[169], and in turn this increased proximity would cause the magnetic moments of the superparamagnetic nanoparticles to be capable of interaction with each other, leading to the possible occurrence of superferromagnetism to arise within the sample[228]. Thus the permanent magnetism in the magnetised cleaned sample can be expected to be of greater magnitude than is indicated by the measurements in Figure 7.6; explaining the discrepancy between the effect of the magnetism used in this study compared to that of Okada *et al.* (2003)[257] and Shi *et al.* (2013)[259].

7.4 Conclusion

The effect of magnetic fields has been shown by several authors to improve the power output of hydrogen fuel cells due to their ability to enrich oxygen in the catalyst layer whilst simultaneously inhibiting the diffusion of nitrogen and expelling the water produced by the reaction. These typically have involved the addition of rare earth magnetic particles into the catalyst layer. We show that this can be achieved in a facile, non 'diluting' way by using a

novel magnetic electrocatalyst whereby biomanufacturing provides magnetically active Pt nanomaterial for this purpose.

The magnetic measurements shown here do not allow for direct quantitative analysis of the interaction between increased magnetic field strength and the impact upon the electrochemical reaction. However, we can conclude that the bio-Pt sample shows a greater magnetic response during magnetic analysis and this sample also imparts a significant improvement in O_2 diffusion when magnetised.

Whilst the strength of the magnetism during catalytic analysis was not accurately determined, this work concurs with the findings of other authors, in that a magnetised catalyst can provide an improvement in oxygen diffusion and provides the first step towards improved fuel cell catalysts via biofabrication. To our knowledge biofabrication provides the first report of a combined magnetically and electrochemically active, ‘undiluted’ Pt catalyst for the oxygen reduction reaction.

8. SUMMARY AND FURTHER WORK

8.1 Summary

There are a wide range of variables that can be used to alter the size and structure of metal nanoparticles prepared via biofabrication. An investigation was conducted to more thoroughly investigate a small number of these to determine the effect that they had upon fabrication of platinum nanoparticles. Amongst these, the largest difference was observed when using different reducing agents. Hydrogen-based reduction produced larger nanoparticles that tended to be located near the cell surface, whereas formate-based reduction produced smaller nanoparticles distributed relatively evenly throughout the entire cell. In addition, XPS provided indication that the use of a different reducing agent causes different organic groups to interact with the platinum. It was also determined that a long biosorption time was found to increase the variability of nanoparticles produced due to increasing the preference for large cluster formation on certain, presumably heavily seeded, biosorption sites on a small number of bacterial cells and that increased metal loading led to larger cluster formation. Hydrogen-based reduction was viewed as preferable for the preceding studies as the tendency to form nanoparticles near the cell surface suggested that there was the possibility of use for direct application as a fuel cell catalyst due to possessing much less obstructing biomass inhibiting access to the catalyst. Furthermore, it was also possible that, should the biomass need to be partially removed, it could be done so more easily than with a formate-based reduction.

Ultimately it was discovered that for an electrochemical catalyst application, it was necessary that bio-Pt needed to undergo a thorough removal of biomass, as the most thorough 'cleaning' procedures were determined to produce a catalyst possessing vastly superior effectiveness than 'softer' cleaning procedures. As such, it is possible that the use of a formate-based reduction may ultimately be capable of producing a superior catalyst as the need to remove almost all biomass would be necessary for bio-Pt prepared using either reducing agent, and the smaller size of bio-Pt prepared with a formate-based reduction could be expected to possess superior mass activity due to the increased surface area.

Internal magnetic testing of bio-Pd was done to provide additional information about its magnetic properties. This was done to attempt to gain an increased understanding of the origins of the magnetism for bio-Pd and, by extension, bio-Pt. This showed a complex situation with multiple magnetic types being observed within the bio-Pd, however comparison with electron micrographs allowed for the observation of a structural relationship which suggested that the magnetism was occurring due to clusters of superparamagnetic nanoparticles behaving as a superferromagnet.

When tested as an electrocatalyst, optimally magnetised bio-Pt was observed to provide a significant enhancement to the diffusion limited current for the oxygen reduction reaction; with the observed enhancement probably resulting from increased oxygen diffusion. As the magnetic testing of native bio-Pt showed magnetic properties that were likely too weak to achieve the observed degree of enhancement this provides additional indication of a relationship between nanoparticle clusters and ferromagnetism, however due to the small quantities of cleaned bio-Pt it was not possible to obtain confirmation of this.

8.2 Further work

Whilst this project has shown that it is possible to produce a Pt nanoparticulate electrocatalyst through biofabrication that is capable of enhanced oxygen reductive current due to its magnetic properties, it has left some avenues open for further research.

1. Preparation of a larger batch of magnetic bio-Pt could allow for magnetic measurements to be made before and after cleaning to determine if nanoparticle clustering provides greater ferromagnetism.
2. Preparation of bio-Pt on *E.coli* using a different set of conditions, e.g. a formate-based reduction, to investigate if this would allow for *E.coli*-based nanoparticles to produce electrocatalytic results in line with those measured with the smaller Pt nanoparticles that were produced when *D.desulfuricans* was used for biofabrication.
3. Preparation of catalyst with base metal incorporated into the structure. Other authors have found alloys capable of producing a superior electrocatalyst, however it is also possible that the use of a ferromagnetic metal could provide additional improvement if the catalyst were properly magnetised prior to use. An attempt was made to produce a bio-PtNi catalyst for such an investigation (Appendix V), however it was not possible to successfully produce this in the time available in this study as the cleaned catalyst contained no Ni, as determined by ICP-MS.

APPENDICES AND REFERENCES

Appendix I – Biomass Growth Curves

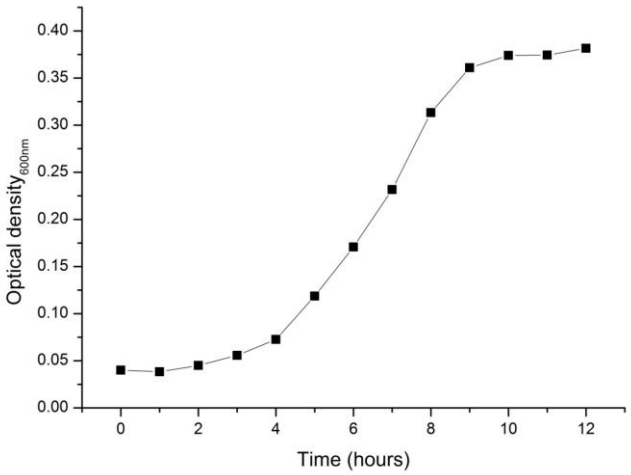

Figure A-I 1, optical density of E. coli *over time. Data obtained from three samples, standard error bars are within data point markers.*

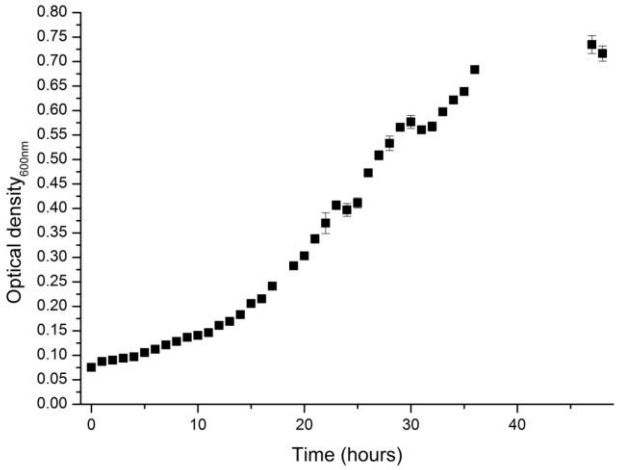

Figure A-I 2, optical density of D. desulfuricans *over time. Error bars shown standard error of three repeats.*

Appendix II – Biosorption Test

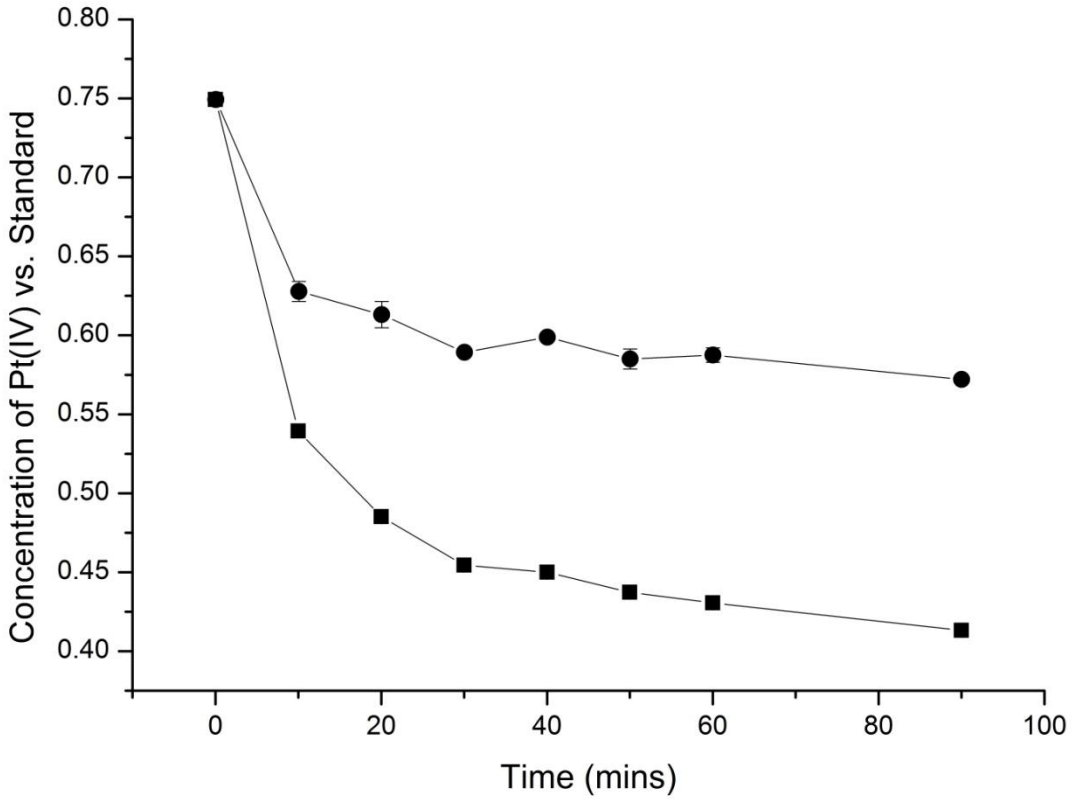

Figure A-II 1, effect of biosorption upon the free Pt(IV) concentration over time by tin chloride assay[23]. 5% loading (▪) and 10% loading (●). Error bars show standard error.

Appendix III – X-ray Photoelectron Spectra of Bio-Pt on *E.coli*

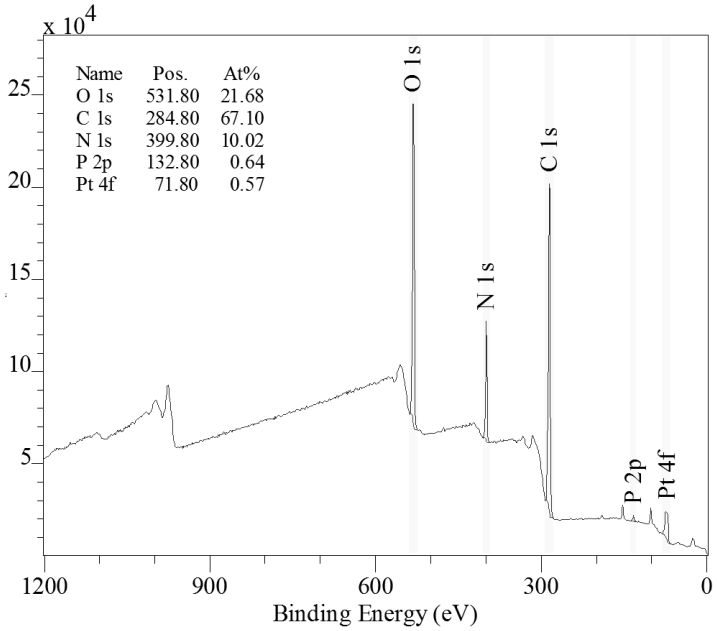

Figure A-III 1, XPS survey scan of sample 1 (10 % Pt, 30 minute biosorption, hydrogen reduced).

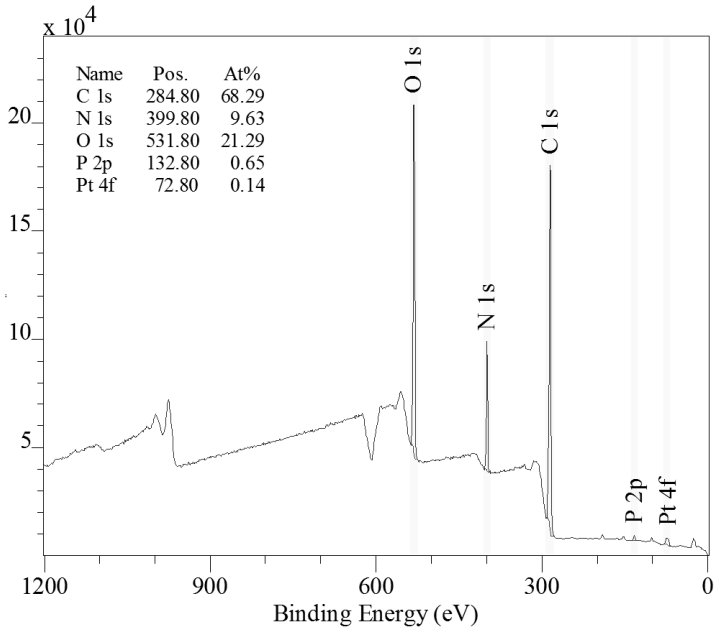

Figure A-III 2, XPS survey scan of sample 2 (5 % Pt, 30 minute biosorption, hydrogen reduced).

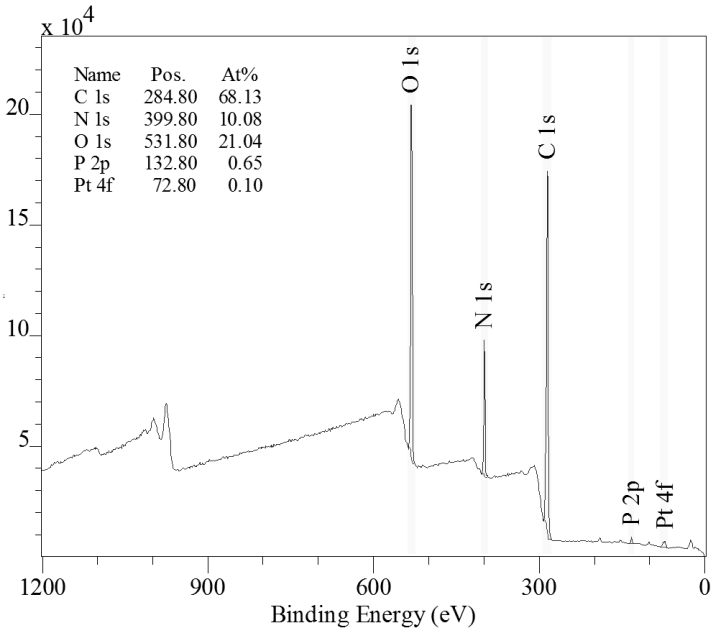

Figure A-III 3, XPS survey scan of sample 3 (5 % Pt, 60 minute biosorption, hydrogen reduced).

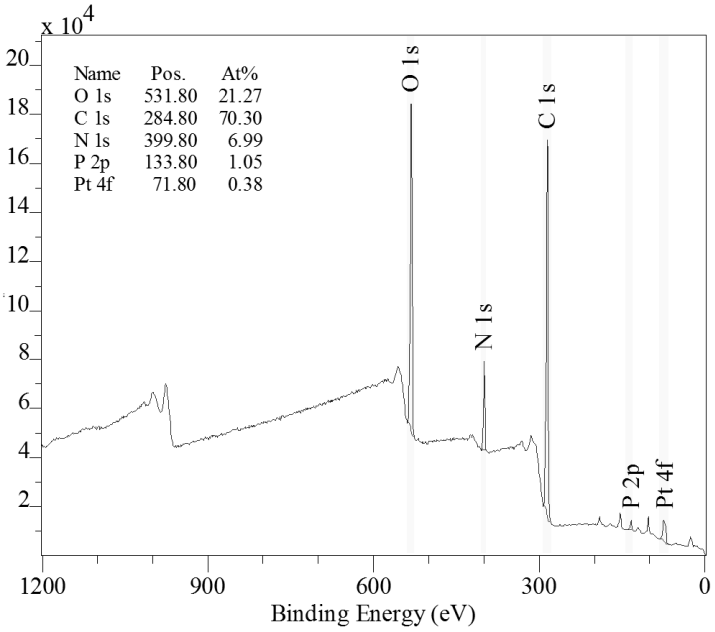

Figure A-III 4, XPS survey scan of sample 4 (10 % Pt, 30 minute biosorption, formate reduced).

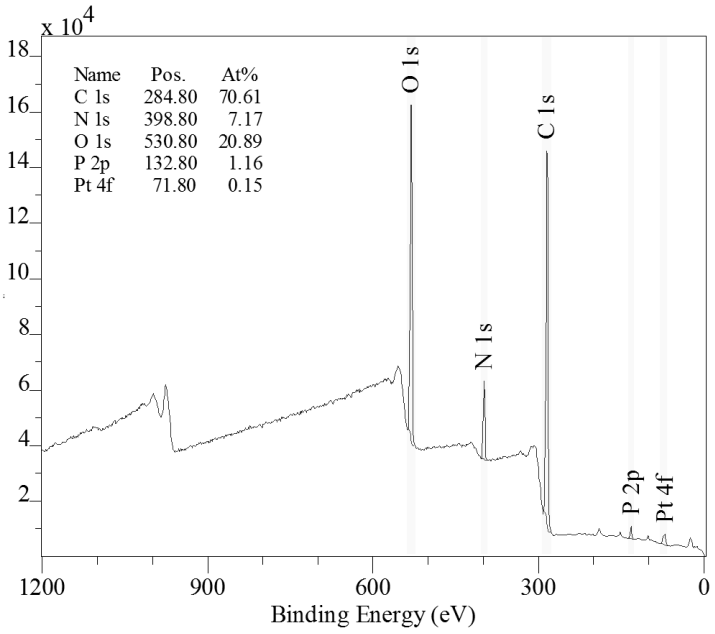

Figure A-III 5, XPS survey scan of sample 5 (5 % Pt, 30 minute biosorption, formate reduced).

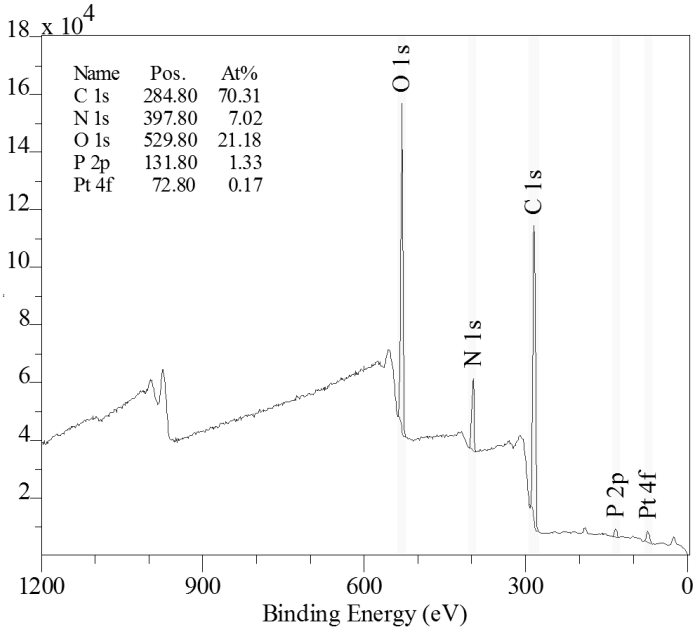

Figure A-III 6, XPS survey scan of sample 6 (5 % Pt, 60 minute biosorption, formate reduced).

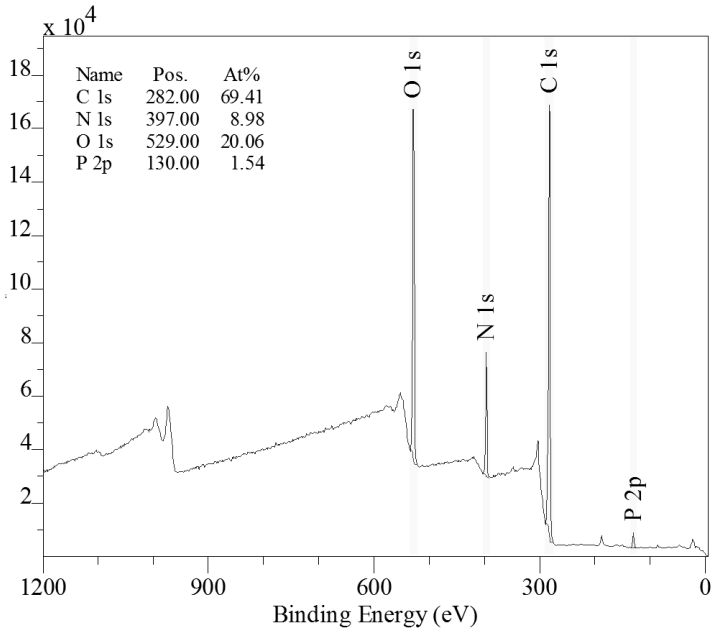

Figure A-III 7, XPS survey scan of sample 7 (Pt-free control).

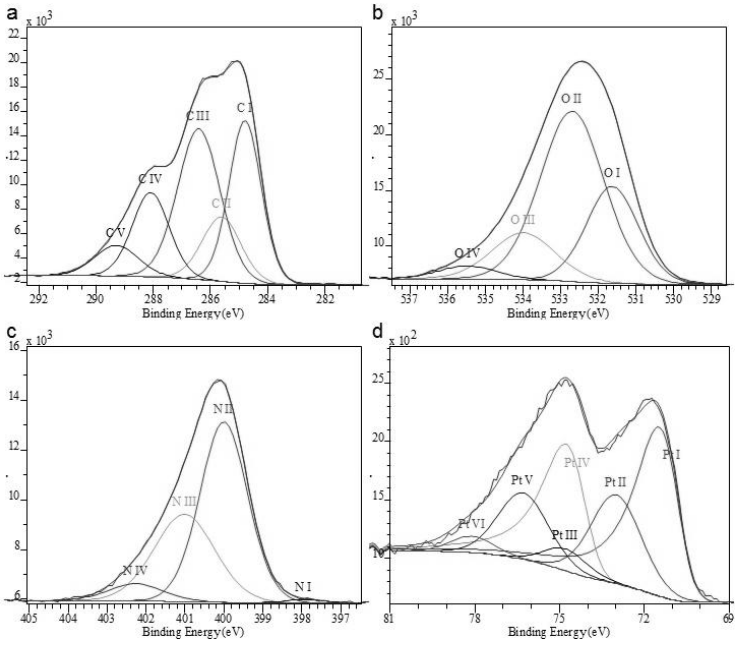

Figure A-III 8, XPS high resolution scans of sample 1. a is carbon 1s, b is oxygen 1s, c is nitrogen 1s and d is Pt 4f.

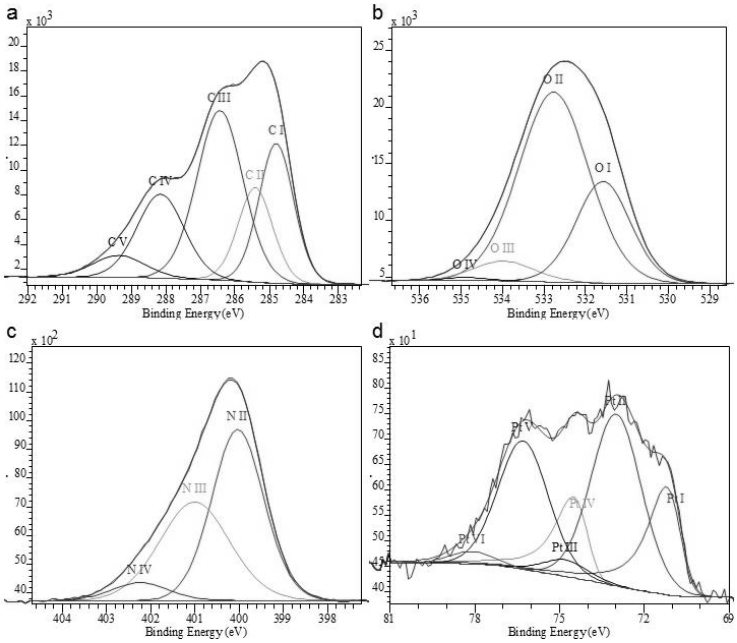

Figure A-III 9, XPS high resolution scans of sample 2. a is carbon 1s, b is oxygen 1s, c is nitrogen 1s and d is Pt 4f.

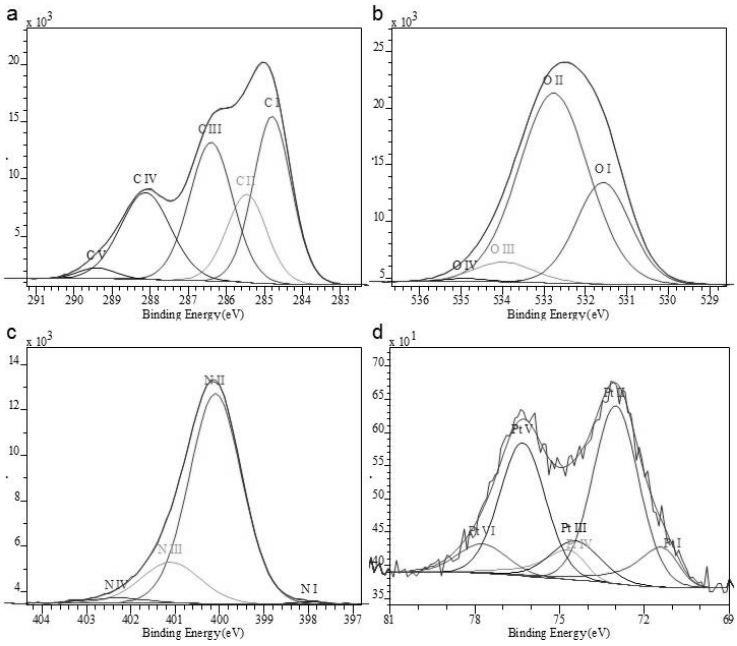

Figure A-III 10, XPS high resolution scans of sample 3. a is carbon 1s, b is oxygen 1s, c is nitrogen 1s and d is Pt 4f.

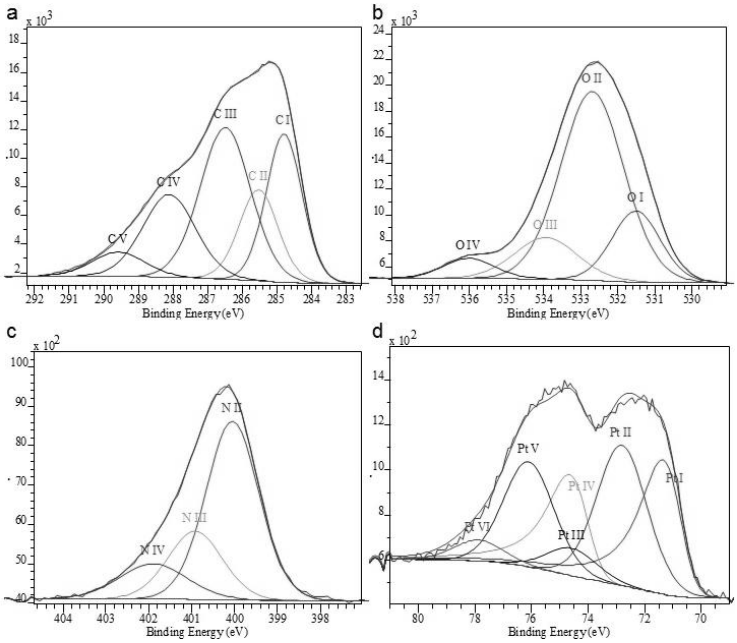

Figure A-III 11, XPS high resolution scans of sample 4. a is carbon 1s, b is oxygen 1s, c is nitrogen 1s and d is Pt 4f.

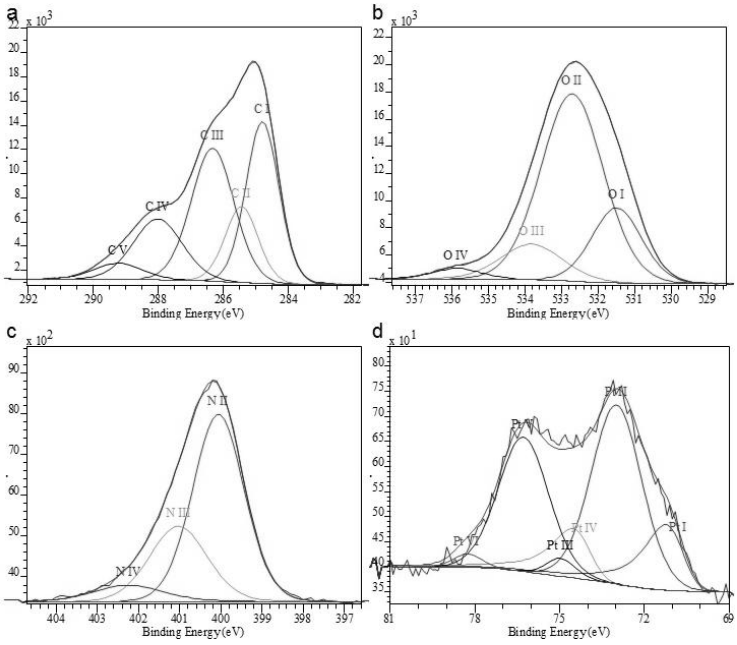

Figure A-III 12, XPS high resolution scans of sample 5. a is carbon 1s, b is oxygen 1s, c is nitrogen 1s and d is Pt 4f.

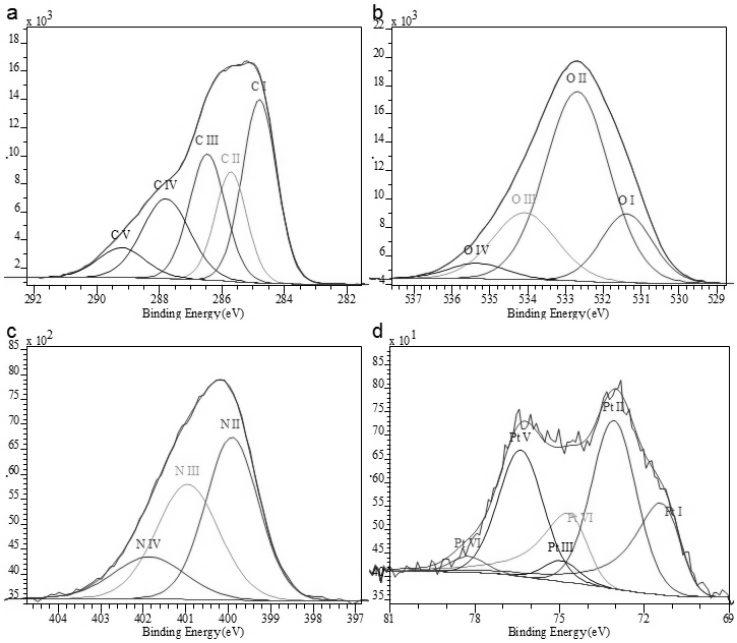

Figure A-III 13, XPS high resolution scans of sample 6. a is carbon 1s, b is oxygen 1s, c is nitrogen 1s and d is Pt 4f.

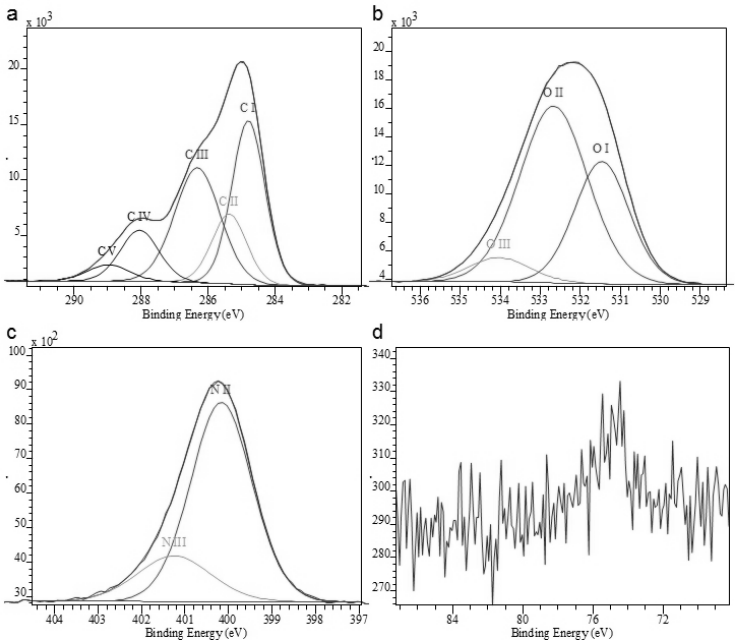

Figure A-III 14, XPS high resolution scans of sample 7. a is carbon 1s, b is oxygen 1s, c is nitrogen 1s and d is Pt 4f.

Appendix IV – Loading Tests for Electrochemical Experiments

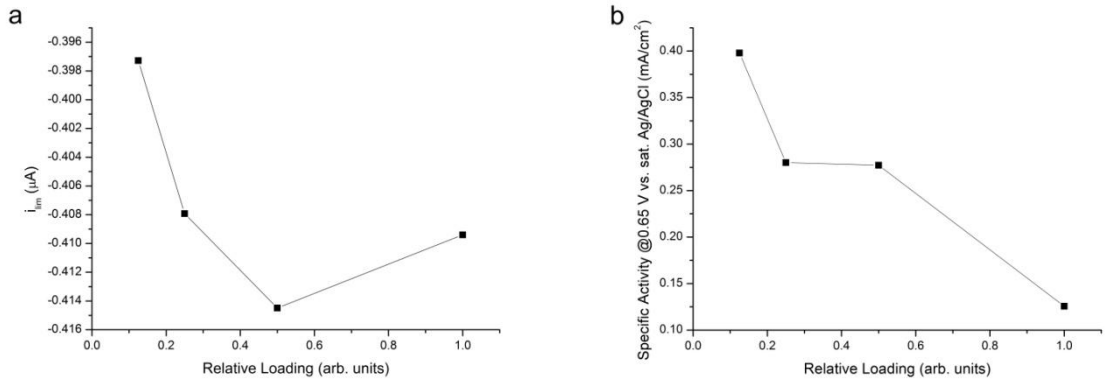

Figure A-IV 1, loading tests for phenol-chloroform cleaned Dd-Pt. Plots show the relative loading against diffusion limited current (a) and specific activity at 0.65 V vs. sat. Ag/AgCl (b). Highest loading tested results in decreased diffusion limited current likely due to the increased quantity of organic material present hindering diffusion.

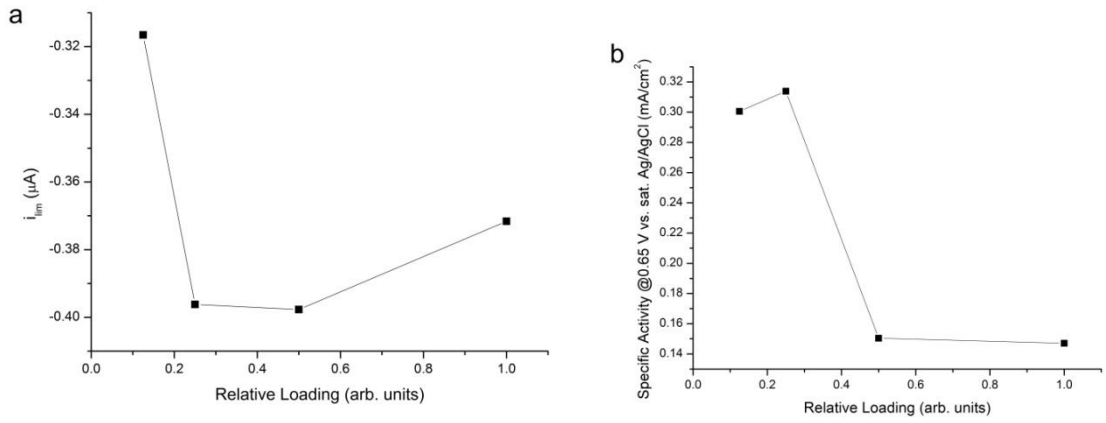

Figure A-IV 2, loading tests for NaOH cleaned Ec-Pt. Plots show the relative loading against diffusion limited current (a) and specific activity at 0.65 V vs. sat. Ag/AgCl (b). Highest loading tested results in decreased diffusion limited current likely due to the increased quantity of organic material present hindering diffusion.

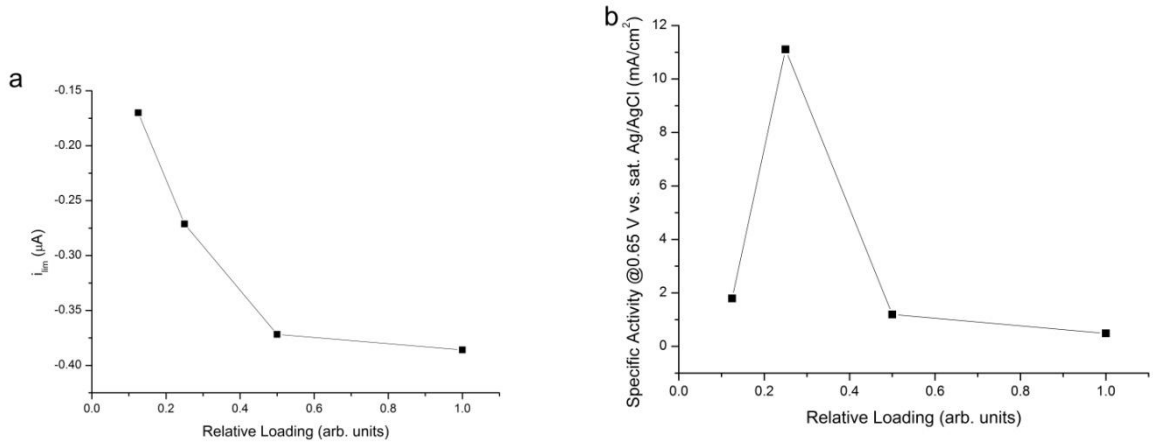

Figure A-IV 3, loading tests for water washed Ec-Pt. Plots show the relative loading against diffusion limited current (a) and specific activity at 0.65 V vs. sat. Ag/AgCl (b). The difficulty in accurately measuring the very low electrochemical surface area leads to a spurious extremely high value in b.

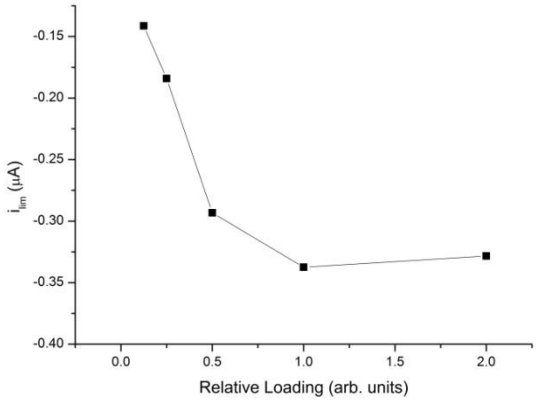

Figure A-IV 4, loading test for sintered Ec-Pt. Plot shows the relative loading against diffusion limited current. A specific activity vs. relative loading plot was not possible due to the difficulty in accurately measuring the very low electrochemical surface area.

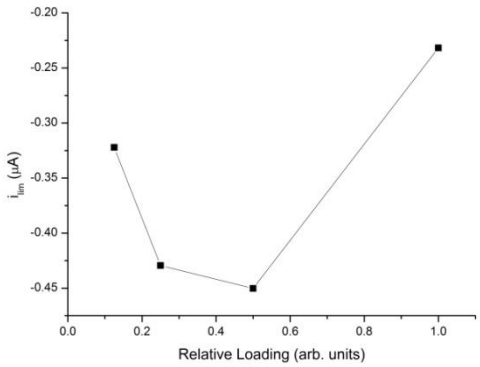

Figure A-IV 5, loading test for water refluxed Ec-Pt. Plot shows the relative loading against diffusion limited current. A specific activity vs. relative loading plot was not possible due to the difficulty in accurately measuring the very low electrochemical surface area. Highest loading tested results in decreased diffusion limited current likely due to the increased quantity of organic material present hindering diffusion.

Appendix V – Bimetallic Magnetic Nanoparticles

A-V.1 Introduction

It has been shown previously (Chapter 6) that biofabrication can produce nanoparticles which possess permanent magnetism that can be utilised to improve oxygen diffusion. It has also been shown that oxygen diffusion increases with increasing permanent magnetic field strength[257]. To investigate further, Pt/Ni bimetallic nanoparticles were prepared by a similar procedure to the magnetic bio-Pt.

A-V.2 Methods and Materials

Biomass was grown as described previously (Chapter 3). The biosorption procedure used a quantity of 2 mM K_2PtCl_6 which would yield a 5 % (w/w %) Pt loading on biomass. Prior to reduction a mixture of 2 mM K_2PtCl_6 and 2 mM $NiCl_2.6H_2O$ (99.9 %, Aldrich) was added such that the final mass of solids would be 15 % Pt, 5 % Ni and 80 % biomass. Reduction was done by sparging of hydrogen (30 min) then pressurising at 1 bar (37 °C; 180 rpm; 2 days). Bio-Pt/Ni was harvested centrifugally, with metal removal checked by analysis of the supernatant[263]. This is a greater metal loading than the previous magnetic bio-Pt study, and was used as prior investigation had shown that a 5 % total metal loading of Pt and Ni led to a pale pink final colour, suggesting that a red compound had formed between the nickel and the organic material[266,267]. Following reduction NaOH cleaning was done as described previously (Chapter 5).

The electrochemical set up was the same as described previously (Chapter 7). Magnetisation was done as described previously (Chapter 7). Inductively coupled plasma mass spectrometry (ICP-MS) was used to ascertain the Pt (measured at mass 195, detection limit 0.005 ppb) and Ni (measured at mass 60, detection limit 0.02 ppb) present in the samples, post cleaning, using an Agilent 7500ce ICP-MS with an octopole reaction system (ORS) to remove polyatomic interferences. The plasma runs with an RF power of 1500 W. A Miramist nebuliser was used for sample introduction. For analysis, a small volume of the sample was suspended in freshly prepared aqua regia (2 days). The metal solution was diluted to 0.07 % HNO_3 / 0.11 % HCl for ICP-MS analysis.

A-V.3 Results and Discussion

Non-magnetised oxygen reduction testing showed that the diffusion limited current was superior to the value obtained with non-magnetised bio-Pt in the previous study (Figure A-VI 1). However, the benefit of magnetisation is less than was observed previously with bio-Pt. As the metal loading on the biomass was greater for bio-Pt/Ni than the previous bio-Pt the nanoparticle size can be expected to be greater[35], thus the magnetism from the Pt would be expected to be poorer[268], yet the presence of Ni should provide a greater improvement to the magnetisation[269].

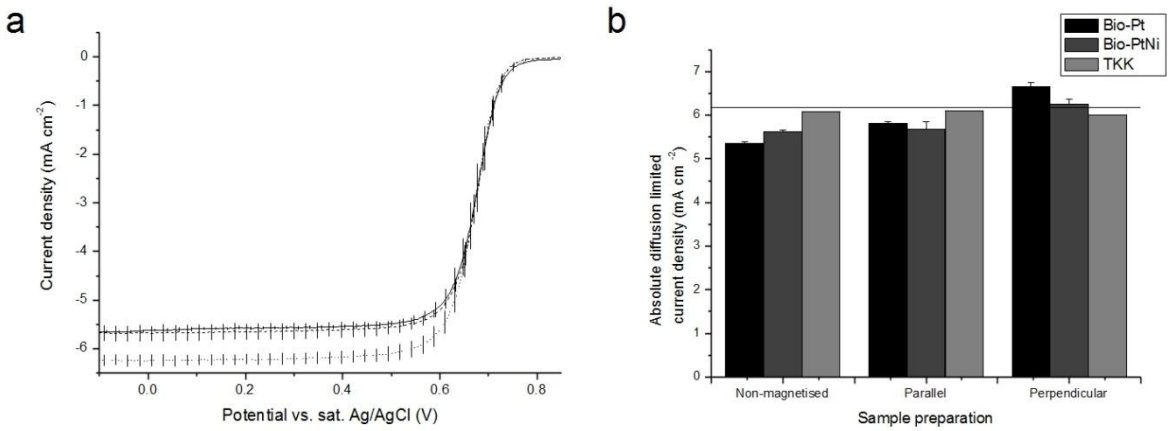

Figure A-V 1, diffusion limited current measurements; a, 1600 rpm linear sweep voltammograms for bio-PtNi; b, comparison of diffusion limited current measurements against previous observations.

Mass spectroscopy analysis revealed that the bio-Pt/Ni sample did not possess appreciable quantities of Ni (<1 % of metal content). As UV-Vis measurements indicated that the Ni was removed from the solution following exposure to the biomass and H_2, the lack of Ni in the cleaned sample has occurred due to either a failure to be reduced by hydrogen or removed during cleaning, possibly as $Ni(OH)_4^{2-}$ in the liquid phase.

A-V.4 Conclusion

The addition of nickel into the catalyst biofabrication procedure was done with the goal of enhancing the permanent magnetism. This methodology was not able to produce a 'cleaned' bio-Pt/Ni catalyst. However, it is possible that a different reducing agent and/or

cleaning process may be capable of achieving this goal, which would have an impact upon the nanoparticle formation and possibly their catalytic capability[7].

List of References

1 Narayanan, K. B. & Sakthivel, N. Biological synthesis of metal nanoparticles by microbes. *Advances in Colloid and Interface Science* **156**, 1-13, (2010).

2 Mata, Y. N. *et al.* Gold(III) biosorption and bioreduction with the brown alga *Fucus vesiculosus*. *Journal of Hazardous Materials* **166**, 612-618, (2009).

3 Gadd, G. M. & White, C. Microbial treatment of metal pollution -- a working biotechnology? *Trends in Biotechnology* **11**, 353-359, (1993).

4 White, C., Wilkinson, S. C. & Gadd, G. M. The role of microorganisms in biosorption of toxic metals and radionuclides. *International Biodeterioration & Biodegradation* **35**, 17-40, (1995).

5 de Vargas, I., Macaskie, L. E. & Guibal, E. Biosorption of palladium and platinum by sulfate-reducing bacteria. *Journal of Chemical Technology & Biotechnology* **79**, 49-56, (2004).

6 Riddin, T. L., Govender, Y., Gericke, M. & Whiteley, C. G. Two different hydrogenase enzymes from sulphate-reducing bacteria are responsible for the bioreductive mechanism of platinum into nanoparticles. *Enzyme and Microbial Technology* **45**, 267-273, (2009).

7 Rashamuse, K. & Whiteley, C. Bioreduction of Pt (IV) from aqueous solution using sulphate-reducing bacteria. *Applied Microbiology and Biotechnology* **75**, 1429-1435, (2007).

8 Deplanche, K., Snape, T. J., Hazrati, S., Harrad, S. & Macaskie, L. E. Versatility of a new bioinorganic catalyst: Palladized cells of *Desulfovibrio desulfuricans* and application to dehalogenation of flame retardant materials. *Environmental Technology* **30**, 681-692, (2009).

9 Yong, P., Rowson, N. A., Farr, J. P. G., Harris, I. R. & Macaskie, L. E. Bioreduction and biocrystallization of palladium by *Desulfovibrio desulfuricans* NCIMB 8307. *Biotechnology and Bioengineering* **80**, 369-379, (2002).

10 Ahmad, A. *et al.* Enzyme Mediated Extracellular Synthesis of CdS Nanoparticles by the Fungus, *Fusarium oxysporum*. *Journal of the American Chemical Society* **124**, (2002).

11 Mukherjee, P. *et al.* Extracellular Synthesis of Gold Nanoparticles by the Fungus *Fusarium oxysporum*. *ChemBioChem* **3**, 461-463, (2002).

12 Xiao, Y. *et al.* Catalytic Growth of Au Nanoparticles by NAD(P)H Cofactors: Optical Sensors for $NAD(P)^{+}$-Dependent Biocatalyzed Transformations. *Angewandte Chemie* **116**, 4619-4622, (2004).

13 He, S. *et al.* Biosynthesis of gold nanoparticles using the bacteria *Rhodopseudomonas capsulata*. *Materials Letters* **61**, 3984-3987, (2007).

14 Riddin, T. L. & et al. Analysis of the inter- and extracellular formation of platinum nanoparticles by *Fusarium oxysporum* f. sp. *lycopersici* using response surface methodology. *Nanotechnology* **17**, 3482 (2006).

15 Konishi, Y. *et al.* Bioreductive deposition of platinum nanoparticles on the bacterium *Shewanella algae*. *Journal of Biotechnology* **128**, 648-653, (2007).

16 Mikheenko, I. P., Rousset, M., Dementin, S. & Macaskie, L. E. Bioaccumulation of Palladium by *Desulfovibrio fructosivorans* Wild-Type and Hydrogenase-Deficient Strains. *Appl. Environ. Microbiol.* **74**, 6144-6146, (2008).

17 Vinod, V. T. P., Saravanan, P., Sreedhar, B., Devi, D. K. & Sashidhar, R. B. A facile synthesis and characterization of Ag, Au and Pt nanoparticles using a natural hydrocolloid gum kondagogu (*Cochlospermum gossypium*). *Colloids and Surfaces B: Biointerfaces* **83**, 291-298, (2011).

18 Venu, R., Ramulu, T. S., Anandakumar, S., Rani, V. S. & Kim, C. G. Bio-directed synthesis of platinum nanoparticles using aqueous honey solutions and their catalytic applications. *Colloids and Surfaces A: Physicochemical and Engineering Aspects* **384**, 733-738, (2011).

19 Song, J., Kwon, E.-Y. & Kim, B. Biological synthesis of platinum nanoparticles using *Diopyros kaki* leaf extract. *Bioprocess and Biosystems Engineering* **33**, 159-164, (2010).

20 Govender, Y., Riddin, T., Gericke, M. & Whiteley, C. Bioreduction of platinum salts into nanoparticles: a mechanistic perspective. *Biotechnology Letters* **31**, 95-100, (2009).

21 Govender, Y., Riddin, T., Gericke, M. & Whiteley, C. On the enzymatic formation of platinum nanoparticles. *Journal of Nanoparticle Research* **12**, 261-271, (2010).

22 Sari, A., Mendil, D., Tuzen, M. & Soylak, M. Biosorption of palladium(II) from aqueous solution by moss (*Racomitrium lanuginosum*) biomass: Equilibrium, kinetic and thermodynamic studies. *Journal of Hazardous Materials* **162**, 874-879, (2009).

23 Deplanche, K., Caldelari, I., Mikheenko, I. P., Sargent, F. & Macaskie, L. E. Involvement of hydrogenases in the formation of highly catalytic Pd(0) nanoparticles by bioreduction of Pd(II) using *Escherichia coli* mutant strains. *Microbiology* **156**, 2630-2640, (2010).

24 Yong, P., Rowson, N. A., Farr, J. P. G., Harris, I. R. & Macaskie, L. E. Bioaccumulation of palladium by *Desulfovibrio desulfuricans*. *Journal of Chemical Technology & Biotechnology* **77**, 593-601, (2002).

25 DeVargas I, S. D., Ashworth AM, Hardy CM, Macaskie LE. in *16th Int. Biohydrometallurgy Symposium.* 605–616 (16th International Biohydrometallurgy Symposium, Cape Town, South Africa, 2005).

26 Lloyd, J. R., Ridley, J., Khizniak, T., Lyalikova, N. N. & Macaskie, L. E. Reduction of Technetium by *Desulfovibrio desulfuricans*: Biocatalyst Characterization and Use in a Flowthrough Bioreactor. *Appl. Environ. Microbiol.* **65**, 2691-2696 (1999).

27 De Luca, G., de Philip, P., Dermoun, Z., Rousset, M. & Vermeglio, A. Reduction of Technetium(VII) by *Desulfovibrio fructosovorans* Is Mediated by the Nickel-Iron Hydrogenase. *Appl. Environ. Microbiol.* **67**, 4583-4587, (2001).

28 Windt, W. D., Aelterman, P. & Verstraete, W. Bioreductive deposition of palladium (0) nanoparticles on *Shewanella oneidensis* with catalytic activity towards reductive dechlorination of polychlorinated biphenyls. *Environmental Microbiology* **7**, 314-325, (2005).

29 Bunge, M. *et al.* Formation of palladium(0) nanoparticles at microbial surfaces. *Biotechnology and Bioengineering* **107**, 206-215, (2010).

30 Omajali, J., Mikheenko, I., Merroun, M., Wood, J. & Macaskie, L. Characterization of intracellular palladium nanoparticles synthesized by *Desulfovibrio desulfuricans* and *Bacillus benzeovorans*. *Journal of Nanoparticle Research* **17**, 1-17, (2015).

31 Vijayaraghavan, K. & Yun, Y.-S. Bacterial biosorbents and biosorption. *Biotechnology Advances* **26**, 266-291 (2008).

32 Yong, P., Mikheenko, I., Deplanche, K., Redwood, M. & Macaskie, L. Biorefining of precious metals from wastes: an answer to manufacturing of cheap nanocatalysts for fuel cells and power generation via an integrated biorefinery? *Biotechnology Letters* **32**, 1821-1828, (2010).

33 Redwood, M. D., Deplanche, K., Baxter-Plant, V. S. & Macaskie, L. E. Biomass-supported palladium catalysts on *Desulfovibrio desulfuricans* and *Rhodobacter sphaeroides*. *Biotechnology and Bioengineering* **99**, 1045-1054, (2008).

34 Orozco, R. *et al.* Towards an integrated system for bio-energy: hydrogen production by *Escherichia coli* and use of palladium-coated waste cells for electricity generation in a fuel cell. *Biotechnology Letters* **32**, 1837-1845, (2010).

35 Ogi, T., Honda, R., Tamaoki, K., Saitoh, N. & Konishi, Y. Direct room-temperature synthesis of a highly dispersed Pd nanoparticle catalyst and its electrical properties in a fuel cell. *Powder Technology* **205**, 143-148, (2011).

36 Ahmadi, T. S., Wang, Z. L., Green, T. C., Henglein, A. & El-Sayed, M. A. Shape-Controlled Synthesis of Colloidal Platinum Nanoparticles. *Science* **272**, 1924-1925 (1996).

37 Courtney, J. M. *Bio-Engineered Gas Diffusion Electrodes (GDEs) for Proton Exchange Membrane Fuel Cells (PEMFCs)* MRes thesis, University of Birmingham, (2011).

38 Farago, M. E., Mullen, W. A. & Payne, J. B. The uptake of platinum group metals by tomato, bean and corn. *Inorganica Chimica Acta* **34**, 151-154, (1979).

39 Sharma, N. C. *et al.* Synthesis of Plant-Mediated Gold Nanoparticles and Catalytic Role of Biomatrix-Embedded Nanomaterials. *Environmental Science & Technology* **41**, 5137-5142, (2007).

40 Bali, R., Siegele, R. & Harris, A. Biogenic Pt uptake and nanoparticle formation in *Medicago sativa* and *Brassica juncea*. *Journal of Nanoparticle Research* **12**, 3087-3095, (2010).

41 Shacklette, H. T., Lakin, H. W., Hubert, A. E. & Curtin, G. C. (Geological Survey Bulletin 1314-B, 1970).

42 Castro, L., Blázquez, M. L., González, F., Muñoz, J. A. & Ballester, A. Extracellular biosynthesis of gold nanoparticles using sugar beet pulp. *Chemical Engineering Journal* **164**, 92-97, (2010).

43 Castro, L. *et al.* Biosynthesis of gold nanowires using sugar beet pulp. *Process Biochemistry* **46**, 1076-1082, (2011).

44 Shankar, S. S., Ahmad, A. & Sastry, M. Geranium Leaf Assisted Biosynthesis of Silver Nanoparticles. *Biotechnology Progress* **19**, 1627-1631, (2003).

45 Sathishkumar, M. *et al.* Phyto-crystallization of palladium through reduction process using *Cinnamom zeylanicum* bark extract. *Journal of Hazardous Materials* **171**, 400-404, (2009).

46 Box, G. E. P. & Wilson, K. B. On the Experimental Attainment of Optimum Conditions. *Journal of the Royal Statistical Society. Series B (Methodological)* **13**, 1-45 (1951).

47 Granier, T., Gallois, B., Dautant, A., Langlois d'Estaintot, B. & Précigoux, G. Comparison of the Structures of the Cubic and Tetragonal Forms of Horse-Spleen Apoferritin. *Acta Crystallographica Section D* **53**, 580-587, (1997).

48 Ueno, T. *et al.* Size-Selective Olefin Hydrogenation by a Pd Nanocluster Provided in an Apo-Ferritin Cage. *Angewandte Chemie International Edition* **43**, 2527-2530, (2004).

49 Deng, Q., Yang, B., Wang, J., Whiteley, C. & Wang, X. Biological synthesis of platinum nanoparticles with apoferritin. *Biotechnology Letters* **31**, 1505-1509, (2009).

50 Yang, D. & Nagayama, K. Permeation of small molecules into the cavity of ferritin as revealed by proton nuclear magnetic resonance relaxation. *Biochem. J.* **307**, 253-256 (1995).

51 Gálvez, N. *et al.* Apoferritin as a nanoreactor for preparing metallic nanoparticles. *Comptes Rendus Chimie* **11**, 1207-1212, (2008).

52 Gugliotti, L. A., Feldheim, D. L. & Eaton, B. E. RNA-Mediated Control of Metal Nanoparticle Shape. *Journal of the American Chemical Society* **127**, 17814-17818, (2005).

53 Liu, D. *et al.* RNA-Mediated Synthesis of Palladium Nanoparticles on Au Surfaces. *Langmuir* **22**, 5862-5866, (2006).

54 Parsons, J. G., Gardea-Torresdey, J. L., Tiemann, K. J. & Gamez, G. Investigation of trace level binding of $PtCl_6$ and $PtCl_4$ to alfalfa biomass (*Medicago sativa*) using Zeeman graphite furnace atomic absorption spectrometry. *Analytica Chimica Acta* **478**, 139-145, (2003).

55 Ruiz, M., Sastre, A. M. & Guibal, E. Palladium sorption on glutaraldehyde-crosslinked chitosan. *Reactive and Functional Polymers* **45**, 155-173, (2000).

56 Godlewska-Zylkiewicz, B. & Kozlowska, M. Solid phase extraction using immobilized yeast *Saccharomyces cerevisiae* for determination of palladium in road dust. *Analytica Chimica Acta* **539**, 61-67, (2005).

57 Li, Q., Bürgi, T. & Chen, H. Preparation of gold nanorods of high quality and high aspect ratio. *Journal of Wuhan University of Technology--Materials Science Edition* **25**, 104-107, (2010).

58 Chowdhury, S. K., Katta, V. & Chait, B. T. Probing conformational changes in proteins by mass spectrometry. *Journal of the American Chemical Society* **112**, 9012-9013, (1990).

59 Alexov, E. G. & Gunner, M. R. Incorporating protein conformational flexibility into the calculation of pH-dependent protein properties. *Biophysical Journal* **72**, 2075-2093, (1997).

60 Casal, H. L., Köhler, U. & Mantsch, H. H. Structural and conformational changes of β-lactoglobulin B: an infrared spectroscopic study of the effect of pH and temperature. *Biochimica et Biophysica Acta (BBA) - Protein Structure and Molecular Enzymology* **957**, 11-20, (1988).

61 Guibal, E., Larkin, A., Vincent, T. & Tobin, J. M. Chitosan Sorbents for Platinum Sorption from Dilute Solutions. *Industrial & Engineering Chemistry Research* **38**, 4011-4022, (1999).

62 Søbjerg, L. S., Lindhardt, A. T., Skrydstrup, T., Finster, K. & Meyer, R. L. Size control and catalytic activity of bio-supported palladium nanoparticles. *Colloids and Surfaces B: Biointerfaces* **85**, 373-378, (2011).

63 Riddin, T., Gericke, M. & Whiteley, C. G. Biological synthesis of platinum nanoparticles: Effect of initial metal concentration. *Enzyme and Microbial Technology* **46**, 501-505, (2010).

64 Gadd, G. M. & Griffiths, A. J. Microorganisms and heavy metal toxicity. *Microbial Ecology* **4**, 303-317, (1977).

65 De Windt, W. *et al.* Biological control of the size and reactivity of catalytic Pd(0) produced by *Shewanella oneidensis*. *Antonie van Leeuwenhoek* **90**, 377-389, (2006).

66 Williams, D. B. & Carter, C. B. in *Transmission Electron Microscopy: A Textbook for Materials Science,* Ch. 1, (Springer, 2009).

67 Ohanian, H. C. in *Physics,* Ch. 43, (Norton, 1989).

68 Williams, D. B. & Carter, C. B. in *Transmission Electron Microscopy: A Textbook for Materials Science,* Ch. 6, (Springer, 2009).

69 Prasad, P. N. in *Nanophotonics,* Ch. 7.2, (Wiley, 2004).

70 Williams, D. B. & Carter, C. B. in *Transmission Electron Microscopy: A Textbook for Materials Science,* Ch. 4, (Springer, 2009).

71 Williams, D. B. & Carter, C. B. in *Transmission Electron Microscopy: A Textbook for Materials Science,* Ch. 2, (Springer, 2009).

72 Egerton, R. F. in *Physical Principals of Electron Microscopy: An Introduction to TEM, SEM and AEM,* Ch. 4, (Springer, 2006).

73 Heumann, M., Uhlig, T., Schneider, M. & Zweck, J. in *Magnetic Storage Systems Beyond 2000* Vol. 41 *NATO Science Series* (ed George C Hadjipanayis), Ch. 21, 281-285 (Springer Netherlands, 2001).

74 Ohanian, H. C. in *Physics,* Ch. 22, (Norton, 1989).

75 Williams, D. B. & Carter, C. B. in *Transmission Electron Microscopy: A Textbook for Materials Science,* Ch. 9, (Springer, 2009).

76 Egerton, R. F. in *Physical Principles of Electron Microscopy,* Ch. 1, (Publisher, 2006).

77 Goldstein, J. I. in *Practical Scanning Electron Microscopy,* Ch. 3, (Springer, 1975).

78 Goldstein, J. I. in *Practical Scanning Electron Microscopy,* Ch. 4, (Springer, 1975).

79 Danilatos, G. D. in *In-Situ Microscopy in Materials Research* (ed P. L. Gai), Ch. 2, 13-44 (Springer US, 1997).

80 Egerton, R. F. in *Electron Energy-Loss Spectroscopy in the Electron Microscope,* Ch. 3, (Springer, 2011).

81 Ohanian, H. C. in *Physics,* Ch. Interlude I, (Norton, 1989).

82 Authier, A. in *Dynamical Theory of X-Ray Diffraction,* Ch. 1, (Oxford University Press, 2001).

83 Authier, A. in *Dynamical Theory of X-Ray Diffraction,* Ch. 5, (Oxford University Press, 2001).

84 Chung, F. H. & Smith, D. K. in *Industrial Applications of X-Ray Diffraction,* Ch. 1, (Marcel Dekker Inc., 1999).

85 Ladd, M. & Palmer, R. in *Structure Determination by X-Ray Crystallography,* Ch. 12, (Springer, 2013).

86 Warren, B. E. in *X-Ray Diffraction,* Ch. 13, (Dover Publications Inc., 1991).

87 Ohanian, H. C. in *Physics,* Ch. 42, (Norton, 1989).

88 van der Heide, P. in *X-ray Photoelectron Spectroscopy: An introduction to Principles and Practices,* Ch. 1, (Wiley, 2012).

89 Hofmann, S. in *Auger- and X-Ray Photoelectron Spectroscopy in Materials Science: A User-Oriented Guide,* Ch. 1, (Springer, 2013).

90 van der Heide, P. in *X-ray Photoelectron Spectroscopy: An introduction to Principles and Practices,* Ch. 5, (Wiley, 2012).

91 Briggs, D. in *Surface analysis of polymers by XPS and static SIMS,* Ch. 2, (Cambridge Solid State Science Series, 1998).

92 van der Heide, P. in *X-ray Photoelectron Spectroscopy: An introduction to Principles and Practices,* Ch. 3, (Wiley, 2012).

93 Hofmann, S. in *Auger- and X-Ray Photoelectron Spectroscopy in Materials Science: A User-Oriented Guide,* Ch. 2, (Springer, 2013).

94 Grünert, W. in *Characterization of Solid Materials and Heterogenous Catalysts: from Structure to Surface Reactivity* (eds M. Che & J. C. Vedrine), Ch. 13, (Wiley, 2012).

95 Hofmann, S. in *Auger- and X-Ray Photoelectron Spectroscopy in Materials Science: A User-Oriented Guide,* Ch. 3, (Springer, 2013).

96 Coulier, J. & Niemantsverdriet, J. W. in *Encyclopedia of Chemical Physics and Physical Chemistry* (eds N. D. Spencer & J. H. Moore), Ch. B1.25, (Institute of Physics Publishing, 2001).

97 Granqvist, C. G. in *Handbook of Inorganic Electrochromic Materials,* Ch. 7, (Elsevier, 1995).

98 de Hoffmann, E. & Stroobant, V. in *Mass Spectrometry Principles and Applications,* 1-13 (Wiley, 2007).

99 de Hoffmann, E. & Stroobant, V. in *Mass Spectrometry Principles and Applications,* Ch. 6, (Wiley, 2007).

100 de Hoffmann, E. & Stroobant, V. in *Mass Spectrometry Principles and Applications,* Ch. 3, (Wiley, 2007).

101 de Hoffmann, E. & Stroobant, V. in *Mass Spectrometry Principles and Applications,* Ch. 1, (Wiley, 2007).

102 de Hoffmann, E. & Stroobant, V. in *Mass Spectrometry Principles and Applications,* Ch. 2, (Wiley, 2007).

103 McCurdy, E., Woods, G. & Potter, D. Unmatched Removal of Spectral Interferences in ICP-MS Using the Agilent Octopole Reaction System with Helium Collision Mode. *Metals Analysis* (2006).

104 McElfresh, M. (http://www.qdusa.com/sitedocs/appNotes/mpms/FundPrimer.pdf).

105 Josephson, B. D. Possible new effects in superconductive tunnelling. *Physics Letters* **1**, 251-253, (1962).

106 London, F. & London, H. Supraleitung und diamagnetismus. *Physica* **2**, 341-354, (1935).

107 Braginski, A. I. & Clarke, J. in *The SQUID Handbook,* 1-28 (Wiley-VCH Verlag GmbH & Co. KGaA, 2005).

108 Chesca, B., Kleiner, R. & Koelle, D. in *The SQUID Handbook,* 29-92 (Wiley-VCH Verlag GmbH & Co. KGaA, 2005).

109 McElfresh, M., Li, S. & Sager, R. (http://qdusa.com/sitedocs/appNotes/mpms/effects.pdf).

110 *Practical Aspects of μSR*, <http://www.isis.stfc.ac.uk/groups/muons/muon-training-school/2008-practical-aspects-spc7875.pdf> (2008).

111 PSI. *General Purpose Surface-Muon Instrument (GPS)*, <http://www.psi.ch/smus/gps#General_Specifications>

112 Lord, J. Muon Beam Lines. (ISIS, 2008).

113 Blundell, S. J. Spin-polarized muons in condensed matter physics. *Contemporary Physics* **40**, 175-192 (1999).

114 Thompson, W. J. *Angular Momentum*. 175-177 (Wiley, 2008).

115 Cox, S. F. J. Implanted muon studies in condensed matter science. *Journal of Physics C: Solid State Physics* **20**, 3187 (1987).

116 Garwin, R. L., Lederman, L. M. & Weinrich, M. Observations of the Failure of Conservation of Parity and Charge Conjugation in Meson Decays: the Magnetic Moment of the Free Muon. *Physical Review* **105**, 1415-1417 (1957).

117 Brewer, J. H., Crowe, K. M., Gygax, F. N. & Schenck, A. in *Muon Physics* (ed Vernon W. Hughes) 3-139 (Academic Press, 1975).

118 Lago, J., Blundell, S. J. & Baines, C. μSR investigation of spin dynamics in the spin-ice material $Dy_2Ti_2O_7$. *Journal of Physics: Condensed Matter* **19**, 326210 (2007).

119 Chang, L. J., Lees, M. R., Balakrishnan, G., Kao, Y. J. & Hillier, A. D. Low-temperature muon spin rotation studies of the monopole charges and currents in Y doped $Ho_2Ti_2O_7$. *Sci. Rep.* **3**, (2013).

120 Hillier, A. D., King, P. J. C., Cottrell, S. P. & Lord, J. S. (ISIS Facility, 2005).

121 Matjie, R. H., Scurrell, M. S. & Bunt, J. The selective dissolution of alumina, cobalt and platinum from a calcined spent catalyst using different lixiviants. *Minerals Engineering* **18**, 801-810, (2005).

122 Godlewska-Zylkiewicz, B. Biosorption of platinum and palladium for their separation/preconcentration prior to graphite furnace atomic absorption spectrometric determination. *Spectrochimica Acta Part B: Atomic Spectroscopy* **58**, 1531-1540, (2003).

123 CasaXPS. Lorentzian Asymmetric Lineshape. (2008).

124 CasaXPS. (Casa Software Ltd, 2006).

125 Battistoni, C., Giuliani, A. M., Paparazzo, E. & Tarli, F. Platinum complexes of the methyl esters of dithiocarbazic acid and 3-phenyldithiocarbazic acid. *Journal of the Chemical Society, Dalton Transactions*, 1293-1299, (1984).

126 Mikheenko, I. *Bioaccumulation of palladium on bacterial surfaces in nanoscale palladium recovery*, University of Birmingham, (2004).

127 Vázquez, J. A. *et al.* Evaluation of toxic effects of several carboxylic acids on bacterial growth by toxicodynamic modelling. *Microbial Cell Factories* **10**, 100-100, (2011).

128 Bagramyan, K. & Trchounian, A. Structural and Functional Features of Formate Hydrogen Lyase, an Enzyme of Mixed-Acid Fermentation from *Escherichia coli*. *Biochemistry (Moscow)* **68**, 1159-1170, (2003).

129 Baatout, S., Leys, N., Hendrickx, L., Dams, A. & Mergeay, M. Physiological changes induced in bacteria following pH stress as a model for space research. *Acta Astronautica* **60**, 451-459, (2007).

130 Southam, G. & Beveridge, T. J. The occurrence of sulfur and phosphorus within bacterially derived crystalline and pseudocrystalline octahedral gold formed in vitro. *Geochimica et Cosmochimica Acta* **60**, 4369-4376, (1996).

131 Yuan, S., Xiong, G., Roguin, A., Teoh, S. H. & Choong, C. *Amelioration of Blood Compatibility and Endothelialization of Polycaprolactone Substrates by Surface-Initiated Atom Transfer Radical Polymerization*. (Intech, 2013).

132 Bagri, A. *et al.* Structural evolution during the reduction of chemically derived graphene oxide. *Nat Chem* **2**, 581-587, (2010).

133 Khattak, G. D., Salim, M. A., Al-Harthi, A. S., Thompson, D. J. & Wenger, L. E. Structure of molybdenum-phosphate glasses by X-ray photoelectron spectroscopy (XPS). *Journal of Non-Crystalline Solids* **212**, 180-191, (1997).

134 Matloob, M. H. & Roberts, M. W. Electron spectroscopic study of nitrogen species adsorbed on copper. *Journal of the Chemical Society, Faraday Transactions 1: Physical Chemistry in Condensed Phases* **73**, 1393-1405 (1977).

135 Dückers, K. & Bonzel, H. P. Core and valence level spectroscopy with Y Mζ radiation: CO and K on (110) surfaces of Ir, Pt and Au. *Surface Science* **213**, 25-48, (1989).

136 Silva, W. M. *et al.* Surface properties of oxidized and aminated multi-walled carbon nanotubes. *Journal of the Brazilian Chemical Society* **23**, 1078-1086 (2012).

137 Contour, J. P., Mouvier, G., Hoogewys, M. & Leclere, C. X-ray photoelectron spectroscopy and electron microscopy of Pt-Rh gauzes used for catalytic oxidation of ammonia. *Journal of Catalysis* **48**, 217-228, (1977).

138 Stypula, B. & Stoch, J. The characterization of passive films on chromium electrodes by XPS. *Corrosion Science* **36**, 2159-2167, (1994).

139 Fierro, J. L. G., Palacios, J. M. & Tomas, F. An analytical SEM and XPS study of platinum–rhodium gauzes used in high pressure ammonia burners. *Surface and Interface Analysis* **13**, 25-32, (1988).

140 Gardner, S. D., Singamsetty, C. S. K., Booth, G. L., He, G.-R. & Pittman Jr, C. U. Surface characterization of carbon fibers using angle-resolved XPS and ISS. *Carbon* **33**, 587-595, (1995).

141 Tong, Z. *et al.* Layered polyaniline/graphene film from sandwich-structured polyaniline/graphene/polyaniline nanosheets for high-performance pseudosupercapacitors. *Journal of Materials Chemistry A* **2**, 4642-4651, (2014).

142 CasaXPS. Quantification using Asymmetric Line-Shapes. (2005).

143 Bard, A. J. & Faulkner, L. R. *Electrochemical Methods Fundamentals and Applications*. (Wiley, 2001).

144 Van Benschoten, J. J., Lewis, J. Y., Heineman, W. R., Roston, D. A. & Kissinger, P. T. Cyclic voltammetry experiment. *Journal of Chemical Education* **60**, 772, (1983).

145 Konopka, S. J. & McDuffie, B. Diffusion coefficients of ferri- and ferrocyanide ions in aqueous media, using twin-electrode thin-layer electrochemistry. *Analytical Chemistry* **42**, 1741-1746, (1970).

146 Stassi, A., Gatto, I., Baglio, V., Passalacqua, E. & Aricò, A. S. Investigation of Pd-based electrocatalysts for oxygen reduction in PEMFCs operating under automotive conditions. *Journal of Power Sources* **222**, 390-399, (2013).

147 Jung, S. H., Kim, S. L., Kim, M. S., Park, Y. & Lim, T. W. Experimental study of gas humidification with injectors for automotive PEM fuel cell systems. *Journal of Power Sources* **170**, 324-333, (2007).

148 James, B. D. & Spisak, A. B. Mass Production Cost Estimation of Direct H_2 PEM Fuel Cell Systems for Transportation Applications: 2012 Update. (Strategic Analysis Inc., 2012).

149 Gigliucci, G., Petruzzi, L., Cerelli, E., Garzisi, A. & La Mendola, A. Demonstration of a residential CHP system based on PEM fuel cells. *Journal of Power Sources* **131**, 62-68, (2004).

150 Barelli, L., Bidini, G., Gallorini, F. & Ottaviano, A. An energetic–exergetic analysis of a residential CHP system based on PEM fuel cell. *Applied Energy* **88**, 4334-4342, (2011).

151 Mishra, B. & Wu, J. Exploring Transient Behavior at Startup of a Polymer Electrolyte Membrane Fuel Cell. *Journal of Fuel Cell Science and Technology* **7**, (2010).

152 Oszcipok, M., Hakenjos, A., Riemann, D. & Hebling, C. Start Up and Freezing Processes in PEM Fuel Cells. *Fuel Cells* **7**, 135-141, (2007).

153 Redwood, M. D., Orozco, R. L., Majewski, A. J. & Macaskie, L. E. An integrated biohydrogen refinery: Synergy of photofermentation, extractive fermentation and hydrothermal hydrolysis of food wastes. *Bioresource Technology* **119**, 384-392, (2012).

154 Macaskie, L. E. *et al.* Applications of bacterial hydrogenases in waste decontamination, manufacture of novel bionanocatalysts and in sustainable energy. *Biochemical Society Transactions* **33**, 76-79 (2005).

155 Yong, P., Paterson-Beedle, M., Mikheenko, I. & Macaskie, L. From bio-mineralisation to fuel cells: biomanufacture of Pt and Pd nanocrystals for fuel cell electrode catalyst. *Biotechnology Letters* **29**, 539-544, (2007).

156 Murray, A. J. Platinum Group Metal Recovery From Powdery Waste. (2010).

157 Glaister, B. J. & Mudd, G. M. The environmental costs of platinum–PGM mining and sustainability: Is the glass half-full or half-empty? *Minerals Engineering* **23**, 438-450, (2010).

158 López-Quintela, M. A. & Rivas, J. Chemical Reactions in Microemulsions: A Powerful Method to Obtain Ultrafine Particles. *Journal of Colloid and Interface Science* **158**, 446-451, (1993).

159 Roth, M. & Hempelmann, R. Nanocrystalline LiF via microemulsion systems. *Journal of Materials Chemistry* **9**, 493-497, (1999).

160 Menard, L. D., Xu, F., Nuzzo, R. G. & Yang, J. C. Preparation of TiO_2-supported Au nanoparticle catalysts from a Au_{13} cluster precursor: Ligand removal using ozone exposure versus a rapid thermal treatment. *Journal of Catalysis* **243**, 64-73, (2006).

161 Lopez-Sanchez, J. A. *et al.* Facile removal of stabilizer-ligands from supported gold nanoparticles. *Nat Chem* **3**, 551-556, (2011).

162 Solla-Gullon, J., Montiel, V., Aldaz, A. & Clavilier, J. Synthesis and Electrochemical Decontamination of Platinum-Palladium Nanoparticles Prepared by Water-in-Oil Microemulsion. *Journal of The Electrochemical Society* **150**, E104-E109, (2003).

163 Clavilier, J. & Armand, D. Electrochemical induction of changes in the distribution of the hydrogen adsorption states on Pt (100) and Pt (111) surfaces in contact with sulphuric acid solution. *Journal of Electroanalytical Chemistry and Interfacial Electrochemistry* **199**, 187-200, (1986).

164 Hernández, J., Solla-Gullón, J. & Herrero, E. Gold nanoparticles synthesized in a water-in-oil microemulsion: electrochemical characterization and effect of the surface structure on the oxygen reduction reaction. *Journal of Electroanalytical Chemistry* **574**, 185-196, (2004).

165 Solla-Gullón, J., Montiel, V., Aldaz, A. & Clavilier, J. Electrochemical characterisation of platinum nanoparticles prepared by microemulsion: how to clean them without loss of crystalline surface structure. *Journal of Electroanalytical Chemistry* **491**, 69-77, (2000).

166 Yang, W.-H., Kim, M. H. & Ham, S.-W. Effect of calcination temperature on the low-temperature oxidation of CO over CoO_x/TiO_2 catalysts. *Catalysis Today* **123**, 94-103, (2007).

167 Newton, J. E., Preece, J. A. & Pollet, B. G. Control of nanoparticle aggregation in PEMFCs using surfactants. *International Journal of Low-Carbon Technologies* **7**, 38-43, (2012).

168 Zhou, Z. *et al.* Preparation of highly active Pt/C cathode electrocatalysts for DMFCs by an improved aqueous impregnation method. *Phys Chem Chem Phys* **5**, 5485-5488, (2003).

169 Attard, G., Casadesús, M., Macaskie, L. E. & Deplanche, K. Biosynthesis of platinum nanoparticles by *Escherichia coli* MC4100: can such nanoparticles exhibit intrinsic surface enantioselectivity? *Langmuir* **28**, 5267-5274, (2012).

170 Takahashi, I. & Kocha, S. S. Examination of the activity and durability of PEMFC catalysts in liquid electrolytes. *Journal of Power Sources* **195**, 6312-6322, (2010).

171 Mayrhofer, K. J. J. *et al.* Measurement of oxygen reduction activities via the rotating disc electrode method: From Pt model surfaces to carbon-supported high surface area catalysts. *Electrochim. Acta* **53**, 3181-3188, (2008).

172 Garsany, Y., Baturina, O. A., Swider-Lyons, K. E. & Kocha, S. S. Experimental Methods for Quantifying the Activity of Platinum Electrocatalysts for the Oxygen Reduction Reaction. *Analytical Chemistry* **82**, 6321-6328, (2010).

173 Smilgies, D.-M. Scherrer grain-size analysis adapted to grazing-incidence scattering with area detectors. *Journal of Applied Crystallography* **42**, 1030-1034, (2009).

174 Liu, J., Takeshi, D., Sasaki, K. & Lyth, S. M. Defective Graphene Foam: A Platinum Catalyst Support for PEMFCs. *Journal of The Electrochemical Society* **161**, F838-F844, (2014).

175 Hansen, T. W., DeLaRiva, A. T., Challa, S. R. & Datye, A. K. Sintering of Catalytic Nanoparticles: Particle Migration or Ostwald Ripening? *Accounts of Chemical Research* **46**, 1720-1730, (2013).

176 Abramoff, M. D., Magalhaes, P. J. & Ram, S. J. Image Processing with ImageJ. *Biophotonoics International* **11**, 36-42 (2004).

177 Savitskii, E. M. *Physical Metallurgy of Platinum Metals*. 31 (Pergamon Press, 1978).

178 Parthasarathy, A., Dave, B., Srinivasan, S., Appleby, A. J. & Martin, C. R. The Platinum Microelectrode/Nafion Interface: An Electrochemical Impedance Spectroscopic Analysis of Oxygen Reduction Kinetics and Nafion Characteristics. *Journal of The Electrochemical Society* **139**, 1634-1641, (1992).

179 Nesselberger, M. *et al.* The Particle Size Effect on the Oxygen Reduction Reaction Activity of Pt Catalysts: Influence of Electrolyte and Relation to Single Crystal Models. *Journal of the American Chemical Society* **133**, 17428-17433, (2011).

180 St. John, S. & Angelopoulos, A. P. In situ analysis of optimum surface atom coordination for Pt nanoparticle oxygen reduction electrocatalysts. *Electrochim. Acta* **112**, 258-268, (2013).

181 Clavilier, J., El Achi, K. & Rodes, A. In situ probing of step and terrace sites on Pt(S)-[n(111) × (111)] electrodes. *Chemical Physics* **141**, 1-14, (1990).

182 van der Niet, M. J. T. C., Garcia-Araez, N., Hernández, J., Feliu, J. M. & Koper, M. T. M. Water dissociation on well-defined platinum surfaces: The electrochemical perspective. *Catalysis Today* **202**, 105-113, (2013).

183 Gómez, R. & Clavilier, J. Electrochemical behaviour of platinum surfaces containing (110) sites and the problem of the third oxidation peak. *Journal of Electroanalytical Chemistry* **354**, 189-208, (1993).

184 Gómez-Marín, A. M. & Feliu, J. M. Oxygen reduction on nanostructured platinum surfaces in acidic media: Promoting effect of surface steps and ideal response of Pt(1 1 1). *Catalysis Today* **244**, 172-176, (2015).

185 Berná, A., Climent, V. & Feliu, J. M. New understanding of the nature of OH adsorption on Pt(1 1 1) electrodes. *Electrochemistry Communications* **9**, 2789-2794, (2007).

186 Domke, K., Herrero, E., Rodes, A. & Feliu, J. M. Determination of the potentials of zero total charge of Pt(100) stepped surfaces in the [01$\bar{1}$] zone. Effect of the step density and anion adsorption. *Journal of Electroanalytical Chemistry* **552**, 115-128, (2003).

187 Souza-Garcia, J., Angelucci, C. A., Climent, V. & Feliu, J. M. Electrochemical features of Pt(S)[n(110) × (100)] surfaces in acidic media. *Electrochemistry Communications* **34**, 291-294, (2013).

188 Souza-Garcia, J., Climent, V. & Feliu, J. M. Voltammetric characterization of stepped platinum single crystal surfaces vicinal to the (1 1 0) pole. *Electrochemistry Communications* **11**, 1515-1518, (2009).

189 Tritsaris, G. A., Greeley, J., Rossmeisl, J. & Nørskov, J. K. Atomic-Scale Modeling of Particle Size Effects for the Oxygen Reduction Reaction on Pt. *Catal Lett* **141**, 909-913, (2011).

190 Hitotsuyanagi, A., Nakamura, M. & Hoshi, N. Structural effects on the activity for the oxygen reduction reaction on n(1 1 1)–(1 0 0) series of Pt: correlation with the oxide film formation. *Electrochim. Acta* **82**, 512-516, (2012).

191 Kuzume, A., Herrero, E. & Feliu, J. M. Oxygen reduction on stepped platinum surfaces in acidic media. *Journal of Electroanalytical Chemistry* **599**, 333-343, (2007).

192 Chen, H., Brener, N. E. & Callaway, J. Electronic structure, optical and magnetic properties of fcc palladium. *Physical Review B* **40**, 1443-1449 (1989).

193 Creamer, N., Mikheenko, I., Johnson, C., Cottrell, S. & Macaskie, L. Local magnetism in palladium bionanomaterials probed by muon spectroscopy. *Biotechnology Letters* **33**, 969-976, (2011).

194 Rastogi, P. K., Ganesan, V. & Krishnamoorthi, S. Palladium nanoparticles incorporated polymer-silica nanocomposite based electrochemical sensing platform for nitrobenzene detection. *Electrochim. Acta* **147**, 442-450, (2014).

195 Liu, Y., Zhu, W., Wu, D. & Wei, Q. Electrochemical determination of dopamine in the presence of uric acid using palladium-loaded mesoporous Fe_3O_4 nanoparticles. *Measurement* **60**, 1-5, (2015).

196 Gupta, D. *et al.* A low temperature hydrogen sensor based on palladium nanoparticles. *Sensors and Actuators B: Chemical* **196**, 215-222, (2014).

197 Budroni, G., Corma, A., García, H. & Primo, A. Pd nanoparticles embedded in sponge-like porous silica as a Suzuki–Miyaura catalyst: Similarities and differences with homogeneous catalysts. *Journal of Catalysis* **251**, 345-353, (2007).

198 Phan, N. T. S. & Le, H. V. Superparamagnetic nanoparticles-supported phosphine-free palladium catalyst for the Sonogashira coupling reaction. *Journal of Molecular Catalysis A: Chemical* **334**, 130-138, (2011).

199 Creamer, N. J. *et al.* A biogenic catalyst for hydrogenation, reduction and selective dehalogenation in non-aqueous solvents. *Hydrometallurgy* **94**, 138-143, (2008).

200 Bennett, J. A. *et al.* Nanoparticles of palladium supported on bacterial biomass: New re-usable heterogeneous catalyst with comparable activity to homogeneous colloidal Pd in the Heck reaction. *Applied Catalysis B: Environmental* **140–141**, 700-707, (2013).

201 De Corte, S. *et al.* Biosupported Bimetallic Pd–Au Nanocatalysts for Dechlorination of Environmental Contaminants. *Environmental Science & Technology* **45**, 8506-8513, (2011).

202 Deplanche, K. Novel gold/palladium bioinorganic catalysts for selective oxidation of alcohols. *Journal of Biotechnology* **150, Supplement**, 198, (2010).

203 Guo, Y. *et al.* Electro-oxidation of formaldehyde and methanol over hollow porous palladium nanoparticles with enhanced catalytic activity. *Catalysis Communications* **58**, 40-45, (2015).

204 Chen, D., Cui, P., He, H., Liu, H. & Yang, J. Highly catalytic hollow palladium nanoparticles derived from silver@silver–palladium core–shell nanostructures for the oxidation of formic acid. *Journal of Power Sources* **272**, 152-159, (2014).

205 Kishore, S., Nelson, J. A., Adair, J. H. & Eklund, P. C. Hydrogen storage in spherical and platelet palladium nanoparticles. *Journal of Alloys and Compounds* **389**, 234-242, (2005).

206 Rather, S.-u., Zacharia, R., Hwang, S. W., Naik, M.-u. & Nahm, K. S. Hyperstoichiometric hydrogen storage in monodispersed palladium nanoparticles. *Chemical Physics Letters* **438**, 78-84, (2007).

207 Coronado, E., Ribera, A., Garcia-Martinez, J., Linares, N. & Liz-Marzan, L. M. Synthesis, characterization and magnetism of monodispersed water soluble palladium nanoparticles. *Journal of Materials Chemistry* **18**, 5682-5688, (2008).

208 Clemente-Leon, M., Coronado, E., Soriano-Portillo, A., Galvez, N. & Dominguez-Vera, J. M. Permanent magnetism in apoferritin-encapsulated Pd nanoparticles. *Journal of Materials Chemistry* **17**, 49-51, (2007).

209 Mendoza, D., Morales, F., Escudero, R. & Walter, J. Magnetization studies in quasi two-dimensional palladium nanoparticles encapsulated in a graphite host. *Journal of Physics: Condensed Matter* **11**, L317 (1999).

210 Vega, A., Parlebas, J. C. & Demangeat, C. in *Handbook of magnetic materials.* (ed Buschow K. H. J.) Electronic structure calculations of low-dimensional transition metals., 199-288 (Elsevier, 2003).

211 Taniyama, T., Ohta, E. & Sato, T. Ferromagnetism of Pd fine particles. *Physica B: Condensed Matter* **237–238**, 286-288, (1997).

212 Sampedro, B. *et al.* Ferromagnetism in fcc Twinned 2.4 nm Size Pd Nanoparticles. *Physical Review Letters* **91**, 237203 (2003).

213 Angappane, S., Jeongmi, P., Youngjin, J., Hyeon, T. & Park, J. G. Magnetic Pd nanoparticles: effects of surface atoms. *Journal of Physics: Condensed Matter* **20**, 295209 (2008).

214 Oba, Y., Sato, T. & Shinohara, T. Ferromagnetism induced by strains in Pd nanoparticles. *Physical Review B* **78**, 224417 (2008).

215 Shinohara, T., Sato, T. & Taniyama, T. Ferromagnetism of gas-evaporated Pd fine particles in mesoscopic size. *Journal of Magnetism and Magnetic Materials* **272–276, Supplement**, E1181-E1182, (2004).

216 Zhang, W., Ge, Q. & Wang, L. Structure effects on the energetic, electronic, and magnetic properties of palladium nanoparticles. *The Journal of Chemical Physics* **118**, 5793-5801, (2003).

217 Vitos, L., Johansson, B. & Kollár, J. Size-dependent paramagnetic-ferromagnetic phase transition in palladium clusters. *Physical Review B* **62**, R11957-R11960 (2000).

218 Alexandre, S. S., Anglada, E., Soler, J. M. & Yndurain, F. Magnetism of two-dimensional defects in Pd: Stacking faults, twin boundaries, and surfaces. *Physical Review B* **74**, 054405 (2006).

219 Kulriya, P. K. *et al.* Enhancement of ferromagnetism in Pd nanoparticle by swift heavy ion irradiation. *Applied Physics Letters* **96**, (2010).

220 Shinohara, T., Sato, T. & Taniyama, T. Surface Ferromagnetism of Pd Fine Particles. *Physical Review Letters* **91**, 197201 (2003).

221 Mikheenko, I. P., Mikheenko, P. M., Darlington, C. N. W., Muirhead, C. M. & Macaskie, L. E. in *Biohydrometallurgy: Fundamentals, Technology and Sustainable Development* (eds V. S. T. Ciminelli & O. Garcia) 525-532 (Elsevier, 2001).

222 *EMU Technical*, <http://www.isis.stfc.ac.uk/instruments/emu/technical/emu-technical4935.html>

223 Reid, I. D. & Cox, S. F. J. Muons in sulphur. *Physica B: Condensed Matter* **289–290**, 620-624, (2000).

224 Suter, A. & Wojek, B. M. Musrfit: A Free Platform-Independent Framework for μSR Data Analysis. *Physics Procedia* **30**, 69-73, (2012).

225 Lu, W., Wang, B., Wang, K., Wang, X. & Hou, J. G. Synthesis and Characterization of Crystalline and Amorphous Palladium Nanoparticles. *Langmuir* **19**, 5887-5891, (2003).

226 Dormann, J. L., Fiorani, D. & Tronc, E. On the models for interparticle interactions in nanoparticle assemblies: comparison with experimental results. *Journal of Magnetism and Magnetic Materials* **202**, 251-267, (1999).

227 Mihaela, O. Study about the possibility to control the superparamagnetism–superferromagnetism transition in magnetic nanoparticle systems. *Journal of Magnetism and Magnetic Materials* **343**, 189-193, (2013).

228 Bakuzis, A. F. & Morais, P. C. Superferromagnetism on a two-dimensional array of magnetic nanodots: an Ising model approximation. *Journal of Magnetism and Magnetic Materials* **285**, 145-154, (2005).

229 Lord, J. S. Muon spin resonance in ferromagnets. *Journal of Magnetism and Magnetic Materials* **177–181, Part 2**, 1470-1471, (1998).

230 Wyckoff, R. W. G. *Crystal Structures* Vol. 1, 7-83 (Wiley (Interscience), 1963).

231 Fritsche, L., Noffke, J. & Eckardt, H. A relativistic treatment of interacting spin-aligned electron systems: application to ferromagnetic iron, nickel and palladium metal. *Journal of Physics F: Metal Physics* **17**, 943 (1987).

232 Moruzzi, V. L. & Marcus, P. M. Magnetism in fcc rhodium and palladium. *Physical Review B* **39**, 471-474 (1989).

233 Fang, B. *et al.* Electrocatalytic performance of Pt-based trimetallic alloy nanoparticle catalysts in proton exchange membrane fuel cells. *International Journal of Hydrogen Energy* **37**, 4627-4632, (2012).

234 Godínez-García, A., Pérez-Robles, J. F., Martínez-Tejada, H. V. & Solorza-Feria, O. Characterization and electrocatalytic properties of sonochemical synthesized PdAg nanoparticles. *Materials Chemistry and Physics* **134**, 1013-1019, (2012).

235 Ke, K., Hiroshima, K., Kamitaka, Y., Hatanaka, T. & Morimoto, Y. An accurate evaluation for the activity of nano-sized electrocatalysts by a thin-film rotating disk electrode: Oxygen reduction on Pt/C. *Electrochim. Acta* **72**, 120-128, (2012).

236 Jeong, S.-M., Kim, M. K., Kim, G.-P., Kim, T. Y. & Baeck, S.-H. Preparation of Pt–Au/carbon catalysts by a reduction method and their electrocatalytic activities for oxygen reduction reactions. *Chemical Engineering Journal* **198–199**, 435-439, (2012).

237 Yan, W.-M., Chen, C.-Y., Mei, S.-C., Soong, C.-Y. & Chen, F. Effects of operating conditions on cell performance of PEM fuel cells with conventional or interdigitated flow field. *Journal of Power Sources* **162**, 1157-1164, (2006).

238 Yan, W.-M., Mei, S.-C., Soong, C.-Y., Liu, Z.-S. & Song, D. Experimental study on the performance of PEM fuel cells with interdigitated flow channels. *Journal of Power Sources* **160**, 116-122, (2006).

239 Kennedy, D. M. *et al.* Fuel cell cathode air filters: Methodologies for design and optimization. *Journal of Power Sources* **168**, 391-399, (2007).

240 de las Heras, N., Roberts, E. P. L., Langton, R. & R. Hodgson, D. A review of metal separator plate materials suitable for automotive PEM fuel cells. *Energy & Environmental Science* **2**, 206-214, (2009).

241 Smitha, B., Sridhar, S. & Khan, A. A. Solid polymer electrolyte membranes for fuel cell applications—a review. *Journal of Membrane Science* **259**, 10-26, (2005).

242 Vosen, S. R. & Keller, J. O. Hybrid energy storage systems for stand-alone electric power systems: optimization of system performance and cost through control strategies. *International Journal of Hydrogen Energy* **24**, 1139-1156, (1999).

243 Benziger, J., Kimball, E., Mejia-Ariza, R. & Kevrekidis, I. Oxygen mass transport limitations at the cathode of polymer electrolyte membrane fuel cells. *AIChE Journal* **57**, 2505-2517, (2011).

244 Wang, X.-D., Duan, Y.-Y., Yan, W.-M. & Peng, X.-F. Effects of flow channel geometry on cell performance for PEM fuel cells with parallel and interdigitated flow fields. *Electrochim. Acta* **53**, 5334-5343, (2008).

245 Faraday, M. On the Diamagnetic conditions of Flame and Gases. *Philosophical Magazine and Journal of Science* **31**, 401-421 (1847).

246 Herzberg, G. *Molecular Spectra and Molecular Structure*. (Prentice-Hall, Inc., 1939).

247 Hund, F. *Linienspektren und Periodisches System der Elemente*. (Springer, 1927).

248 Ohanian, H. C. in *Physics*, Ch. 33, 806-822 (Norton, 1989).

249 Matsushima, H., Iida, T., Fukunaka, Y. & Bund, A. PEMFC Performance in a Magnetic Field. *Fuel Cells* **8**, 33-36, (2008).

250 Shi, J., Xu, H., Zhao, H., Lu, L. & Wu, X. Preparation of $Nd_2Fe_{14}B$/C magnetic powder and its application in proton exchange membrane fuel cells. *Journal of Power Sources* **252**, 189-199, (2014).

251 Cai, J. *et al.* Study on oxygen enrichment from air by application of the gradient magnetic field. *Journal of Magnetism and Magnetic Materials* **320**, 171-181, (2008).

252 Coey, J. M. D., Rhen, F. M. F., Dunne, P. & McMurry, S. The magnetic concentration gradient force—Is it real? *J Solid State Electrochem* **11**, 711-717, (2007).

253 Wang, L. B., Wakayama, N. I. & Okada, T. Numerical simulation of enhancement of mass transfer in the cathode electrode of a PEM fuel cell by magnet particles deposited in the cathode-side catalyst layer. *Chemical Engineering Science* **60**, 4453-4467, (2005).

254 Monzon, L. M. A. & Coey, J. M. D. Magnetic fields in electrochemistry: The Kelvin force. A mini-review. *Electrochemistry Communications* **42**, 42-45, (2014).

255 Lide, D. R. *Handbook of Chemistry and Physics*. (CRC Press, 2004).

256 Monzon, L. M. A. & Coey, J. M. D. Magnetic fields in electrochemistry: The Lorentz force. A mini-review. *Electrochemistry Communications* **42**, 38-41, (2014).

257 Okada, T. *et al.* The effect of magnetic field on the oxygen reduction reaction and its application in polymer electrolyte fuel cells. *Electrochim. Acta* **48**, 531-539, (2003).

258 Shi, J., Xu, H., Zhao, H. & Lu, L. Synthesis and properties of Fe_3O_4/polyaniline and its tiny magnetic field functions during oxygen transfer processes. *Journal of Power Sources* **205**, 129-135, (2012).

259 Shi, J., Xu, H., Lu, L. & Sun, X. Study of magnetic field to promote oxygen transfer and its application in zinc–air fuel cells. *Electrochim. Acta* **90**, 44-52, (2013).

260 Chaure, N. B., Rhen, F. M. F., Hilton, J. & Coey, J. M. D. Design and application of a magnetic field gradient electrode. *Electrochemistry Communications* **9**, 155-158, (2007).

261 García, M. A. *et al.* Ferromagnetism in Twinned Pt Nanoparticles Obtained by Laser Ablation. *Chemistry of Materials* **19**, 889-893, (2007).

262 Sakamoto, Y. *et al.* Ferromagnetism of Pt nanoparticles induced by surface chemisorption. *Physical Review B* **83**, 104420 (2011).

263 Balcerzak, M., Święcicka, E. & Balukiewicz, E. Determination of platinum and ruthenium in Pt and Pt–Ru catalysts with carbon support by direct and derivative spectrophotometry. *Talanta* **48**, 39-47, (1999).

264 Shi, J., Xu, H., Lu, L. & Sun, X. Study of magnetic field to promote oxygen transfer and its application in zinc air fuel cells. *Electrochim. Acta*, (2013).

265 Charles, S. W. in *Magnetic Properties of Fine Particles* (eds J. L. Dormann & D. Fiorani) (Elsevier, 1991).

266 Jolly, P. W. & Wilke, G. in *The Organic Chemistry of Nickel* (eds P. W. Jolly & G. Wilke) 94-138 (Academic Press, 1974).

267 Jolly, P. W. & Wilke, G. in *The Organic Chemistry of Nickel* (eds P. W. Jolly & G. Wilke) 329-401 (Academic Press, 1974).

268 Yamamoto, Y. *et al.* Magnetic properties of the noble metal nanoparticles protected by polymer. *Physica B: Condensed Matter* **329-333, Part 2**, 1183-1184, (2003).

269 Beille, J., Bloch, D. & Besnus, M. J. Itinerant ferromagnetism and susceptibility of nickel-platinum alloys. *Journal of Physics F: Metal Physics* **4**, 1275 (1974).